Versuchsanstalt für Wasserbau,
Hydrologie und Glaziologie
der Eidgenössischen
Technischen Hochschule Zürich

Mitteilungen 130

Glacier Sliding Over Sinusoidal Bed and the Characteristics of Creeping Flow Over Bedrock Undulations

G. Hilmar Gudmundsson

Zürich, 1994

Herausgeber: Prof. Dr. Dr.h.c. D. Vischer

Versuchsanstalt für Wasserbau,
Hydrologie und Glaziologie
der Eidgenössischen
Technischen Hochschule Zürich

Mitteilungen 130

Glacier Sliding Over Sinusoidal Bed and the Characteristics of Creeping Flow Over Bedrock Undulations

G. Hilmar Gudmundsson

Zürich, 1994

Herausgeber: Prof. Dr. Dr.h.c. D. Vischer

Preface

In 1979 a remarkable symposium "Glacier Beds: the Ice-Rock Interface" has been organized by the Canadian National Research Council. A wealth of excellent papers has been presented and discussed. Nevertheless, the final goal of formulating a general glacier sliding law seemingly had moved further away than before. Several speakers stressed this point; for instance Professor Hans Weertman, with his contribution "The unsolved general glacier sliding problem" or Professor Louis Lliboutry with the statement: "The best model is that which fits the largest number of observations and has the least complexity". Since this symposium, the interest in the sliding problem has grown steadily. It was roused especially by spectacular natural events: glacier surges, sudden slides of hanging glaciers, the disintegration and drastic retreat of tidewater glaciers and the "fast flow" of certain polar ice streams. Progress in understanding glacier sliding has been achieved on theoretical grounds and by applying highly developed numerical methods and experimental techniques. While no really "general" sliding law is yet in sight, several aspects of sliding are being better understood, for instance the influence of bed separation on sliding over bedrock.

In the present study, "Glacier sliding over sinusoidal bed and the characteristics of creeping flow over bedrock undulations" the ice flow close to bedrock undulations is investigated in detail. The sinusoidal bed is the one with least complexity, and yet, it comprises a good model for typical glacier-polished bedrock, where small roughness elements are absent. Dr. Hilmar Gudmundsson derives the velocity field and stress field analytically for a linear-viscous medium and small bed roughness. He then extends the study to include large bed roughness and non-linear rheology by applying a suitable numerical method. He establishes the conditions under which local extrusion flow takes place. Beyond a certain limiting value of bed roughness a new phenomenon appears: circulating flow in the troughs of the sinusoidal bed. In this case the ice can no longer escape from the troughs.

Besides giving a full account of the flow field near the interface of sliding, this study may thus help to understand certain unexpected disturbances such as local extrusion flow which have been encountered near the bed in measurements of borehole tilt. Furthermore, it will permit to assert the conditions under which ancient ice can be preserved in bedrock troughs. At a different scale, it shows the typical distribution of strain rates in glaciers which slide through overdeepenings. This last issue supplements the results of a subsequent study by Dr. Gudmundsson (No 131 of this publication series) of ice flow at a glacier confluence.

This research has been funded by the Swiss National Science Foundation.

Almut Iken

Contents

List of Figures

List of Tables

List of Symbols

Dimensional quantities are usually in lower case letters and non-dimensional quantities in capital letters.

A	softness parameter, a constant in Glen's flow law
A_m	Morland's A parameter, defined through Eq. A.6
a	amplitude of a sine wave
a_p	channel width
B	hardness parameter, $B = A^{-1/n}$
b_p	channel depth
c	heat capacity
$c_i(\delta, n)$	Taylor coefficients of the sliding function
C	parameter in Weertman-type sliding law
C_0	Clausius-Clapeyron constant, relating the depression of the melting-point to the pressure
d	one half of glacier width
e	total strain
f	form factor
g	acceleration of gravity
$g(.)$, $\hat{g}(.)$	some unknown functions
h	glacier thickness
k	wavenumber
k_*	controlling wavenumber $\sqrt{\frac{L}{2\eta C_0 (K_I + K_B)}}$
K	thermal conductivity
L	Latent heat of fusion per unit volume of ice
m	parameter in Weertman's sliding law
n	parameter in Glen's flow law
u_b	basal or sliding velocity
U_b	nondimensional sliding velocity, $u_b = A\tau_b^n \lambda U_b$; note: $U_b = s(\varepsilon, \delta, n)\pi\varepsilon^{-n-1}$
u_s	surface velocity
p	mean normal pressure, for incompressible media defined as: $p := -\frac{1}{3}\sigma_{ii}$
p_a	atmospheric pressure
p_∞	overburden pressure
q	ice flux
Q	non-dimensional discharge, $q = 2A\tau_b^n R^3 Q$, or the geothermal head flux
R	in Sub-sec. 5.1.3 channel radius

$R^{\max}(\varepsilon, \delta)$	$R^{\max}((\varepsilon, \delta) := \frac{U^{\max}_{\pi/2} - U(3\pi/2,0)}{U(3\pi/2,0)}$
$R^{\min}(\varepsilon, \delta)$	$R^{\min}(\varepsilon, \delta) := \frac{U^{\min}_{3\pi/2} - U(3\pi/2,0)}{U(3\pi/2,0)}$
r	roughness; $r := a/\lambda$
$s(\varepsilon, \delta, n)$	sliding function; $s(\varepsilon, \delta, n) := \varepsilon^{n+1} k u_b / 2A\tau_b^n$
t	time
$U^{\max}_{\pi/2}$	the local maximum of horizontal velocity immediately above a sinusoidal bed at the position $kx = \pi/2$, where $z_o = a \sin kx$
$U^{\text{saddle}}_{\pi/2}$	the saddle point of horizontal velocity immediately above a sinusoidal bed at the position $kx = \pi/2$, where $z_o = a \sin kx$
$U^{\min}_{3\pi/2}$	the local minimum of horizontal velocity immediately above a sinusoidal bed at the position $kx = 3\pi/2$, where $z_o = a \sin kx$
$u(r)$	longitudinal channel velocity
V_X, V_Z	scaled velocities, defined as $(V_X, V_Z) = (v_x, v_z)/u_b$,
v	speed; $v = \sqrt{v_x^2 + v_y^2 + v_z^2}$
v_h	horizontal speed; $v_h := \sqrt{v_x^2 + v_y^2}$
v_i	components of velocity vector, $\mathbf{v} = (v_x, v_y, v_z) = (u, v, w)$
W	aspect ratio; $W := b_p/a_p$
$\bar{w}$	$\bar{w} := \lambda/\lambda_* = k_*/k$
x, y, z	space coordinates
X, Z	non-dimensional space coordinates; $(X, Z) = k(x, z)$
$Z_{\text{critical}}(\pi/2, \delta)$	the Z coordinate of $U^{\text{saddle}}_{\pi/2}$ and $U^{\max}_{\pi/2}$ at $\varepsilon = \varepsilon_{\text{critical}}$
z_0	position of glacier bed

α	surface slope
$\beta(x)$	local bedrock slope; $\tan\beta(x) = dz_0(x)/dx$
β_{ij}	regression coefficients
β_1	$\beta_1 := \frac{\bar{w}^2}{\bar{w}^2+1}$
δ	thinness parameter; $\delta := (kh)^{-1}$
δ_{ij}	Kronecker delta
$\dot{\epsilon}_{ij}$	components of strain-rate tensor; $\dot{\epsilon}_{ij} = \frac{1}{2}(v_{i,j} + v_{j,i})$
$\dot{\epsilon}_3^s$	vertical surface strain rate
$\dot{\epsilon}$	effective strain rate; $\dot{\epsilon} := \sqrt{\frac{1}{2}\dot{\epsilon}_{ij}\dot{\epsilon}_{ij}}$
ε	local bed-slope parameter, $\varepsilon := ak$
$\varepsilon_{\text{critical}}$	$v(x,y)$ will only have stationary points at $X = \pi/2$ for some δ if $\varepsilon < \varepsilon_{\text{critical}}(\pi/2, \delta)$
η	viscosity
η_{eff}	effective viscosity
κ	thermal diffusivity; $\kappa = K/\rho c$
λ	wavelength
λ_*	transition wavelength
ρ	specific density
σ'_{II}	second deviatoric stress invariant; $\sigma'_{II} := \frac{1}{2}\sigma'_{ij}\sigma'_{ij}$
σ_{ij}	components of stress tensor
σ'_{ij}	components deviatoric stress tensor, $\sigma'_{ij} := \sigma_{ij} - \frac{1}{3}\delta_{ij}\sigma_{kk} = \sigma_{ij} + p$
σ_n	component of the stress tensor normal to the bed
σ'_n	component of the deviatoric stress tensor normal to the bed
σ_p	component of the stress tensor parallel to the bed
σ'_p	component of the deviatoric stress tensor parallel to the bed
ς	asperity; $\varsigma := \lambda/h$
τ	effective stress; $\tau := \sqrt{\sigma'_{II}}$
τ_b	basal shear stress or driving stress; $\tau_b := \rho_I g h \sin\alpha$

Suffices

I	properties of ice
B	properties of bedrock
b	basal properties
p	parabolic

Abstract

The characteristics of creeping flow close to bed undulations, and the form of the sliding law, in the absence of friction, bed separation and regelation, are analyzed. This is done by an analytical and numerical treatment of a non-linear medium flowing over a sinusoidal bed. The main theoretical results of relevance obtained to date, which are usually only valid in the case of a linear rheology, are given, and emphasis is placed on what can be learned from them about flow behavior close to the bed. An estimate of the pressure variation along the bed and of an effective viscosity is used to obtain a sliding law for a non-linear medium valid in the limit of small roughness and infinitely thick glaciers. Solutions based on a second order perturbation analysis for the velocity field are presented and examined for a sinusoidal bed. It is found that close to bedrock undulations, depending on the amplitude-to-wavelength ratio, two different regions of extrusion flow may arise. Above the crest of the sine wave a region of local maximum, and within and above the trough a region of local minimum of the vertical velocity can develop, and exact criteria for the appearance and disappearance of these stationary points are given. Extrusion flow will cause a reversal of bore-hole inclination profiles close to the bedrock. This has been observed in nature but its cause has not so far been fully understood.

Numerical calculations are performed to extend the analytical results to the case of non-linear rheology and a strongly undulating bed. The general form of the sliding law for a sinusoidal bed for every possible roughness and n value (n is a parameter in Glen's flow law) is found, and the effect of the ratio of glacier thickness to bedrock wavelength is analysed. Extrusion flow is found to become increasingly important as the flow gets progressively more non-linear. For high roughness values a flow separation occurs, *i.e.* the main flow sets up a secondary flow circulation within the trough, and the ice participating in this circular motion theoretically never leaves it.

Zusammenfassung

Die Fließeigenschaften eines kriechenden Mediums in der Nähe von Bettunebenheiten mit analytischen sowie mit numerischen Methoden untersucht. Dabei wird angenommen, daß zwischen dem Bett und dem Medium keine Reibung stattfindet. Nur der Fall indem sich das Medium vom Bett nicht ablöst, wird betrachtet. Regelation wird ignoriert. Ein Überblick über die bisherigen theoretischen Ergebnisse, die sich in der Regel auf den linearen Fall beschränken, wird gegeben. Eine Abschätzung der Druckschwankung am Bett und der effektiven Viskosität wird benutzt um zu einem Gleitgesetz zu kommen das für den nicht-linearen Fall und kleine Rauhigkeiten gültig ist. Neue Lösungen für das Fließ- und das Spannungsfeld, die auf einer Störungstheorie zweiter Ordnung basieren, werden präsentiert, und die werden für den Fall eines sinusförmigen Gletscherbettes untersucht. Es zeigt sich, daß je nach dem Verhältnis der Amplitude der Bettunebenheiten zu deren Wellenlänge, sich bis zu zwei Zonen bilden können, an denen die horizontale Geschwindigkeit mit der Tiefe zunimmt. Oberhalb des höchsten Punktes des sinusförmigen Bettes kann ein lokales Geschwindigkeitsmaximum entstehen, und oberhalb des tiefsten Punktes kann sich ein lokales Geschwindigkeitsminimum bilden. Genaue Kriterien für dieses Fließverhalten werden gegeben. Diese Art vom Fließverhalten ist schon in der Natur beobachtet worden, aber bisher waren keine theoretischen Erklärungen bekannt.

Anhand von numerischen Berechnungen werden die analytischen Resultate auf den nicht-linearen Fall und große Rauhigkeiten erweitert. Die allgemeine Form des Gleitgesetzes für ein sinusförmiges Bett in Abhängigkeit des Rauhigkeitsparameters und dem Grad der Nichtlinearität wird bestimmt. Ebenfalls wird der Einfluß einer endlichen Gletschermächtigkeit auf das Gleiten untersucht und quantifiziert. Für sehr hohe Rauhigkeiten kann in einer Übertiefung eine zirkulierende Strömung einsetzen. Das Eis, das sich in einer solchen zirkulierenden Strömung befindet, wird die Übertiefung nie verlassen.

CHAPTER 1

Introduction

1.1 Basal sliding and flow close to bedrock

Glacier flow consists of three elements: internal deformation of the ice, the rheology of may be described mathematically by Glen's flow law, basal sliding, and deformation of the underlying substrate. The sliding motion is often responsible for a large part of the flow velocity of temperate glaciers, and is therefore a subject of vital importance to the understanding of glacier behavior. The dependency of the sliding velocity on physical conditions at the ice-bed interface is still an open question. There have been many proposals for sliding laws, but so far there seems to be no general consensus on what are the pertinent variables governing the sliding velocity, let alone the form of the sliding law. Without a theoretically and experimentally well-founded sliding law, realistic basal boundary conditions for a model of glacier flow are not known and have to be introduced in an *ad hoc* manner.

For a numerical flow model, sliding is a sub-grid process (for the grid densities which are currently practicable); sliding law is then expected to give the contribution of all sub-grid processes to an average basal velocity u_b (where the averaging distance is of the same order as the distance between two grid points), as a function of some quantity calculated by the numerical model, as an average over a characteristic grid dimension such as the average basal shear stress τ_b. In general the sliding law has therefore the form:

$$\tau_b = f(u_b) \tag{1.1}$$

where f is some unknown functional representing the sliding law. The search for a sliding law is a search for a matching condition for the local (sub-grid scale) flow and the large-scale flow as has been stressed by Fowler (1986). Properties of the local flow determine and give the boundary conditions, *i.e.* the sliding law, for the large-scale flow.

For any particular glacier the physical conditions at the bed-rock interface as well as factors known to influence the sliding velocity — the form of the bed, water pressure, debris concentration *etc.* — are in general, not known. It will hence be difficult to obtain information on the functional dependency of the sliding velocity on for example the bed roughness spectrum through measurements. This illustrates the usefulness, indeed the need for a theoretical work on sliding.

A short overview of previous work on the form of the sliding law and on flow characteristics close to bedrock undulation, in the presence of sliding, is given in Sections 2.2 and 2.3 respectively.

The only process so far analysed in such detail that it can be considered to be formally understood is the sliding of a Newtonian fluid over a perfectly smooth wavy surface in the limit of small roughness, which can be solved with standard perturbation methods. The sliding velocity for high roughness values, even for this highly idealized model, is not known. It is not even known what roughness values should be considered to be high, *i.e.* how accurate the perturbation solutions are as a function of r, where r is the amplitude/wavelength ratio. No bounds on the accuracy of linear, as well as non-linear sliding laws using Glen's flow law, proposed so far, are known and it is possible (and will be shown in Sec. 6.6.1 to be true) that the range of r values where the sliding laws can be used accurately decreases as the non-linearity of the viscous medium increases.

Sliding over hard beds, as opposed to sliding over sediments or soft beds, is an important sliding mechanism in the Alps. Frictionless sliding over a sinusoidal bed without bed separation is possibly the conceptually simplest model of sliding that can be thought of. It is difficult to see how progress toward a "general" sliding law for hard beds, including the effects of friction and bed separation, can be made before a proper theoretical understanding of the more simple type of model has been obtained. A numerical approach seems to be the only possibility of addressing this problem in its full generality, since horizontal as well as vertical stress gradients are expected to become important close to bedrock protubances and the full set of equations has to be solved. Three dimensionless quantities characterise the problem (*cf.* Sec. 3.1); two geometrical numbers describing the roughness of the bed and the relative thickness of the glacier, and one number describing the degree of the rheological non-linearity. A three-dimensional parameter space must therefore be investigated, involving repeated solution of a non-linear equation system, so that considerable computer resources are needed. This is most probably the reason why this problem has not been tackled in its full generality by numerical means so far, although valuable insights have been gained from numerical work done for several isolated cases (Raymond, 1978; Meyssonnier, 1989; Schweizer, 1989). This numerical work will be discussed in Sec. 2.2 and Sec. 2.4.

Most flow solutions, including solutions for large-scale datum flow (typical wavelength of bedrock undulation large compared to ice thickness) as well as short-scale solutions (typical wavelength of bedrock undulation comparable to ice thickness) do not calculate sliding from first principles but regard it as resulting from the local-scale flow (typical wavelength of bedrock undulation much smaller than ice thickness) in some unknown manner, and circumvent the problem by using an *ad hoc* sliding law usually of Weertman type

$$u_b = C\tau_b^m \tag{1.2}$$

where m and C are adjustable parameters. Although this law has mathematically the same form as Glen's flow law it does not have the same experimental status (Lliboutry, 1968). The important point here is that the amount of basal sliding is not an output but an input of most flow solutions. This makes perfect sense for large-scale flow models but may be somewhat questionable for short-scale solutions.

Given the current state of affairs there seems, however, to be no other way of tackling the effect of sliding on the flow.

Little is known about the local flow properties close to bedrock undulations in the presence of sliding even for the linear case, and almost nothing for a non-linear medium (*cf.* Sec. 2.3). Because of the inherent complexity of the problem, only a few analytical solutions exist. These solutions often apply to somewhat idealized conditions at the rock bed but nevertheless give a valuable insight in to the nature of the flow. Again only flow properties for small roughness are known and numerical work has been limited to a few cases.

Measurements of the deformation of bore hole give information on the rheological properties of ice. Since shearing is usually concentrated at the lower most section, directly above the bed, it is important for the interpretation of bore-hole deformation data to know how ice deforms around bedrock protrubances. Some surprising observations, which require an explanation have been made. Extrusion flow close to the bed has been demonstrated by bore-hole measurements (*i.e.* close to bed the velocity increased with depth) (Hooke *et al.*, 1987), which could possibly be caused by the presence of bedrock undulations. Extrusive flow has also been observed within subglacial sediments (Blake *et al.*, 1992).

Flow through an overdeepening has been the object of increased interest with the recent finding in the Alps of a corpse buried in ice, which was dated to be about 5000 years old. The fact that the corpse was found to be lying in an overdeepening suggests a way of how it could have been situated there for such a long time. In this context it is especially interesting to know to what extent ice flows over an overdeepening without activating the ice within it. This will of course be dependent on the depth-to-width ratio. A sinusoidal bed is a convenient idealization of this type of geometry. To what extent the ice lying in the overdeepening participates in the general flow and for how long it stays within it depends on the exact boundary conditions, but a lower limit to the time it stays there and an upper limit on the flow velocity is obtained by assuming no friction at all, *i.e.* perfect sliding.

1.2 Goals of the study

The goals of this study are twofold: (i) to investigate and determine the dependency of the sliding velocity on bedrock roughness and rheological non-linearity, and (ii) to analyse the characteristics of glacier flow close to bedrock undulations in the presence of sliding.

To this end a study of an idealized glacier having a sinusoidal bed given by $z_0 = a \sin kx$, where z_0 is the vertical position of the bed, a the amplitude and k the wavenumber, will be done. The single wave *roughness* is defined as the ratio of the amplitude to the wavelength and will be denoted by r, *i.e.* $r := a/\lambda$, where $\lambda = 2\pi/k$. Another convenient measure of the roughness is the *local bed-slope parameter* ε defined as $\varepsilon := ak$. The ratio of the glacier thickness h to the bed wavelength is expected to influence the sliding behavior. The *thinness* parameter δ is defined as $\delta := (kh)^{-1}$.

Attempts should be made to find answers to questions such as:

- Is $u_b \propto 1/\varepsilon^{n+1}$ for $\varepsilon \to 0$, and if that is true, for what range of ε values can this relation be used? Does the range depend critically on n?
- What are the effects of δ on u_b other that those entering the sliding law through τ_b? Does δ influence u_b significantly or can it for practical purposes be ignored?
- How does u_b depend on ε for $\varepsilon \not< 1$?
- Is extrusion flow close to bedrock undulations possible?
- How does ice flow through an overdeepening? At what ε values does ice effectively remain within the trough?
- Is flow separation possible?

Another goal of the study is to test the feasibility of the FE method for flow calculations involving sliding, and to develop programs that automate the calculation of sliding velocities for a general bed geometry.

1.3 Organization

In Chapter 2 a specification of the problem that forms the subject of this work is given. Previous work is discussed, with an emphasis on the linear first order theory of Nye and Kamb.

Chapter 3 focuses on what is known about the form of the sliding law for a non-linear medium, and what can be learned from simple dimensional arguments. An estimate of the effective viscosity is used to show how strongly the sliding velocity depends on the slope parameter ε.

The second order solution of Morland for the flow along the sole-bed interface is extended in Chapter 4 to the region above the bed-line. It is shown that the solution so found displays a number of interesting properties.

For a non-linear flow law of the type mostly used in flow modeling, *i.e.* Glen's flow law, analytical solutions have not been found. The only way at present of obtaining a better understanding of this important problem seems to be through the use of numerical models. In Chapter 5 a testing of the correctness of numerical results obtained with the FE program MARC is described. This program was used for numerical calculations of flow over a perfectly lubricated sinusoidal bed.

In Chapter 6 the numerical results are presented and discussed.

A summary of the results is given in Chapter 7.

CHAPTER 2

Previous Work

In this chapter an exact description of the idealized problem of a glacier flowing over a perfectly lubricated sinusoidal bed is given. This includes a mathematical description of ice as a highly viscous isotropic and homogeneous material. Previous work on sliding, with emphasis on sliding without bed separation and regelation, is summarized.

2.1 Description and specification of the problem

2.1.1 Ice dynamics

Laboratory experiments and field observations suggest a constitutive law for ice of the form

$$\dot{\epsilon}_{ij} = A \, \sigma_{II}^{'(n-1)/2} \sigma_{ij}^{'} \tag{2.1}$$

where $\dot{\epsilon}_{ij}$ are strain rates, $\sigma_{ij}^{'}$ deviatoric stresses,

$$\sigma_{ij}^{'} := \sigma_{ij} - \frac{1}{3}\delta_{ij}\sigma_{kk} \tag{2.2}$$

$\sigma_{II}^{'}$ the second invariant of the deviatoric stress tensor

$$\sigma_{II}^{'} := \frac{1}{2}\sigma_{ij}^{'}\sigma_{ij}^{'} \tag{2.3}$$

and δ_{ij} is the Kronecker delta. A and n are parameters determined by measurements. Unfortunately the values of A and n are only approximately known. Often n is assumed to have the value 3, although the experimental basis for this is not strong. A, which is sometimes called the *softness parameter*, is a thermodynamic property and varies strongly with temperature. Other factors such as ice fabric, ice composition and chemical state and, for temperate ice, moisture content, are also known to be important and to influence the value of A, *e.g.* Lile (1978), Budd and Jacka (1989), van der Veen and Whillans (1990). Sometimes the *hardness parameter* $B = A^{-1/n}$ is used instead of A. This type of constitutive law is known in metallurgy as Norton-Hoff's power law, in general fluid dynamics literature as the Ostwald-de Waerde or Reiner power law, but as Glen's flow law in the glaciological literature (Hutter, 1991). Glen (1952, 1955) and Steinemann (1958a, 1958b) showed for the first time the necessity of a non-linear flow law for ice. Generalisation of Glen's experimental results — that were done with a stress state of uniaxial compression — by Nye (1953, 1957) resulted in the above shown flow law.

All glacier flow must obey the fundamental laws of conservation for a physical system, *i.e.* the conservation of mass, linear and angular momentum, and of energy. Since the density of ice can be assumed to be constant, conservation of mass is equivalent to conservation of volume.

Continuity equation (mass conservation):

$$v_{i,i} = 0. \tag{2.4}$$

Equation of motion (conservation of linear momentum):

$$\sigma_{ij,j} + \rho_i g_i = 0. \tag{2.5}$$

The acceleration term is ignored since it is truly small compared to other terms.

Energy equation (conservation of energy):

$$\rho c \frac{DT}{Dt} = KT_{,ii} + \sigma_{ij}\dot{\epsilon}_{ij}, \tag{2.6}$$

where D/Dt is the substantial derivative[1], c the heat capacity, and K the thermal conductivity. In Eq. (2.6) use has been made of one constitutive equation, *i.e.* Fourier's law of heat conduction. Since the ice will be assumed to be temperate, the temperature will be determined by the Clausius-Clapeyron relation, and Eq. (2.6) is inappropriate. The energy released by viscous dissipation will increase the moisture content and not raise the temperature. The softness parameter A is expected to be a function of moisture content (Lliboutry, 1976) but this will be ignored here. Only spatial variations of A within the basal layer will affect the results presented. It is not clear that the influence of spatial variation of moisture content on A will dominate other factors on which A depends, such as salt, air-bubble and debris content, which can either increase or decrease the value of A, and which will also be neglected. A theoretical formulation of temperated ice masses that accounts for the interaction of ice and water has been given by Hutter (1993) and numerical work has been done by Hutter *et al.* (1988).

2.1.2 Problem definition

Consider a glacier, thought of as a highly viscous material, sliding slowly and steadily over a sinusoidal bed. Inertia forces are negligible. The sliding is perfect in the sense that there is no tangential traction at the bed. The beds exert only normal forces. No bed separation occurs and regelation is neglected.[2] The problem is depicted in Fig. 2.1. The bed profile is given by

$$z = z_0 := a \sin kx. \tag{2.7}$$

[1] $D/Dt := \partial/\partial t + v_i \partial/\partial x_i$. Other names for the substantial derivative are the particle derivative and the material derivative.

[2] For real glaciers regelation is expected to be important at wavelengths smaller than the transition wavelength (Weertman, 1957; Weertman, 1964; Weertman, 1979).

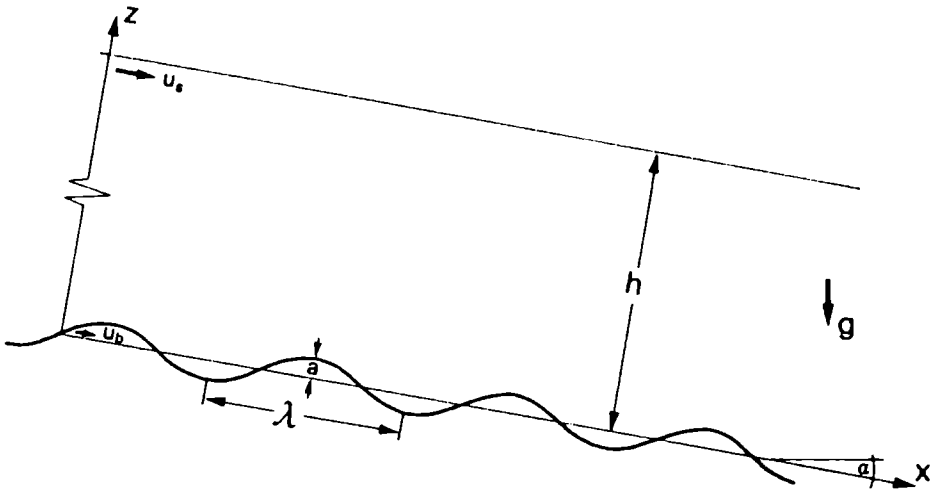

Fig. 2.1: Flow over a sinusoidal bed. The coordinate system makes the angle α with respect to the horizontal. The vertical position of the bed line z_0, is given by: $z_o = a \sin kx$. The sine wave has the wavelength $\lambda = 2\pi/k$, and amplitude a. The surface velocity is denoted by u_s and the sliding velocity by u_b. h is the glacier thickness.

2.2 Previous work on the form of the sliding law

Weertman (1957) was the first to put forward a theory of glacier sliding. Later he refined and defended his model (Weertman, 1964; Weertman, 1971). He distinguished between two fundamentally different physical processes. The first is regelation, whereby pressure variations around a bed obstacle cause a melting on the up-stream side and refreezing at the down-stream side. The second is local viscous deformation of ice around bed obstacles.[3] For a given driving stress τ_b Weertman found the regelative and the viscous components of the ice velocity to be proportional to τ_b and τ_b^n respectively, where n is the exponent in Glen's flow law.

Lliboutry (1959, 1968, 1979, 1987b) argued that ice deformation, where the ice separates from the bed, forming water filled cavities, is an important sliding mechanism. Bed separation reduces friction and causes larger sliding velocities.[4] Variations of water pressure cause a change in the extent of bed separation and must be linked to changes in sliding velocity (Iken, 1981). Measurements have confirmed this (Iken and Bindschadler, 1986). The magnitude of sliding with bed separation must depend on the water pressure in one way or another. Theoretical work has been done by Fowler (1986, 1987) that produced a complex sliding law for bed with power-law roughness spectra $r(\lambda) \propto \lambda^l$. Further work has been done by Kamb (1987),

[3]Weertman used the term *enhanced plastic flow* to describe this mechanism that I call *local viscous deformation*. I do not use the word plastic because the flow is not plastic (for $n > 1$ Glen's flow law represents a pseudo-plastic stress-strain relationship (White, 1991, p. 24-25)), and the word enhanced does not seem necessary since it is not clear with respect to what the flow is being enhanced.

[4]I use the term bed separation instead of the word cavitation since cavitation is used in fluid mechanics to denote another physical mechanics, namely the spontaneous creation of air bubbles within a fluid as the fluid pressure becomes locally lower than the vapor pressure (Hutter, 1983).

Humphrey (1987) and Schweizer and Iken (1992). A recent overview has been given by Kamb (1993).

Various attempts to estimate the relative importance of regelation and ice deformation with and without bed separation have all shown that regelation is only expected to be of importance at small distance scales (Weertman, 1957; Nye, 1969; Fowler, 1986). For a given ratio of the amplitude of the bedrock undulations to the distance between them, sliding due to regelation is inversely proportional to wavelength, but sliding caused by ice deformation increases linearly with wavelength. This is the motivation for Weertman's notion of a controlling obstacle length, where the contribution to sliding by regelation and ice deformation is the same. By simple dimensional analysis and assuming that the contribution of regelation and ice deformation (without bed separation) can be added to the sliding velocity, one finds

$$\frac{u_b}{\tau_b} = \hat{c}_0 \frac{\lambda}{\eta} + \hat{c}_1 \frac{C_0 K}{L\lambda}, \tag{2.8}$$

where λ is the wavelength of the undulation (or the distance between the obstacles), η is the viscosity of the ice, which for a non-linear material could be substituted by an effective viscosity, C_0 is the Clausius-Clapeyron constant, K the mean thermal conductivity of ice and bedrock, and L is the latent heat of fusion per unit volume of ice. $\hat{c}_0$ and $\hat{c}_1$ are some unknown constants, that in general will be some unknown function of all the dimensionless numbers and ratios entering the problem, such as the roughness $r := a/\lambda$, the ratio of the wavelength to the thickness of the glacier, and a possible non-dimensional number entering the flow law.

Nye (1969, 1970) and Kamb (1970) considered the flow of a linear viscous medium over a perfectly smooth sinusoidal bed without bed separation, and derived a first order perturbation solution for the flow and for the stress field. This solution will be discussed in Section 2.3.1. For a single sine wave Nye and Kamb found

$$\frac{u_b}{\tau_b} = \frac{1}{\eta\varepsilon^2 k} + \frac{2C_0(K_I + K_B)k}{L\varepsilon^2}, \tag{2.9}$$

where k is the wave number ($k = 2\pi/\lambda$), $\varepsilon := ak$ is the *local bed-slope parameter* ($\varepsilon = 2\pi r$), and K_I and K_B are the thermal conductivities of ice and bedrock respectively. The first term on the right-hand side represents sliding due to pure viscous flow and the second sliding caused by regelation. The equation can only be used for $\varepsilon \ll 1$. The transition wavelength λ_* is given by

$$\lambda_*^2 = \frac{8\pi^2 \eta C_0 (K_I + K_B)}{L} \tag{2.10}$$

and is of the order of 0.5 m. Morland's (1976a) second order linear perturbation theory gave the same result. If roughness is absent at wavelengths smaller than λ_*, regelation can be ignored in the calculation of sliding velocities, and the sliding velocity is proportional to τ_b^n. Conversely, if the bed roughness is concentrated at short wavelengths ($\lambda < \lambda_*$), then $u_b \propto \tau_b$. For a bed consisting of a single sine wave with $\lambda = \lambda_*$, Weertman (1957) showed that $u_b \propto \tau_b^{(n+1)/2}$. The heat transfer associated with the regelation process was calculated by assuming it to be

caused by pure conduction through rock and ice only, which can be justified to some extent by the thinness of the water film estimated to be about 1 μm (Nye, 1967; Lliboutry, 1968; Fowler, 1981). A more accurate estimate of melting and refreezing by regelation is difficult as the ice salt and air-bubble content, water inclusions, moisture content and surface properties of the bedrock must be accounted for (Drake and Shreve, 1973; Chadbourne *et al.*, 1975; Morris, 1976; Shreve, 1984; Meyssonnier, 1989).

Kamb (1970) developed an approximate non-linear theory of sliding, which will be discussed briefly in Sec. 3.3. He made the assumption that the effective viscosity is a function of the distance above the bed only, and found that the transition length is somewhat smaller for $n > 1$ than for $n = 1$, where n is a constant in Glen's flow law.

Fowler (1981) made a rational dimensional analysis of the sliding of glaciers in the absence of bed separation, including the non-linearity of the flow law. For the transition length he found a value of the order of 0.01 m and concluded that the regelative component of the ice velocity may therefore be neglected, provided roughness is absent at lowest wavelengths.

By using a variational theorem for non-Newtonian flow found by Johnson (1960), Fowler (1981) derived a sliding law valid for a non-linear medium, concluding that the sliding velocity u_b should be proportional to the ratio δ/ε^{n+1}, where $\delta = 1/kh$ and h is the glacier thickness. A sliding law with the same functional dependence on ε had earlier been derived by Lliboutry (1968) using simple physical arguments.

That u_b is so highly dependent on ε for $n = 3$, the value of n mostly used for ice flow modeling, is striking. This has, however, been questioned by Schweizer (1989) who, through FE calculations, found u_b to be less dependent on ε than $u_b \propto 1/\varepsilon^{n+1}$ indicates.

Raymond (1978), in what seems to be the first numerical calculation of this problem, calculated the sliding velocity for a perfectly lubricated sinusoidal bed with no regelation using Glen's flow law. His calculations were limited to a few ε values and they do not give the sliding velocity as a general function of ε, δ, and n, but they stand in an agreement with $u_b \propto 1/\varepsilon^{n+1}$.

Meyssonnier (1983) did a comprehensive numerical study of this problem, and compared numerical calculated sliding velocities with analytical estimates. His important work will be discussed in Section 3.2.

2.3 Previous work on flow characteristics close to bedrock undulations

2.3.1 The linear first order theory of Nye and Kamb

Nye and Kamb, and later, in a somewhat more general way, Morland (1976), have found an approximate solution to the problem of a highly viscous Newtonian fluid

sliding over a smooth bed. The assumption of a Newtonian fluid was necessary in order to be able to use standard perturbation methods. Morland has also considered the effect of friction on the flow (Morland, 1976b).

The method of Nye and Kamb will now be briefly outlined, mainly in order to point out the approximations that had to be made in order to obtain the solution.

A solution for the velocity $\mathbf{v} = (u, w)$ and the pressure p is sought in the form

$$u = u_b + \sum_{i=1}^{\infty} \varepsilon^i u_i(x, z), \tag{2.11}$$

$$w = \sum_{i=1}^{\infty} \varepsilon^i w_i(x, z), \tag{2.12}$$

$$p = \sum_{i=1}^{\infty} \varepsilon^i p_i(x, z), \tag{2.13}$$

where $\varepsilon = ak$. One may think of ε as some small number, $\varepsilon \ll 1$. The bed profile is given by

$$z = z_0 := a \sin kx =: \varepsilon f(x). \tag{2.14}$$

At the upper boundary where $z = z_1$ with $z_1 \gg \lambda$, a shear stress τ is applied. This is the driving force of the motion, not gravity, which is not present. The idea here is that the force of gravity acting in the layer close to the bed will be negligible compared to the force that the overlaying ice is exerting on it; a good approximation for a thick glacier, that is if $\delta \approx 0$. This means that close to the upper boundary the horizontal velocity varies linearly with z. On the lower boundary, $z_0 = a \sin kx$, there are two conditions imposed: the velocity normal to the bed is zero,[5] and there is no tangential traction. This means that

$$-u\frac{dz_0}{dx} + w = 0 \quad , \quad \text{on} \qquad z = z_0, \tag{2.15}$$

and that

$$\sigma_{xz} = \frac{1}{2}(\sigma_{xx} - \sigma_{zz}) \tan 2\beta(x) \quad , \quad \text{on} \qquad z = z_0, \tag{2.16}$$

where $\tan \beta(x) := dz_0(x)/dx$. These exact boundary conditions are now applied not at the real boundary $z = z_0$, but at $z = 0$. By inserting $z_0 = \varepsilon f(x)$ and the expressions (2.11) and (2.12) into Eq. (2.15), and by only taking terms up to order ε, one obtains, since z_0 is $O(\varepsilon)$:

$$-u_b f'(x) + w_1(x, 0) = 0. \tag{2.17}$$

The second boundary condition can be approximated in a similar way. Since both $\sigma'_{xx} = (\sigma_{xx} - \sigma_{zz})/2$ and $\tan 2\beta(x)$ are $O(\varepsilon)$, the boundary condition (2.16) becomes

$$\sigma_1(x, 0) = 0; \tag{2.18}$$

writing σ_{xz} as

$$\sigma_{xz} = \varepsilon\sigma_1 + O(\varepsilon^2). \tag{2.19}$$

[5] In the presence of regelation this is not correct and there is a non-vanishing velocity component normal to the bed. Regelation was taken into account by Nye and Kamb, but it is ignored here.

Or if expressed in terms of $\mathbf{v} = (u, w)$

$$w_1 = u_b f'(x) \quad \text{and} \quad \frac{\partial u_1}{\partial z} = -u_b f''(x), \quad \text{on} \quad z = 0. \tag{2.20}$$

The expressions for the velocity and the pressure are now substituted into

$$\eta \nabla^2 \mathbf{v} = \nabla p \quad \text{and} \quad \nabla \cdot \mathbf{v} = 0 \tag{2.21}$$

the conservation laws of linear momentum and mass.

After having collected the first order terms the solution is obtained by usual Fourier integral methods. In the special case of a bed consisting of a single sine wave these first order perturbation solutions are:

$$u_b = \frac{\tau_b}{\eta a^2 k^3}, \tag{2.22}$$

$$v_x(x, z) = u_b + u_b a k^2 z e^{-kz} \sin kx + O(\varepsilon^2), \tag{2.23}$$

$$v_z(x, z) = u_b k(1 + kz) e^{-kz} a \cos kx + O(\varepsilon^2), \tag{2.24}$$

$$p(x, z) = p_\infty + 2\eta u_b k^2 e^{-kz} a \cos kx + O(\varepsilon^2), \tag{2.25}$$

$$\sigma'_{xx}(x, z) = -\sigma'_{zz} = 2\eta u_b k^3 z e^{-kz} a \cos kx + O(\varepsilon^2), \tag{2.26}$$

$$\sigma_{xz}(x, z) = -2\eta u_b k^3 z e^{-kz} a \sin kx + O(\varepsilon^2), \tag{2.27}$$

$$\tau(x, z) = 2\eta u_b a k^3 z e^{-kz} = 2\tau_b \frac{z}{a} e^{kz} + O(\varepsilon^2), \tag{2.28}$$

where $\tau := \sqrt{\sigma'_{II}}$, which is sometimes called the *effective stress*, and p_∞ is the pressure applied at the upper boundary of the medium.

These expressions have some interesting features. One of them is the fact that the second invariant of the deviatoric stress tensor, Eq. (2.28), shows no dependence on x. This will of course also apply to the second strain-rate tensor invariant.

Another interesting feature of the linear solutions above is the occurrence of *extrusion flow*; there is a region close to the bed where the horizontal velocity increases with depth. At the point $kx = 3\pi/2 + 2\pi l$ where $l \in N$ and $z = z_{\min} := 1/k$, v_x has a local minimum:

$$v_{\min} := v_x(x = 3\pi/(2k), z = 1/k) = u_b(1 - ak/e). \tag{2.29}$$

From here downwards to the bed the horizontal velocity increases. This is a remarkable fact, which deserves a closer inspection. Notice that since $ak \ll 1$, it follows that $z_{\min} \gg a$. Extrusion flow, a term introduced by Demorest (1941, 1942) has been a subject of some debate in the glaciological literature. On theoretical grounds it can easily be shown that a *global* extrusion flow, that is an increase of the horizontal velocity with depth throughout an entire glacier, is impossible since the overlying mass will then experience a force in the main direction of flow, which is not counterbalanced by any other force, leading to an accelerating velocity (Nye, 1952). There are, on the other hand, claims of extrusion flow having been directly observed

by bore-hole deformation measurements (Hooke *et al.*, 1987), and by observations within sub-glacial caves close to the bed-rock interface (Carol, 1947). Arguments supporting (global) extrusion flow based on mass-balance measurements have also been given (Streiff-Becker, 1938; Seligman, 1947). These arguments must, however, be considered to be rather weak, because no direct information on the velocity field was available.

Because the solution of Nye and Kamb is only approximate, one might be tempted to believe that this occurrence of extrusion flow may only be an artifact due to its inexact nature, and that a more complete treatment where second order perturbation terms are included will eliminate this feature. The inclusion of gravity as the driving force of the motion, instead of a given shear stress at the upper boundary, will modify the velocity profile so that it no longer varies linearly with depth at some distance above the bed and that would also affect this situation.[6] A somewhat more realistic theory is needed to clarify these matters. In Sec. 4.1 the second order solution of Morland (1976a) will be used to calculate the velocity and the stress field as functions of x and z (Morland only gave the solution along the bed, *i.e.* $z = 0$) and the solutions will be analysed with respect to the possibility of extrusion flow.

2.4 Numerical work

Raymond (1978), Meyssonnier (1983), and Schweizer (1989) did FE calculations of flow over a simple sinusoidal bed.

Raymond found the excess of velocity in comparison with a no slip situation to depend on height above bed, which he ascribed to an effective softening of the basal ice for $n > 1$. He also found the deformation to be concentrated more closely near the bed for non-linear than linear behavior.

Meyssonnier obtained a point of maximum relative horizontal velocity that was situated above the peak of the sine wave. This point did not appear in all his calculations, for which the reason is not clear.

[6] It is interesting that neither Nye nor Kamb mentioned the feature of there solutions which suggests the existence of extrusion flow for an infinitely wide glacier at small asperity and roughness values. My guess is that they thought of it as an artifact of no relevance for glacier flow.

CHAPTER 3

Sliding Law for a Non-Linear Medium

No analytical solutions exist for the flow over a sinusoidal bed of a power law medium with $n \neq 1$. Despite this fact some information on the form of the sliding law can be obtained through the use of dimensional analysis and variational theorems.

3.1 Dimensional arguments

The relevant variables are: the glacier thickness (h), the wavelength of the sinusoidal bed (λ), the amplitude of the sine function (a), the mean slope (α), the driving stress ($\tau_b = \rho_I g h \sin\alpha$) — which is equal to the mean drag — and the viscosity η. The sliding velocity (u_b) can only depend on these variables. That is

$$u_b = u_b(a, \lambda, h, \tau, \eta). \tag{3.1}$$

There are two dimensionless ratios that can be formed with these variables: the *roughness*, $r := a/\lambda$ and the *asperity*, $\varsigma := \lambda/h$, were h is the glacier thickness.[1] It is sometimes more convenient to use, instead of r and ς, the parameters: $\varepsilon := ak$, called the *local bed-slope parameter*[2], and $\delta := 1/kh$, which I call the *thinness parameter*. For an infinitely thick "glacier" the thinness parameter is equal to zero.[3]

The sliding velocity will in general depend on both parameters. If, however, the glacier thickness, h, is much larger than the wavelength λ and the amplitude a, it is physically reasonable to expect that the ice close to the ice-bed interface only responds to the applied stress caused by the overlying mass of ice and that it does not

[1] Fowler (1979) introduced the word asperity for ς and used the word corrugation for ε. To call the ratio of amplitude to wavelength roughness (sometimes multiplied by some numerical factor), and use the symbol r for it, has been done by many authors, *e.g.* (Nye, 1970; Kamb, 1970; Lliboutry, 1968; Schweizer, 1989; Schweizer and Iken, 1992).

[2] ε is the so called *small slope parameter* which Nye and Kamb introduced (Nye, 1970; Kamb, 1970). Here I simply call it the *slope parameter* since in what follows it will not necessarily be small, or the *local bed-slope parameter* to make it clear that it is the local slope of the bed which is being referred to.

[3] Theories of large-scale datum flow, *e.g.* shallow ice approximation (*cf.* (Hutter, 1983)) often use the symbol δ for the ratio of the vertical to the horizontal dimensions of an ice cap, which is then inversely proportional to the thinness parameter defined here and also denoted by δ. The motivation for defining δ in this way here, is that the symbol δ is usually thought to stand for some small dimensionless number, and in what follows $\delta := 1/kh$ has to be small. The assumption of $\delta \ll 1$ is not a self-imposed restriction; it is difficult to see how sliding velocity, which must be some average property of the inner flow (*i.e.* the flow close to bed) can be defined if this does not hold. The assumption $\delta \ll 1$ can be seen as part of the definition of the problem.

sense the existence of a free surface, so that the thickness h will not appear explicitly in the sliding law. In this limit of an infinitely thick glacier u_b is a nontrivial function of r only (nontrivial in the sense that this function cannot be determined by mere dimensional arguments) or equivalently of the slope parameter $\varepsilon := ak = 2\pi r$. Dimensional arguments now give

$$u_b = g(\varepsilon)\tau_b\lambda/\eta \tag{3.2}$$

or

$$u_b = \hat{g}(\varepsilon)\tau_b a/\eta, \tag{3.3}$$

where g and $\hat{g}$ are some unknown functions and τ_b is the average basal shear stress. Assuming that the rheological behavior of glacier ice can be approximated in sufficient detail by Glen's flow law

$$\dot{\epsilon}_{ij} = A\sigma_{II}^{'(n-1)/2}\sigma_{ij}^{'}, \tag{3.4}$$

where $\sigma_{II}^{'}$ denotes the second deviatoric stress invariant:

$$\sigma_{II}^{'} = \frac{1}{2}\sigma_{ij}^{'}\sigma_{ij}^{'} = \mathrm{tr}\,\frac{1}{2}\sigma^{'2}, \tag{3.5}$$

the sliding law becomes

$$u_b = U_b(\varepsilon, \delta, n)A\tau_b^n\lambda. \tag{3.6}$$

Notice that the τ_b^n dependence of u_b follows entirely from dimensional arguments and that this is the only form possible if the effects of other physical processes such as regelation, are neglected.

The unknown function U_b can, and most probably will, depend on n and δ since n and δ are dimensionless. One can think of U_b as a nondimensional sliding velocity.

3.2 The sliding law in the limit as $\varepsilon \to 0$ and for $\delta \approx 0$

It is possible to show how the sliding velocity, u_b, depends on the (local bed) slope parameter ε, and the parameter n in Glen's flow law for $\delta \approx 0$ in the limit $\varepsilon \to 0$, if one assumes that the strain rates close to the bed are mainly determined by the kinematics of the problem, and that changing n will have much more effect on the stresses than on the strains. This will be done below. Somewhat similar arguments have been given by Kamb (1970) and Lliboutry (1968). The argument given suggests a certain form of the sliding law but does not prove that it must have this form. The result has already been proved by Fowler (1986, 1987) and does not, of course, have to be proved again. The arguments used by Fowler are, however, somewhat complicated, and it is instructive to see how the form of the sliding law, can be derived in a much simpler, albeit less rigorous, way.

The idea is to express the pressure variation along the bed as a function of the amplitude, the wavelength, the sliding velocity and the viscosity. Since the rheology is non-linear the effective viscosity will be considered. It is assumed that $\varepsilon \ll 1$.

The pressure along the bed[4] is then given by

$$p(x) = p_a + \rho_I g h \cos\alpha + \delta p, \tag{3.7}$$

where

$$\delta p(x) = c_0 u_b \eta_{\text{eff}} k\varepsilon \cos kx + O((ak)^2). \tag{3.8}$$

c_0 is some unknown constant, p_a is the atmospheric pressure and η_{eff} is an effective viscosity that will be defined below. In order to see the plausibility of this expression notice that δp must vanish as $\varepsilon \to 0$. That $\delta p(x)$ depends linearly on ε can be thought to be the result of a Taylor expansion with respect to ε where only the first term is retained. This will always give a correct result if ε is small enough.[5] The product $\eta u_b k$ gives the right dimension for the pressure. It would also have been possible to use the basal shear stress τ_b to get the right dimensions, but then η would not have been a part of the expression. Notice also that k cannot be substituted by $1/a$ because if $a \to 0$, δp must vanish (another way of seeing this is that if $a \mapsto -a$, δp must change sign). It is obvious that the variation of δp with x must be of the form $\cos kx$ if ε is sufficiently small.

Now the effective viscosity η_{eff} will be estimated.

As a column of ice, which extends from the bed up to some distance l where the disturbance due to the bed undulations has disappeared, moves the distance Δx, in the time $\Delta t = \Delta x/u_b$, it is stretched/compressed to the length $l + \Delta z$, where $\Delta z = \Delta x\, dz_0/dx$. The (average) strain rate is given by

$$<\dot{\epsilon}_{zz}>= \frac{1}{\Delta t}\frac{\Delta z}{l}, \tag{3.9}$$

where the brackets are used to indicate that these are averaged strain rates over a given distance, that is

$$<\dot{\epsilon}_{ij}>:= \frac{1}{l}\int_0^l \dot{\epsilon}_{ij}\, dz. \tag{3.10}$$

For the average vertical strain rate one gets

$$<\dot{\epsilon}_{zz}>\propto \frac{1}{\Delta x/u_b}\frac{\Delta x ak\cos kx}{1/k} + O((ak)^2) = u_b ak^2 \cos kx + O((ak)^2), \tag{3.11}$$

where use was made of the fact that l must be proportional to $1/k$ since the only parameters entering the problem that have the dimension length are a and $1/k$, and that using a would again be incorrect since the strain rates must change sign as $a \mapsto -a$.[6] This expression could also have been obtained by calculating the average of the vertical strain rates over the whole glacier using the vertical strain rates from

[4]Note that the pressure at the bed is not equal to the negative of the local normal stress σ_n, *i.e.* $p \neq -\sigma_n$. This can be seen by writing the pressure as $p = -\frac{1}{2}(\sigma_n + \sigma_p)$, where σ_p is the local stress parallel to the bed, and noticing that $\sigma_n - \sigma_p = \sigma_n' - \sigma_p' \neq 0$.

[5]One could also do the following analysis to second order in ε. I have done this but it did not give any new results. Note that the first order term is needed since Nye and Kamb's solution shows that $\partial p(x)/\partial\varepsilon \neq 0$ for $\varepsilon = 0$.

[6]Notice that it is the slope of the sine curve, which has to be small if this analysis is to be correct. It is therefore ε which has to have a value of less than unity, and not $a/\lambda = \varepsilon/2\pi$.

the theory of Nye and Kamb discussed in Sub-sec. 2.3.1. Doing this for the shear strain rates gives for $<\dot{\epsilon}_{xz}>$

$$<\dot{\epsilon}_{xz}>= u_b a k^2 \sin kx. \tag{3.12}$$

The effective strain rate $\dot{\epsilon}$ is

$$\dot{\epsilon}^2 := \frac{1}{2}\dot{\epsilon}_{ij}\dot{\epsilon}_{ij} = \dot{\epsilon}_{xx}^2 + \dot{\epsilon}_{xz}^2 \tag{3.13}$$

which now turns out to be

$$\dot{\epsilon} = u_b a k^2 \sqrt{\cos^2 kx + \sin^2 kx} = u_b a k^2. \tag{3.14}$$

The Glen flow law can be written as

$$\sigma_{ij}^{'} = \frac{\dot{\epsilon}^{(1-n)/n}}{A^{1/n}}\dot{\epsilon_{ij}} = 2\eta_{\text{eff}}\dot{\epsilon_{ij}}, \tag{3.15}$$

where

$$\eta_{\text{eff}} := \frac{\dot{\epsilon}^{(1-n)/n}}{2A^{1/n}}. \tag{3.16}$$

Inserting (3.14) and (3.16) into (3.8) gives

$$\delta p(x) \propto |u_b a k^2/A|^{1/n} \cos kx. \tag{3.17}$$

Force equilibrium requires

$$\rho_I g h \begin{pmatrix} \sin\alpha \\ \cos\alpha \end{pmatrix} = \frac{1}{C(\gamma)} \int_\gamma \sigma\, \hat{n}\, ds, \tag{3.18}$$

where γ is a path along the sine curve, $C(\gamma)$ is the path length, σ is the stress tensor, and $\hat{n}$ is a unit normal vector

$$\hat{n} = \frac{1}{\sqrt{1+(dz_o/dx)^2}} \begin{pmatrix} -dz_o/dx \\ 1 \end{pmatrix}. \tag{3.19}$$

A change of variables $dx = ds(1+(dz_o/dx)^2)^{-1/2}$ gives for the drag (the x-component of Eq. (3.18))

$$\begin{aligned} \tau_b &= \frac{1}{\lambda}\int_0^\lambda (\sigma_{xz} - \sigma_{xx}\frac{dz_o}{dx})\, dx \\ &= \frac{1}{\lambda}\int_0^\lambda (p\frac{dz_o}{dx} + \sigma_{xz} - \sigma_{xx}^{'}\tan\beta)\, dx, \end{aligned} \tag{3.20}$$

where $\tan\beta = dz_o/dx$. The last term on the right-hand side is of second order in ε, and the exact boundary condition on z_0 (Eq. 2.16) shows that σ_{xz} is then of second order also. Up to first order in ε the drag can therefore be calculated according to

$$\tau_b := \rho_I g h \sin\alpha = \frac{1}{\lambda}\int_0^\lambda p(x, z_0)\, \frac{dz_0}{dx}\, dx, \tag{3.21}$$

giving

$$\tau_b = \frac{\hat{c}k}{2\pi}\int_0^{2\pi/k} (u_b a k^2/A)^{1/n} a k \cos^2 kx\, dx, \tag{3.22}$$

where $\hat{c}$ is an unknown constant. After integrating and rearranging terms one gets

$$u_b \propto \frac{2A\tau^n}{|(ak)^{n+1}k|}\hat{c}^{-n}. \tag{3.23}$$

Expression (3.23) is a remarkable result. It brings out the asymptotic $1/\varepsilon^{n+1}$ behavior of the sliding velocity as $\varepsilon \to 0$ and shows how strongly it depends on the bedrock roughness. It also encourages the definition of a new function s, which I call the *sliding function*

$$s(\varepsilon, \delta, n) := \frac{\varepsilon^{n+1} k u_b(\varepsilon, \delta, n)}{2A\tau_b^n}. \tag{3.24}$$

One can think of the function s as the sliding velocity brought to a non-dimensional form, where the asymptotic behavior for $\varepsilon \to 0$ has been accounted for. s is an even function of ε. For every particular n, $\delta \approx 0$, and $\varepsilon \ll 1$, s is a constant. In general, however, it is of course dependent on ε. From (2.22) it is seen that $s(0, 0, 1) = 1$.

Kamb (1970) found the same asymptotic behavior as in Eq. (3.23), but his derivation involved various assumptions which made it difficult to judge the general correctness of his findings. Kamb's work will be discussed in Sec. 3.3.

It wasn't until Fowler (1979), by using a variational theorem (Johnson, 1960), came to this same conclusion, that Eq. (3.23) was given a sound mathematical basis.

Lliboutry (1987b, p. 356) gave an argument somewhat similar to the one given above. His line of thought is however not easy to follow and one of his equations, which gives the basal shear stress (Eq. (13.39)) as a function of σ_{xx}, is incorrect.

Schweizer (1989), in a numerical study, came to the conclusion that the sliding velocity does not vary as $\varepsilon^{-(n+1)}$, but somewhat more slowly. His results are also not in accordance with results based on a simple dimensional analysis (Eq. (3.6)). They must therefore be, to some extent, inaccurate.

The function $s(\varepsilon, \delta, n)$ can be expressed as a Taylor series with respect to the variable ε

$$s(\varepsilon, \delta, n) = \sum_{i=0}^{\infty} c_{2i}(\delta, n)\, \varepsilon^{2i}, \tag{3.25}$$

where c_i are the Taylor coefficients.

Fowler (1981), Lliboutry (1987a) and Meyssonnier (1983) were able to estimate $c_0(0, 3)$. Meyssonnier found

$$0.305 \leq c_0(0, 3) \leq 0.338. \tag{3.26}$$

By using numerical methods to calculate the sliding velocity for values of r in the range 0.01 to 0.05 and δ in the range $0.25/\pi$ to $1/\pi$, Meyssonnier was able to give an estimate of $c_2(0, 3)$

$$c_2(0, 3) = 2.4. \tag{3.27}$$

He gave no estimate of the errors involved and did not perform a systematic investigation of the δ dependency of u_b, but concluded that it is small.

Lliboutry (1993) used a variational method to obtain an upper bound on s for $n = 3$. His result is

$$s(0,3) \leq 0.33839 + 3.688\,\varepsilon^2 + 0.169\,\varepsilon^3 \tag{3.28}$$

Eq. (3.23) shows that $s(\varepsilon, \delta, n)$ as a function of n will be equal to $\check{c}\hat{c}^{-n}$, where $\check{c}$ is some unknown number. Since $s(0,0,1) = 1$, $\check{c} = \hat{c}$, giving

$$s(,,n) = \hat{c}^{1-n}. \tag{3.29}$$

Nye's and Kamb's solution for the pressure $p(x,z)$ shows that $\hat{c} = 2$ for a linear Newtonian medium. Assuming that the effect of a non-linear flow law on the pressure variation along the bed can be described by a corresponding change in the effective viscosity, $\hat{c}$ in (3.8) will remain the same for different values of n. The estimate of the effective viscosity given above may, however, not accurately describe the effect that a change of n has on η_{eff}. The proper integration length l in (3.10) will for example depend on n if the deformation is concentrated in a different way near the bed for non-linear than for linear behavior. Important aspects of the non-linearity of the flow law such as these cannot be described simply by introducing an effective viscosity.

3.3 Kamb's non-linear sliding law

The effective stress is, as was discussed on page 25, to first order in ε independent of x. Kamb (1970) used this fact as a starting point for the development of a theory of sliding incorporating rheological non-linearity; assuming that since $\dot{\epsilon}_{II}$ is independent of x in the linear theory (where only first order perturbation terms are considered) it will also be approximately so for non-linear flow, in which case the effective viscosity distribution $\eta(z)$ for one particular wavelength is a function of z only. Kamb's expression for the sliding velocity is (Kamb, 1970, p. 703)

$$u_b = \frac{(1 + \pi^2 e^2 r^2)^{(n-1)/2}}{4\pi^{n+2} e^{n-1} r^{n+1}} \lambda A \tau_b^n \tag{3.30}$$

or

$$u_b = \frac{2^{n+1}(1 + (e\varepsilon/2)^2)^{(n-1)/2}}{4e^{n-1}} \frac{2A\tau_b^n}{\varepsilon^{n+1} k}. \tag{3.31}$$

This means that $s(0,0,3) = c_0(0,3) = 4/e^2 \approx 0.54$, a value that does not fulfill the inequality (3.26). Meyssonnier's results and those of Kamb differ, but not much. In light of the assumptions that Kamb had to make the agreement is in fact surprisingly good. Kamb's theory not only gives the correct dependency of the sliding velocity on roughness, but the numerical values are also almost correct. Kamb's non-linear theory must therefore be considered to be a successful one.[7]

[7]There is no doubt that Meyssonnier got the correct result. I have repeated Meyssonnier's calculations based on Johnson's variational theorem (Johnson, 1960), that are easy but involve some tedious work, and have got exactly the same numbers.

CHAPTER 4

Characteristics of Flow Close to Bedrock Undulations

In this chapter the flow characteristics of a highly viscous medium flowing without friction over a bed consisting of a single sinusoid will be investigated. This is done with the help of analytical solutions that are only valid for a linear medium and small roughnesses.

4.1 Morland's solutions

Morland considered the same problem as Nye and Kamb: The creeping flow of a Newtonian medium over a wavy bed. He incorporated gravity as the driving force of the motion and calculated terms to second order in ε. For the special case of a sinusoidal bed he gave expressions for the pressure field and for the velocity components at $z = 0$, but not for the velocity and the for stress field as functions of x and z. Using Morlands results one can calculate without difficulty the velocity and the stress field as functions of x and z, although somewhat laborious work is involved. Note that only flow in the absence of regelation will be discussed here. The corresponding solutions with regelation are given in Appendix A.

For the velocity field one finds

$$\begin{aligned} v_x(x,z) &= u_b + \frac{\tau_b h}{2\eta}(1-(1-z/h)^2) \\ &+ u_b a k^2 z e^{-kz}\sin kx \\ &+ u_b (ak)^2 e^{-2kz}(1/4 - kz/2)\cos 2kx + O(\varepsilon^3), \end{aligned} \tag{4.1}$$

$$\begin{aligned} v_z(x,z) &= u_b a k(1+kz)e^{-kz}\cos kx \\ &+ \frac{1}{2}u_b (ak)^2 k z e^{-2kz}\sin 2kx + O(\varepsilon^3). \end{aligned} \tag{4.2}$$

The sliding velocity is as before

$$u_b = \frac{\tau_b}{\eta a^2 k^3}. \tag{4.3}$$

The strain rates are given by

$$\begin{aligned}\dot{\epsilon}_{xx} &= u_b ak\, zk^2 e^{-kz} \cos kx \\ &+ u_b (ak)^2\, k(kz - 1/2) e^{-2kz} \sin 2kx + O(\varepsilon^3),\end{aligned} \tag{4.4}$$

$$\begin{aligned}\dot{\epsilon}_{xz} &= \frac{1}{2} u_b k (ak)^2 (1 - z/h) \\ &- u_b ak\, zk^2 e^{-kz} \sin kx \\ &+ u_b (ak)^2\, k(kz - 1/2) e^{-2kz} \cos 2kx + O(\varepsilon^3).\end{aligned} \tag{4.5}$$

4.2 Dimensionless form of the flow solutions

For the following discussion it proves to be of advantage to rescale the various dimensional quantities involved and so to recast the equations in a dimensionless form. To this end dimensionless vertical and horizontal length scales, denoted by capital letters, are defined by

$$X := kx \qquad \text{and} \qquad Z := kz, \tag{4.6}$$

where the wavenumber k is used as a scaling factor. The velocity field is scaled by the sliding velocity

$$V_X(X, Z) := v_x(x, z)/u_b \qquad \text{and} \qquad V_Y(X, Y) := v_y(x, z)/u_b. \tag{4.7}$$

As dimensionless parameters the slope parameter ε and the thinness parameter δ will be used. Sometimes V_X will be denoted by U and V_Y by V. Eqs. (4.1) and (4.2) then become

$$\begin{aligned}V_X(X, Z) &= 1 + \frac{\varepsilon^2}{2\delta}(1 - (1 - \delta Z)^2) \\ &+ \varepsilon Z e^{-Z} \sin X \\ &+ \varepsilon^2 e^{-2Z}(1/4 - Z/2) \cos 2X + O(\varepsilon^3),\end{aligned} \tag{4.8}$$

and

$$\begin{aligned}V_Z(X, Z) &= \varepsilon(1 + Z) e^{-Z} \cos X \\ &+ \frac{1}{2} \varepsilon^2 Z e^{-2Z} \sin 2X + O(\varepsilon^3),\end{aligned} \tag{4.9}$$

where use has been made of Eq. (4.3).

4.3 Discussion of the second order velocity solution with respect to the possibility of extrusion flow

Does Eq. (4.1) imply extrusion flow, *i.e.* does $v_x(x, z)$ have a local maximum or minimum for $z > z_0$? A necessary criterion for a stationary point of $v_x(x, z)$ is $\nabla v_x(x, z) = \mathbf{0}$. One may start with investigating the variation of $V_X(X, Z)$ with respect to X.

4.3.1 Variation of $V_X(X,Z)$ with respect to X

By looking at

$$\begin{aligned}\frac{\partial V_X}{\partial X}(X,Z) &= \varepsilon Z e^{-Z}\cos X \\ &+ \varepsilon^2(1/2-Z)e^{-2Z}\sin 2X,\end{aligned} \tag{4.10}$$

one sees that $\partial V_X(X,Z)/\partial X = 0$ has as a solution $X = \pi/2$ and $X = 3\pi/2$ with no restrictions on Z.[1] There is another interesting set of solutions given by

$$\sin X = \frac{Ze^Z}{\varepsilon(1-2Z)} \tag{4.11}$$

Since $X = 0$ and $X = \pi$ with $Z = 0$ are solutions (these two solution branches will now be called (X_0,Z_0) and(X_π,Z_π)) to Eq. (4.11), there are four points where the horizontal velocity obtains a minimum or a maximum value at $Z = 0$ with respect to X (and not only two as one might have expected). Inspection of the second derivative of $V_X(X,Z)$ with respect to X shows that $X = \pi/2$ and $X = 3\pi/2$ are points of local minima, and that there are local maxima at $X = 0$ and $X = \pi$ for $Z = 0$. The horizontal velocity does therefore not attain its largest value at the highest point of the crest of the sine profile, but at the point of maximum slope. This is a second order effect, as can be seen by looking at Eq. (4.8), and is restricted to regions in the immediate neighbourhood of the bed where the second order term dominates the first order one. There is no first order contribution to the velocity field at the bed. In Fig. 4.1 the value of X according to Eq. (4.11) is depicted as a function of ε and Z. The figure shows that the Z values never get large (Z cannot get larger than $1/2$), and that as Z increases, X approaches the value $X = \pi/2$ rather rapidly. At this point a further increase in Z will increase the right-hand side of (4.11) to greater than unity.[2] Only the solution branch corresponding to $X = 0$ and $Z = 0$ is shown. Only in the immediate vicinity of the bed will the maximum value of $V_X(X,Z)$ be close to the point $X = 0$ and $X = \pi$. As an example: for $\varepsilon = 0.1$, Z will have to be smaller than 0.03 if X is to be less than $0.1/\pi$. This is due to the fact that for $Z = 0$ the first order contribution to $V_X(X,Z)$ vanishes and it is therefore only the second order contribution to $V_X(X,Z)$, which is responsible for the maximum at $Z = 0$. As soon as Z becomes somewhat larger than zero the first order contribution starts to dominate and moves the maximum of the horizontal velocity with respect to X to the point $X = \pi/2$. There will then be two (and no longer four) stationary points: The point $X = \pi/2$, which — as an investigation of the second derivative of $V_X(X,Z)$ with respect to X shows — is a point of maximum, and the point $X = 3\pi/2$, which is a point of minimum. Except for this second order complication, these are the only X values where one can expect stationary points.

[1] It is to be understood that because of the periodicity of the sine function an integer multiple of 2π can always be added to the values of X although it will not be explicitly so written.

[2] As Z increases further the right-hand side of Eq. (4.11) has a local minimum at $Z = 1$, obtaining the value $-e/\varepsilon$, and since the absolute value is larger than 1, there are no solutions for $Z > 1/2$.

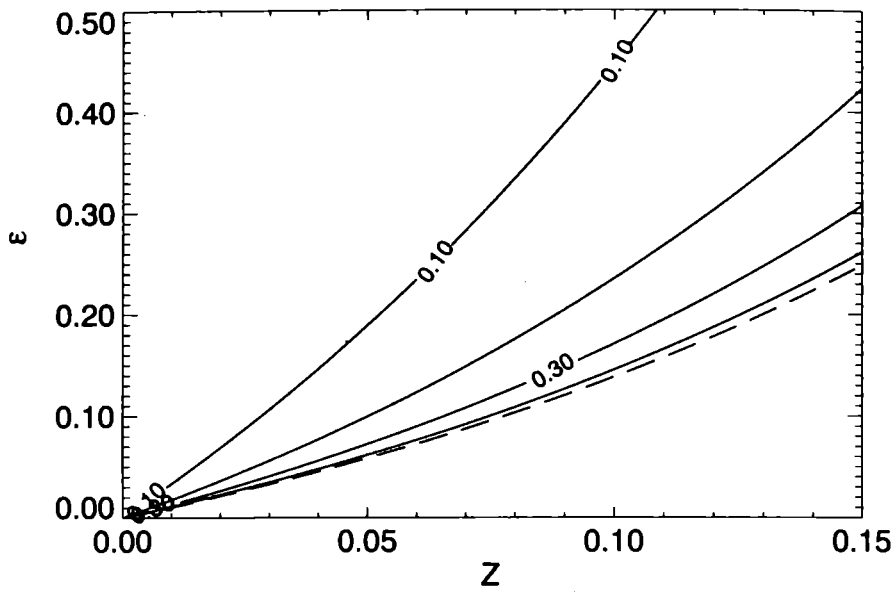

Fig. 4.1: Stationary points at $X = 0$ and $X = \pi$
Lines of constant X/π values according to Eq. (4.11), as a function of ϵ and Z. X, Z and ϵ are related through $X = \arcsin\{\frac{Ze^Z}{\epsilon(1-2Z)}\}/\pi$. Each line corresponds to one particular value of X/π. The dashed line corresponds to $X/\pi = 1/2$. Only above this line is there a solution to Eq. (4.11) for some values of Z and ϵ. There are two solution branches to this equation. The (X_0, Z_0) branch, which includes $(X, Z) = (0, 0)$, is shown. The other branch can be obtained by the mapping $X \mapsto \pi - X$. Notice how rapidly X approaches $\pi/2$ as Z increases, and that, for all reasonable values of ϵ, Z_0 remains close to the bed.

4.3.2 Variation of $V_X(X, Z)$ with respect to Z

Differentiating $V_X(X, Z)$ with respect to Z and setting the resulting expression equal to zero gives

$$1 - \delta Z = \frac{1}{\epsilon}(Z-1)e^{-Z}\sin X + (1-Z)e^{-2Z}\cos 2X. \tag{4.12}$$

The interesting cases to considered are $X = \pi/2$ and $X = 3\pi/2$, but notice that $Z = 0$, $X = 0$ and $X = \pi$ are also solutions to (4.12). These points, which are situated at the bedrock interface, are saddle points. Here the horizontal velocity has a maximum with respect to X but a minimum with respect to Z. This minimum is situated at $Z = 0$, which forms the boundary of the medium. The existence of these points is, as said before, a second order effect.

Let us begin with the case $X = \pi/2$ and see if there is a solution to the resulting equation

$$\underbrace{1 - \delta Z}_{=:L(\pi/2, Z, \delta)} = \underbrace{\frac{1}{\epsilon}(Z-1)e^{-Z} + (Z-1)e^{-2Z}}_{=:R(\pi/2, Z, \epsilon)}. \tag{4.13}$$

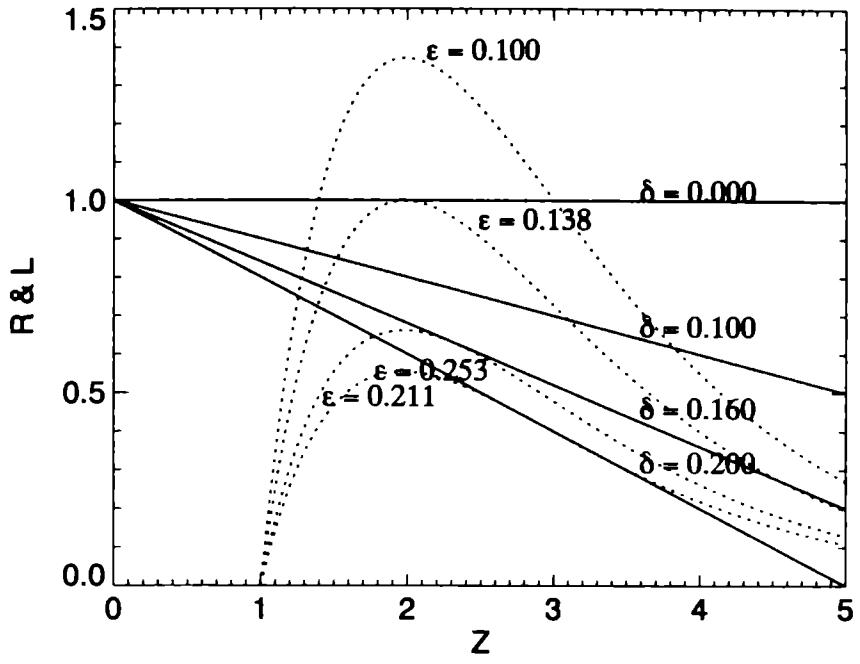

Fig. 4.2: $L(\pi/2, Z, \delta)$ and $R(\pi/2, Z, \varepsilon)$ as functions of Z.
The solid lines represent the left-hand side of Eq. (4.13) for a few different values of δ, and the dotted lines show the right-hand side of that same equation for different ε values. For a given δ value, if ε is small enough there will be at least two solutions. If $\delta > 0$ a third solution close to or above the surface (at the surface $Z = 1/\delta$) will exist. For every δ, ε has to be smaller than some critical value if there is to be at least one solution. There are no solutions for $Z < 1$, and as ε increases the first solution (going along an ε curve from left to right) moves away from the bed, and the second solution towards the bed. The first solution is, as explained in the text, a point of relative maximum of $V_X(X, Z)$ called $U^{\max}_{\pi/2}$, and the second solution is a saddle point called $U^{\text{saddle}}_{\pi/2}$.

This is a non-linear equation that does not have a solution in closed form. By plotting the left-hand side ($L(\pi/2, Z, \delta)$) and the right-hand side ($R(\pi/2, Z, \varepsilon)$) separately, as is done in Fig. 4.2, one sees that there will be a solution to (4.13) if the right-hand side, for at least one value of Z, becomes greater than $1 - \delta Z$. This will happen if ε is less than some particular value, that will now be called $\varepsilon_{\text{critical}}(\pi/2, \delta)$. There will only be stationary points at $X = \pi/2$ for some δ if $\varepsilon < \varepsilon_{\text{critical}}(\pi/2, \delta)$. To determine $\varepsilon_{\text{critical}}(\pi/2, \delta)$, write ε as a function of Z and δ

$$\varepsilon(Z, \delta) = \frac{Z - 1}{(1 - \delta Z)e^{Z} + (1 - Z)e^{-Z}}. \tag{4.14}$$

Then $\varepsilon_{\text{critical}}(\pi/2, \delta)$ can be found by maximising ε given by (4.14) subjected to $Z > 0$ and $0 \leq \delta \ll 1$. Differentiating $\varepsilon(Z, \delta)$ with respect to Z gives

$$\frac{\partial \varepsilon(Z, \delta)}{\partial Z} = \frac{(2 - Z + (Z^2 - Z - 1)\delta)e^{Z} + (-Z^2 + 2Z - 1)e^{-Z}}{((\delta Z - 1)e^{Z} - (Z + 1)e^{-Z})^2}. \tag{4.15}$$

By solving $\partial \varepsilon / \partial Z = 0$ numerically, $\varepsilon_{\text{critical}}(\pi/2, \delta)$ can be calculated as a function

of δ.[3] As an example let's assume $\delta = 0$, which according to Eq. (4.15) gives $(Z-1)^2 e^{-2Z} = 2 - Z$, or — as can be found by doing a few numerical iterations with $Z = 2$ as a starting value — that $Z \approx 1.9816906$, which gives (*c.f.* Eq. (4.14)) $\varepsilon \approx 0.1378839$.[4] Another interesting limiting case to consider is $\delta = 0$ and $\varepsilon \to 0$. Then, as can be seen by looking at Eq. (4.13), Z must obey $(Z-1)e^{-Z} = 0$, which gives $Z = 1$ or $Z = +\infty$. For infinitely thick "glaciers" with ε truly small (let's say $\varepsilon < 0.05$), there will therefore only be one stationary point for $X = \pi/2$, situated at $Z \approx 1$. As ε gets larger this stationary point moves upward towards $Z \approx 1.9816906$ and another stationary point appears close to the surface which moves downwards towards $Z \approx 1.9816906$ and disappears as ε becomes equal to $0.1378839\ldots$. At this value of ε, which will now be called $\varepsilon_{\text{critical}}(\pi/2, \delta)$ ($\varepsilon_{\text{critical}}(\pi/2, 0) \approx 0.1378839$), these stationary points coincide and disappear. Accordingly the point where these two stationary points meet as $\varepsilon \to \varepsilon_{\text{critical}}$ will be called $Z_{\text{critical}}(\pi/2, \delta)$. We have $Z_{\text{critical}}(\pi/2, 0) \approx 1.9816906$. An inspection of the determinant of the Hessian matrix of $V_X(X, Z)$ at the point $X = \pi/2$ shows that the stationary point below $Z_{\text{critical}}(\pi, \delta)$ is a point of relative maximum, so that it will now be called $U^{\max}_{\pi/2}$. The stationary point situated above $Z_{\text{critical}}(\pi/2, \delta)$ is a saddle point; as a function of X, $V_X(X, Z)$ has a maximum there, but a minimum if the variation with respect to Z is considered. This point will be called $U^{\text{saddle}}_{\pi/2}$.

$\varepsilon_{\text{critical}}(\pi/2, \delta)$ is depicted in Fig. 4.3. The figure was obtained by solving

$$\partial \varepsilon(Z, \delta)/\partial Z = 0 \tag{4.16}$$

numerically for different values of δ, $\varepsilon_{\text{critical}}(\pi/2, \delta)$, subject to $\partial^2 \varepsilon/\partial^2 Z < 0$ and $Z > 1$. The figure shows that the value of ε, above which the horizontal velocity has no stationary points at $X = \pi/2$, gets larger as δ increases.

The variation of $\varepsilon_{\text{critical}}(\pi/2, \delta)$ and of δ as a function of $Z_{\text{critical}}(\pi/2, \delta)$ is given in Fig. 4.4. As ε increases from 0 to $\varepsilon_{\text{critical}}(\pi/2, \delta)$, $U^{\max}_{\pi/2}$ goes from $Z = 1$ to $Z = Z_{\text{critical}}(\pi/2, \delta)$. $Z_{\text{critical}}(\pi/2, \delta)$ increases somewhat with $\varepsilon_{\text{critical}}(\pi/2, \delta)$. For every ε less than $\varepsilon_{\text{critical}}(\pi/2, \delta)$ there will be at least two stationary points. (The possibility of a third stationary point will be discussed later.) One of these two stationary points is a saddle point and will be called $U^{\text{saddle}}_{\pi/2}$. $U^{\text{saddle}}_{\pi/2}$ is situated above $Z_{\text{critical}}(\pi/2, \delta)$. The other one is a point of relative maximum and will hence be called $U^{\max}_{\pi/2}$. $U^{\max}_{\pi/2}$ is situated below $Z_{\text{critical}}(\pi/2, \delta)$. As ε increases $U^{\max}_{\pi/2}$ moves upwards toward $Z_{\text{critical}}(\pi/2, \delta)$, $U^{\text{saddle}}_{\pi/2}$ moves downwards toward $Z_{\text{critical}}(\pi/2, \delta)$; they meet there for a value of $\varepsilon = \varepsilon_{\text{critical}}(\pi/2, \delta)$ and disappear. In Fig. 4.5 the position of $U^{\max}_{\pi/2}$ and $U^{\text{saddle}}_{\pi/2}$ as a function of ε for two different δ values is shown. It can be seen how these two points move along Z toward each other as ε increases — $U^{\text{saddle}}_{\pi/2}$ starting from $Z = 1/\delta$ and $U^{\max}_{\pi/2}$ starting from $Z = 1$ — meeting at

[3] There are two solutions to $\partial \varepsilon/\partial Z = 0$, one corresponding to $\partial^2 \varepsilon/\partial^2 Z > 0$ and another which gives $\partial^2 \varepsilon/\partial^2 Z < 0$. If $\delta \ll 1$ then the minimum solution (which exists because of the $(1 - \delta Z)$ term in Eq. (4.14)) will be situated close to $z\delta = 1$. For ε lying between these maximum/minimum values there are three solutions to (4.13).

[4] By looking at Eq. (4.13), setting $\delta = 0$ and ignoring the second term on the right-hand side with respect to the first one (anticipating that ε will be small), one finds easily, by calculating the maximum of the resulting equation with respect to Z, that ε must be larger or equal to $e^{-2} \approx 0.135$ if there is to be a solution; a good approximation of the more correct value of 0.1378839.

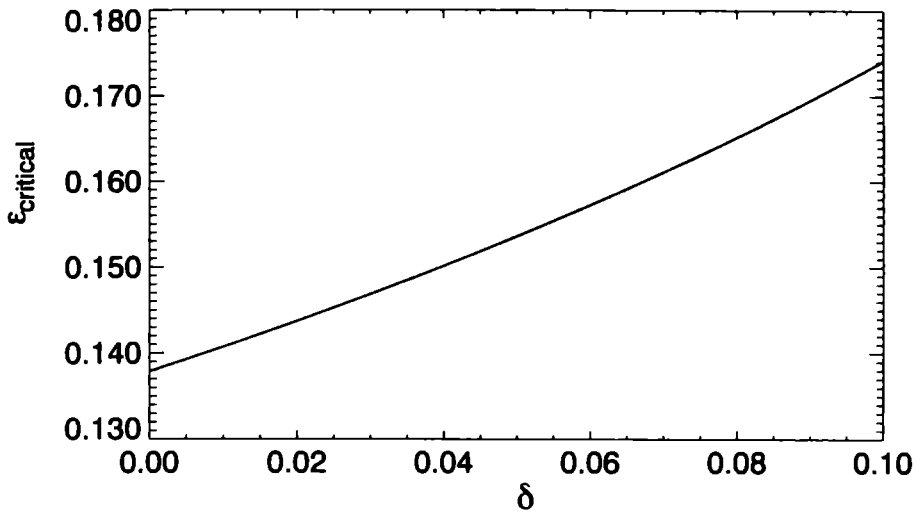

Fig. 4.3: $\varepsilon_{\text{critical}}(\pi/2, \delta)$ as a function of δ.
For ε and δ values below the line there will be at least two solutions to Eq. (4.13). One of these two solutions corresponds to a local maximum of the horizontal velocities above the peak of the sinusoidal bed and is called $U^{\text{max}}_{\pi/2}$. The other solution is situated above $U^{\text{max}}_{\pi/2}$ and corresponds to a saddle point of the horizontal velocities, where v_x has a local maximum with respect to X but a local minimum with respect to Z, and is called $U^{\text{saddle}}_{\pi/2}$. If, for a given δ the roughness of the bed corresponds to a ε lying on the curve, there will only be one solution to Eq. (4.13). This solution corresponds to the situation were the two points $U^{\text{max}}_{\pi/2}$ and $U^{\text{saddle}}_{\pi/2}$ coincide and disappear. For ε larger than $\varepsilon_{\text{critical}}$ for some given δ, which in the figure corresponds to ε and δ values lying above the line, the horizontal velocity will have no local maximum or a saddle point at $x = \pi/2$. Note that $\varepsilon_{\text{critical}}(\pi/2, \delta)$ increases as a function of δ. There is a limiting value of $\varepsilon_{\text{critical}}(\pi/2, 0) \approx 0.1378839$ as $\delta \to 0$.

$Z = Z_{\text{critical}}(\pi/2, \delta)$ and $\varepsilon = \varepsilon_{\text{critical}}(\pi/2, \delta)$. It can also be seen that $\varepsilon_{\text{critical}}(\pi/2, \delta)$ increases as δ becomes larger (this can be seen better in Fig. 4.3).

At some point the curvature of $R(\pi/2, Z, \varepsilon)$ will change sign and the solid lines of Fig. 4.2 can cross the dotted ones not only twice but three times, giving rise to the third stationary point. Calculating $d^2R(\pi/2, Z, \varepsilon)/dz^2$ and setting the resulting expression equal to zero gives the position of the inflexion-point of $R(\pi/2, Z, \varepsilon)$

$$\varepsilon = \frac{Z-3}{4(Z-2)} e^Z, \tag{4.17}$$

so that the inflexion point will be at Z slightly greater than 3. The third stationary point, at which the streamwise velocity will be called $U^{\text{Up}}_{\pi/2}$, must therefore be above $Z = 3$ so that δ has to be less than $1/3$. $U^{\text{Up}}_{\pi/2}$ will be closest to the bed if Eq. (4.13) is fulfilled where the slope of the left-hand and right-hand sides are the same.[5] This

[5]Then, at the point where the dotted lines of Fig. 4.2 touch the solid ones, the slope of the two lines will be the same.

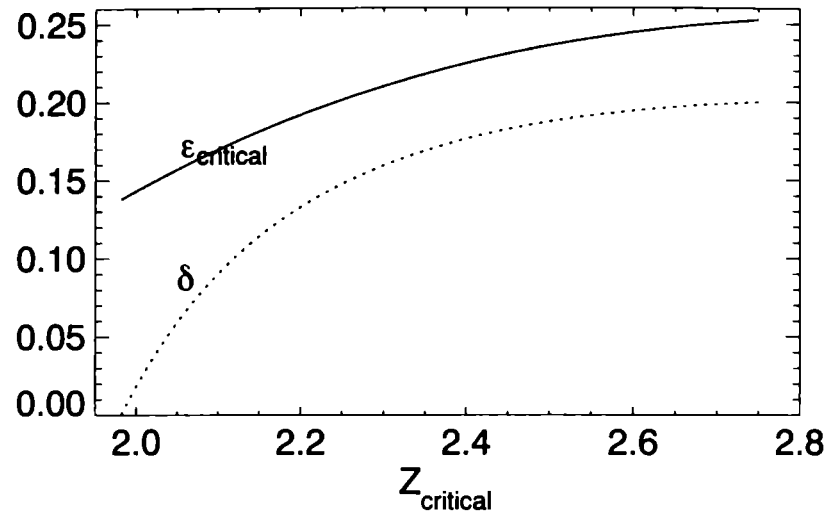

Fig. 4.4: $\varepsilon_{\text{critical}}(\pi/2,\delta)$ and δ as a function of $Z_{\text{critical}}(\pi/2,\delta)$. $Z_{\text{critical}}(\pi/2,\delta)$ is the point where the stationary points $U^{\max}_{\pi/2}$ and $U^{\text{saddle}}_{\pi/2}$ meet and disappear as ε goes to $\varepsilon_{\text{critical}}(\pi/2,\delta)$. For $\varepsilon < \varepsilon_{\text{critical}}(\pi/2,\delta)$ the stationary point $U^{\max}_{\pi/2}$ is situated below $Z_{\text{critical}}(\pi/2,\delta)$ and the stationary point $U^{\text{saddle}}_{\pi/2}$ above $Z_{\text{critical}}(\pi/2,\delta)$. $\varepsilon_{\text{critical}}$ and δ are connected, as is shown in Fig. 4.3.

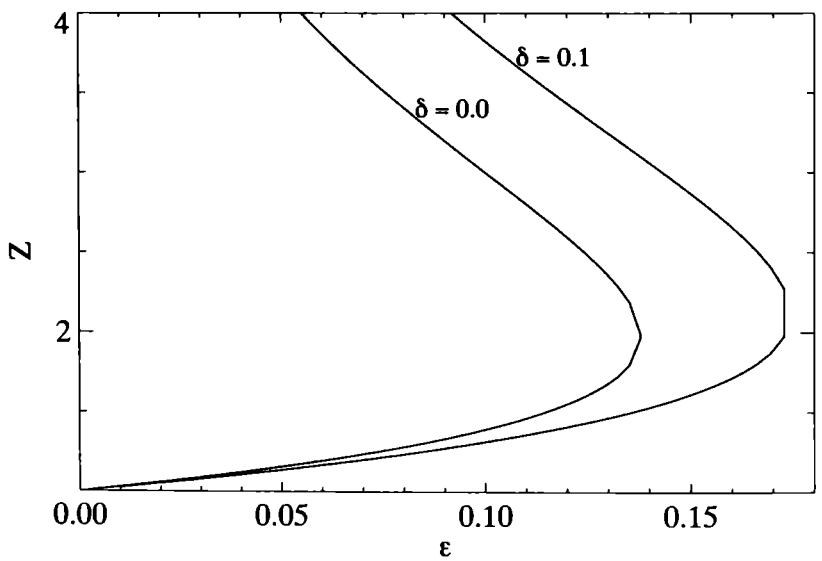

Fig. 4.5: The position of $U^{\max}_{\pi/2}$ and $U^{\text{saddle}}_{\pi/2}$ as a function of ε for $\delta = 0$ and $\delta = 0.1$. $Z_{\text{critical}}(\pi/2,\delta)$ and $\varepsilon_{\text{critical}}(\pi/2,\delta)$ are the points where the the lines are vertical. The branch above $Z_{\text{critical}}(\pi/2,\delta)$ corresponds to $U^{\text{saddle}}_{\pi/2}$ and the one below to $U^{\max}_{\pi/2}$. For $\varepsilon = \varepsilon_{\text{critical}}(\pi/2,\delta)$ there are no $U^{\max}_{\pi/2}$ and $U^{\text{saddle}}_{\pi/2}$ points. These solutions were found by solving Eq. (4.13) numerically.

must happen for $Z > 3$ if there is to be a third stationary point ($U^{\mathrm{Up}}_{\pi/2}$) at all

$$L(\pi/2, Z, \delta) = R(\pi/2, Z, \varepsilon) \qquad \text{and} \qquad \frac{\partial L(\pi/2, Z, \delta)}{dz} = \frac{\partial R(\pi/2, Z, \varepsilon)}{dz}. \tag{4.18}$$

Solving these two equations simultaneously for ε and δ yields

$$\varepsilon = \frac{Z^2 - Z - 1}{2Z^2 - 2Z - 1 - e^{2Z}} e^Z, \tag{4.19}$$

and

$$\delta = \frac{e^{-2Z}(Z^2 - 2Z + 1) - 2 + Z}{Z^2 - Z - 1}, \tag{4.20}$$

subject to $Z > 3$.

In Fig. 4.6 ε and $1 - \delta Z$, where Z in this context stands for the Z coordinate of $U^{\mathrm{Up}}_{\pi/2}$, are plotted as functions of δ, according to Eq. (4.19) and Eq. (4.20). If δ goes to zero, $U^{\mathrm{Up}}_{\pi/2}$ goes to $+\infty$, so that $1 - \delta U^{\mathrm{Up}}_{\pi/2} \to 0$, *i.e.* $U^{\mathrm{Up}}_{\pi/2} \to 1/\delta$, which means that $U^{\mathrm{Up}}_{\pi/2}$ is at the surface. This behavior is expected because as $\delta \to 0$ the glacier becomes infinitely thick and the surface reacts only to the average form of the bed, which means that close to the surface there is no horizontal velocity variation of the vertical velocity component ($\partial V_Z/\partial X = 0$), and because of the free surface condition no shear stress and therefore no shear strain rate, which means that $\partial V_X/\partial Z$ is zero also. The interesting thing about Fig. 4.6 is the fact that this point of no vertical variation of the horizontal velocity, which is normally at the surface, can move, for some value of δ and ε, somewhat below the surface.

As $U^{\mathrm{Up}}_{\pi/2}$ approaches 3 the slope of $1 - \delta U^{\mathrm{Up}}_{\pi/2}$ becomes infinite; if that curve were to be followed further it would have a negative slope. This continuation of the curve does not correspond to $U^{\mathrm{Up}}_{\pi/2}$ but to $U^{\mathrm{saddle}}_{\pi/2}$; $U^{\mathrm{Up}}_{\pi/2}$ does no longer exist. For rather large values of δ, larger than about 0.2 ($\delta \approx 0.20198$ corresponds to $Z = 3$ according to Eq. (4.20)), and ε larger than 0.35, the vertical variation of V_X will therefore not be zero at the surface $Z = 1/\delta$ ($\partial V_Z/\partial X \neq 0$) and one must expect the surface to start to deform because of bed undulations. This theory can hence not be used for $\delta > 0.2$, since the existence of a free surface at $Z = 1/\delta$ was assumed.

The other possible X value for a stationary point of $V_X(X, Z)$, in addition to $X = \pi/2$, is $X = 3\pi/2$. Inserting $X = 3\pi/2$ into Eq. (4.12) gives:

$$1 - \delta Z = e^{-Z}(1 - Z)(1/\varepsilon - e^{-Z}) \tag{4.21}$$

The left side will always be positive, as will the term $1/\varepsilon - e^{-Z}$. For $Z = 1$ the right-hand side is equal to zero, above $Z = 1$ it is negative and no solution is possible, while below $Z = 1$ it is positive and there will always be a solution if $1 \leq 1/\varepsilon - 1$, or if $\varepsilon \leq 1/2$, which means that $\varepsilon_{\mathrm{critical}}(3\pi/2, \delta) = 1/2$. For $\varepsilon \to 0$ this solution will be situated at $Z = 1$ and for $\varepsilon = 1/2$ it will be situated at $Z = 0$ no matter what the value of δ is. Again, by looking at the determinant of the Hessian matrix, one finds that this stationary point is a point of relative minimum, and it will be called $U^{\mathrm{min}}_{3\pi/2}$. Eq. (4.21) can be solved for ε:

$$\varepsilon = \frac{1 - Z}{(1 - \delta Z)e^Z + (1 - Z)e^{-Z}}. \tag{4.22}$$

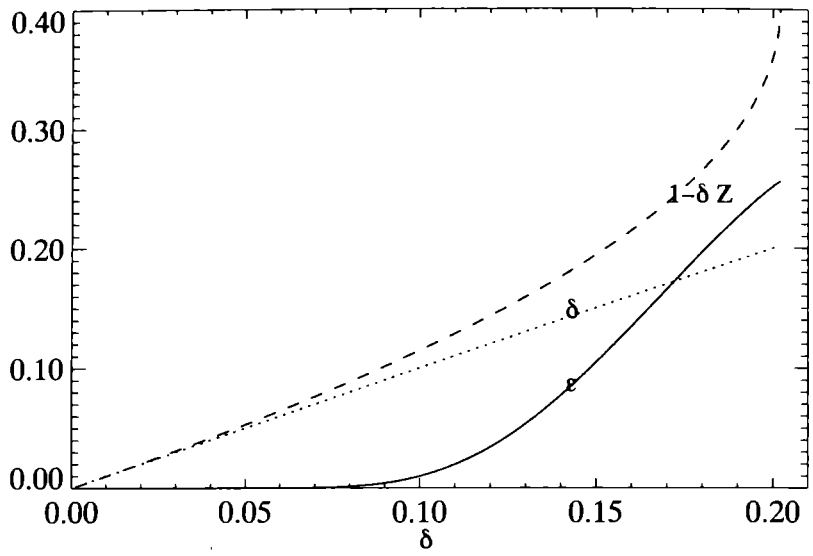

Fig. 4.6: ε and $1-\delta Z$, where Z denotes the normalized vertical position of $U^{\mathrm{Up}}_{\pi/2}$, as a function of δ. $U^{\mathrm{Up}}_{\pi/2}$ is defined as the point of the horizontal velocity above $U^{\mathrm{saddle}}_{\pi/2}$ where its vertical variation is zero. The coordinate system is scaled in such a way that $\delta Z = 1$ corresponds to $U^{\mathrm{Up}}_{\pi/2}$ being situated at the surface of the glacier. Since the vertical variation of the horizontal velocity is always zero at the surface, which follows from the fact that at the surface the shear stresses must be zero, one expects $U^{\mathrm{Up}}_{\pi/2}$ to be found at the surface, and $1-\delta Z$ to be zero. If $1-\delta Z \not\approx 0$, $U^{\mathrm{max}}_{\pi/2}$ is no longer situated close to the surface, and one must expect the surface to start to deform because of the bed undulations. Morland's solutions can then no longer be used. Note that the vertical position of $U^{\mathrm{Up}}_{\pi/2}$, for a given δ, also depends on ε. The curve for $1-\delta Z$ corresponds to the "worst case", in the sense that they were calculated for the value of ε that causes, for a given δ, $U^{\mathrm{Up}}_{\pi/2}$ to be situated as far below the glacier surface as possible. This value of ε can also be seen and is represented by the ε curve.

As δ varies the position of $U^{\mathrm{min}}_{3\pi/2}$ changes somewhat. This is depicted in Fig. 4.7, which shows the position of $U^{\mathrm{min}}_{3\pi/2}$ as a function of ε for two different δ values.[6] A value of $\varepsilon_{\mathrm{critical}}(3\pi/2,\delta) = 1/2$ is rather large, and it is not clear if this prediction can be trusted since the perturbation approach is only valid for $\varepsilon \ll 1$.

The existence of the stationary points $U^{\mathrm{max}}_{\pi/2}$, $U^{\mathrm{saddle}}_{\pi/2}$ and $U^{\mathrm{min}}_{3\pi/2}$ shows that there will be two regions of extrusion flow. One is at $X = \pi/2$, which extends over the region that lies between the saddle point ($U^{\mathrm{saddle}}_{\pi/2}$) and the maximum point ($U^{\mathrm{max}}_{\pi/2}$), and another one at $X = 3\pi/2$ that extends from bed towards the point of local velocity minimum ($U^{\mathrm{min}}_{3\pi/2}$). The extrusion flow at $X = \pi/2$ will only be found for $\varepsilon < \varepsilon_{\mathrm{critical}}(\pi/2,\delta)$, and the extrusion flow at $X = 3\pi/2$ will only be found for $\varepsilon < 1/2$.

To get an idea of how strong the velocity maximum at $X = \pi/2$, is with respect to

[6] For a given ε value and $\delta \neq 0$ there will be two solutions for Z of Eq. (4.22). Only one of them will be situated below $1/\delta$ (which is the maximum value of Z) and it is depicted in Fig. 4.7. The other one will always be somewhat above $1/\delta$ and is therefore of no relevance.

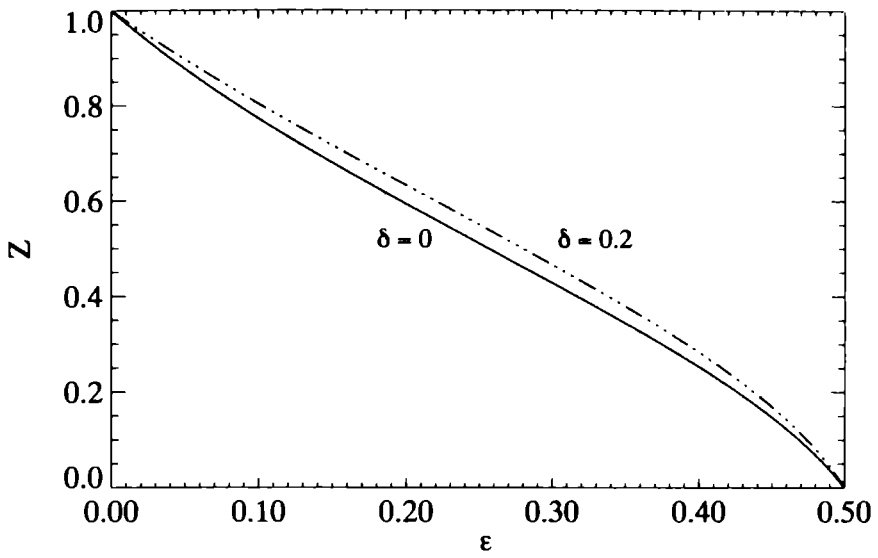

Fig. 4.7: The position of $U^{\min}_{3\pi/2}$ as a function of ε for $\delta = 0$ and $\delta = 0.2$. $U^{\min}_{3\pi/2}$ is the local minimum of the horizontal velocities above the trough of the sinusoidal curve (where $x = 3\pi/2$). For $\varepsilon = 0$, $U^{\min}_{3\pi/2}$ is situated at $Z = 1$. As ε increases it approaches the bed, and disappears at $\varepsilon = 1/2$. Note that δ has almost no effect on the position of $U^{\min}_{3\pi/2}$.

the velocity at $(X, Z) = (\pi/2, 0)$, $R^{\max}(\varepsilon, \delta)$ is defined as

$$R^{\max}(\varepsilon, \delta) := \frac{U^{\max}_{\pi/2} - U(\pi/2, 0)}{U(\pi/2, 0)}. \tag{4.23}$$

For $\delta = 0$ and $\varepsilon \to 0$

$$R^{\max}(\varepsilon, 0) = \varepsilon \frac{\varepsilon + 1/e + \varepsilon(1/e^2 + 1)/4}{1 - \varepsilon^2/4} \tag{4.24}$$

or $R^{\max}(\varepsilon, 0) \approx \varepsilon/e$ ($\delta = 0$, $\varepsilon \to 0$). This equation cannot be used for ε values close to $\varepsilon_{\text{critical}}(\pi/2, 0)$ because the variation of the position of $U^{\max}_{\pi/2}$ with respect to ε has been ignored.

In a similar way $R^{\min}(\varepsilon, \delta)$ is defined as

$$R^{\min}(\varepsilon, \delta) := \frac{U^{\min}_{3\pi/2} - U(3\pi/2, 0)}{U(3\pi/2, 0)}. \tag{4.25}$$

$R^{\min}(\varepsilon, \delta)$ gives an idea of how strong the velocity decrease at $X = 3\pi/2$ is, with respect to the velocity at the bed.

Eq. (4.8) gives:

$$R^{\min}(\varepsilon, \delta) = \varepsilon \frac{-1/e + \varepsilon + (1/e^2 + 1)/4}{1 - \varepsilon^2/4}. \tag{4.26}$$

There is a minimum at:

$$\varepsilon = (5e^2 + 1 - \sqrt{25e^4 + 6e^2 + 1})/e \tag{4.27}$$

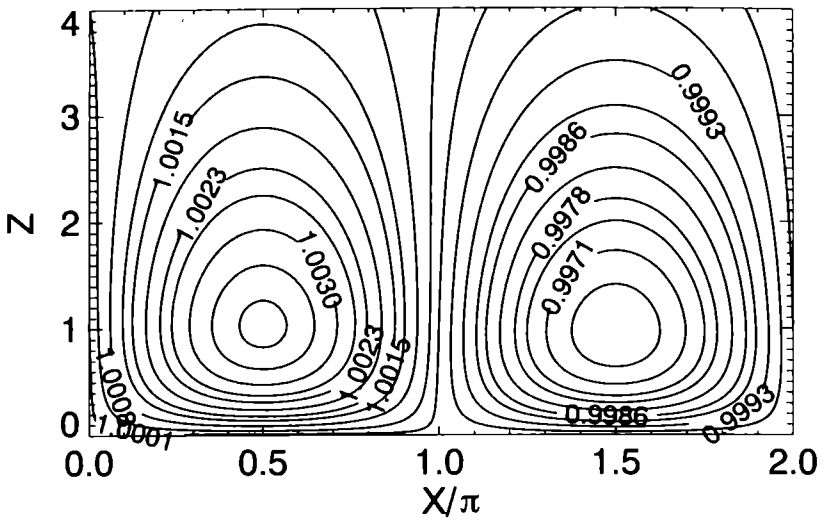

Fig. 4.8: V_X as a function of X and Z for $\varepsilon = 0.01$ and $\delta = 0$. The maximum at $X/\pi = 1/2$ and $Z \approx 1$ is $U^{\max}_{\pi/2}$. The minimum at $X/\pi = 3/2$ and $Z \approx 1$ is $U^{\min}_{3\pi/2}$. For $\varepsilon \to 0$ the position of $U^{\max}_{\pi/2}$ and $U^{\min}_{3\pi/2}$ approaches $Z = 1$. With increasing ε, $U^{\max}_{\pi/2}$ moves upwards and disappears for $\varepsilon = \varepsilon_{\text{critical}}$. $U^{\min}_{3\pi/2}$, on the other hand, moves downwards with increasing ε and disappears for $\varepsilon = 1/2$.

or $\varepsilon \approx 0.144$. For this value the extrusion flow is the largest. This value is, however, only approximately correct since here again the variation of $U^{\min}_{3\pi/2}$ with respect to ε has been ignored, and its position at $Z = 1$ for $\varepsilon = 0$ was used.

It is illustrative to look at the velocity field given by (4.8) for some values of ε and δ. In Fig. 4.8 $V_X(X, Z)$ is shown for $\varepsilon = 0.01$ and $\delta = 0$. $U^{\max}_{\pi/2}$ at $X = \pi/2$ and $U^{\min}_{3\pi/2}$ at $X = 3\pi/2$ can be seen but not, of course, $U^{\text{saddle}}_{\pi/2}$ since it is at $Z = +\infty$ for $\delta = 0$. Notice that the X is in units of π.

The solution of Nye and of Kamb has, as said earlier, regions of extrusion flow. For the stationary points this solution gives, for the vertical position of the maximum and the minimum points, the value $Z = 1$. The solution of Nye and of Kamb has no saddle point. These findings are reproduced by Morland's solution in the limit $\varepsilon \to 0$ as is to be expected. For ε values as large as $\varepsilon_{\text{critical}}(\pi/2, 0)$ there are profound differences. Nye's and Kamb's solution makes no distinction between the maximum and minimum points regarding their appearance/disappearance with respect to different slope parameters values. Morland's solution predicts instead the disappearance of the maximum point, $U^{\max}_{\pi/2}$, and the saddle point, $U^{\text{saddle}}_{\pi/2}$, at $\varepsilon > \varepsilon_{\text{critical}}(\pi/2, \delta)$. The minimum point, $U^{\min}_{3\pi/2}$, remains for ε values up to $\varepsilon = 1/2$. One sees that Morland's solution contains regions of extrusion flow, but only for a limited range of ε and δ values.

It is important to notice that the influence of the wavy nature of the bed on the flow is not largest at the bed but at some distance above it. Typically this distance will be about 1 (or $z = 1/k$). Often the deformation of a bore hole is used to get information on the rheological behavior of the ice. One must carefully interpret the

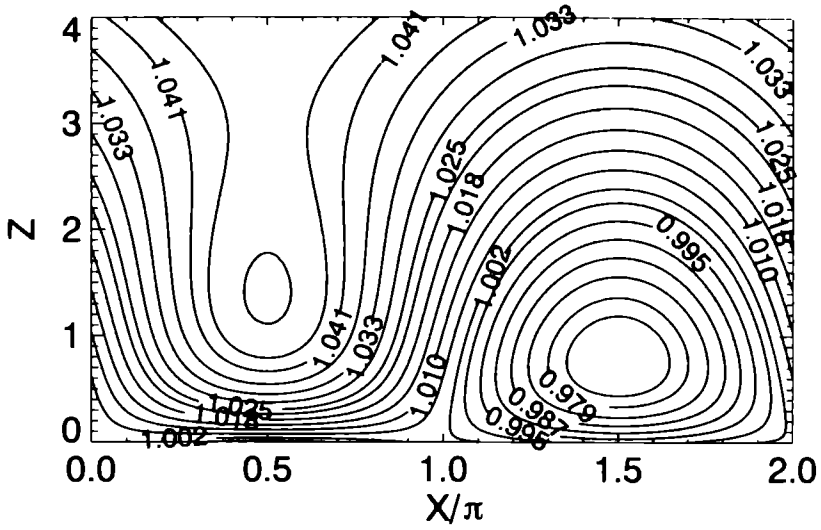

Fig. 4.9: V_X as a function of X and Z for $\varepsilon = 0.1$ and $\delta = 0$.
$U^{\max}_{\pi/2}$ has moved upwards and $U^{\min}_{3\pi/2}$ downwards with respect to Fig. 4.8. The point $U^{\text{saddle}}_{\pi/2}$ can also be seen. As ε increases further $U^{\max}_{\pi/2}$ and $U^{\text{saddle}}_{\pi/2}$ move towards $Z = Z_{\text{critical}}(\pi/2, \delta) \approx 1.9816906$, which they reach for $\varepsilon = \varepsilon_{\text{critical}}(\pi/2, 0) \approx 0.1378839$. Simultaneously $U^{\min}_{3\pi/2}$ moves downwards and reaches $Z = 0$ for $\varepsilon = \varepsilon_{\text{critical}}(3\pi/2, \delta) = 1/2$.

data from the lowest portion of a bore hole since the exact form of the bedrock, which is usually not known, can have a large effect on the flow. Fig. 4.9, for example, shows that the perturbed flow (the second and the third terms of Eq. (4.8)) dominates in the region $Z < 3$, the gravity-driven plane flow (the first term of Eq. (4.8)).

In a numerical study Meyssonnier (1983) observed the appearance and the disappearance of $U^{\max}_{\pi/2}$ and $U^{\text{saddle}}_{\pi/2}$ but did not mention $U^{\min}_{3\pi/2}$. He did not include gravity in his model. The driving force of the motion was a given horizontal velocity at some distance above the bed. In this respect his calculations correspond to the problem solved by Nye and Kamb. The maximum point disappears because of the super position of a linear velocity profile on the Nye and Kamb solution.

4.4 A physical explanation for extrusion flow

Upon reflection it becomes evident that the vertical contraction and expansion of the ice close to the bed is responsible for the extrusion flow. At some distance, let us say at $z = z_1$, sufficiently far above the bed the ice moves parallel to the mean bed slope. For $kx = \pi/2$, a high-pressure zone develops above the bed, which causes a Poiseuille flow, superimposed on the gravity-driven plane flow (GDPF) solution. The maximum of the Poiseuille velocity profile is at $(z_1 - z_0)/2$, and if its decrease above that point is faster than the increase of the GDPF velocity profile, a velocity maximum will be found. Since the influence of the bed profile on velocity field is (because of the factor e^{-kz}) limited to a zone of height proportional to $1/k$, z_1 will

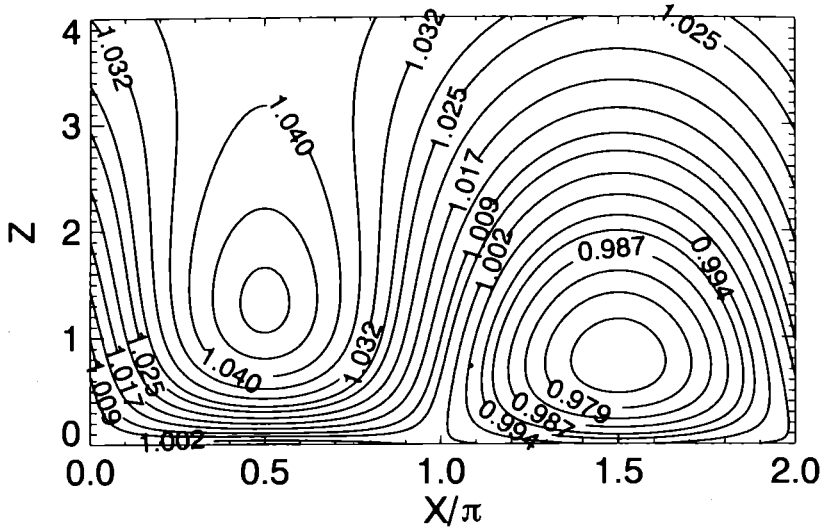

Fig. 4.10: V_X as a function of X and Z for $\varepsilon = 0.1$ and $\delta = 0.1$.
By comparing this figure with Fig. 4.9 the influence of δ can be seen.

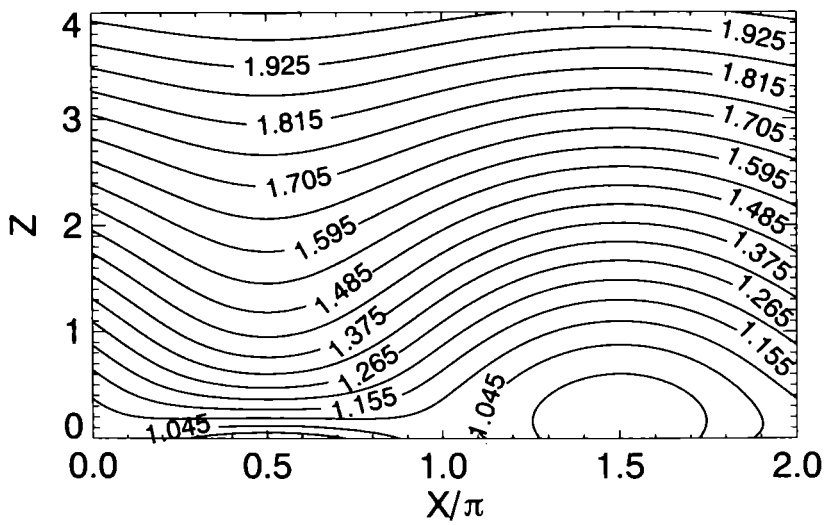

Fig. 4.11: V_X as a function of X and Z for $\varepsilon = 0.5$ and $\delta = 0$. The points $U^{\max}_{\pi/2}$ and $U^{\text{saddle}}_{\pi/2}$ can no longer be seen, and point $U^{\min}_{3\pi/2}$ is at $Z = 0$, so there is no extrusion flow.

be proportional to $1/k$ and one will expect the position of this maximum to also be proportional to $1/k$. As a a matter of fact (2.23) has a maximum at $z = 1/k$ for $kx = \pi/2$. At $kx = 3\pi/2$ the ice is expanded vertically and the Poiseuille flow profile reverses, causing a velocity minimum, again at $z = 1/k$ as said before.

Nye's and Kamb's solution ignores GDPF and actually expresses nothing but this contraction and expansion due to the wavy nature of the bed. The velocity minimum and maximum therefore never disappears no matter how ε is varied. If on the other

hand the GDPF is present it induces a subtle interplay between the Poiseuille flow and the GDPF. GDPF must be involved if extrusion flow is to develop. Therefore only certain ε values give rise to this interesting flow behavior, as was shown in Sec. 4.3.

4.5 Higher harmonics

Another interesting feature of Eqs. (4.1) and (4.2) is the doubling of the sine-wave frequency. These second harmonics may be somewhat surprising since one might expect the reaction of a linear medium to be of the same frequency as the applied perturbation, a fact well known from linear system theory. The perturbation is, however, in this case not a small term added to the fundamental differential equation, as in the usual perturbation theory, but rather the boundary condition that is perturbed and that is a non-linear perturbation.

A simple argument shows that one is to expect other frequencies than $\sin kx$ to appear in the solution, unless ε is so small that the first order solutions (*cf.* Sec. 2.3.1) are valid, and that they will become more pronounced as ε becomes larger.

Let us suppose that there were no higher harmonics in the expressions for u and w, for all values of ε. That is

$$u = u_b + \hat{c}_0 \sin kx \quad \text{and} \quad w = \hat{c}_1 \cos kx, \quad \text{on} \quad z = z_0, \tag{4.28}$$

where $\hat{c}_0$ and $\hat{c}_1$ are some unknown constants. It follows that

$$\frac{u}{w} = \frac{u_b}{\hat{c}_1 \cos kx} + \frac{\hat{c}_0}{\hat{c}_1} \tan kx. \tag{4.29}$$

Using the exact boundary condition (2.15) and $z_0 = a \sin kx$ one obtains

$$\frac{u}{w} = \frac{1}{ak \cos kx} \tag{4.30}$$

at the base. Comparing Eq. (4.29) and Eq. (4.30) shows that $\hat{c}_1$ must be equal to $u_b ak$ and that $\hat{c}_0$ has to be zero if expression (4.28) is to be true. But this must be true for all ε values because Eq. (4.30) is always valid. On physical grounds $\hat{c}_0 = 0$ can, however, be rejected; for high ε values v_x will certainly not be a constant on $z = z_0$, which means that the starting-point Eq. (4.28), must be incorrect. The velocity will therefore not be a single harmonic.[7]

4.6 The stress field

Using results from Morland (1976a) the stress field can be calculated. My result is

$$\sigma_{xz} = \tau_b(1 - z/h) + 2\eta k^2 u_b a \left\{ ka(kz - 1/2)e^{-2kz} \cos 2kx - kze^{-kz} \sin kx \right\} + O(\varepsilon^3), \tag{4.31}$$

[7]For small corrugation values $\hat{c}_0 = 0$ and $\hat{c}_1 = u_b ak$ may become approximately correct. As a matter of fact this is what Equations (2.23) and (2.24), that only show the dependence on the fundamental harmonic, imply for $z = 0$. The expressions (4.1) and (4.2) that show the existence of the second harmonic do not, of course, conform with these values of $\hat{c}_0$ and $\hat{c}_1$.

$$\sigma_{zz} - \sigma_{xx} = -4\eta u_b k^2 a \left\{ kze^{kz} \cos kx + ka(kz - 1/2)e^{-2kz} \sin 2kx \right\} + O(\varepsilon^3), \quad (4.32)$$

The expression for the second invariant of the deviatoric stress tensor is particularly interesting:

$$\begin{aligned} \tau^2 &= \tau_b^2 (1 - z/h)^2 \\ &- 4\tau_b^2 \frac{z}{a}(1 - z/h)e^{-kz} \sin kx \\ &+ 4\tau_b^2 \{(\frac{z}{a})^2 e^{-2kz} + (1 - z/h)(kz - 1/2)e^{-2kz} \cos 2kx\} \\ &+ 8\tau_b^2 \frac{z}{a} e^{-3kz}(kz - 1/2) \sin kx \\ &+ 4\tau_b^2 e^{-4kz}(kz - 1/2)^2 + O(\varepsilon^6). \end{aligned} \quad (4.33)$$

This equation should be compared with the corresponding Eq. (2.28) of Nye and Kamb. In contrast to (2.28) it shows that τ is dependent on x. It can readily be shown that if $z/h \ll 1$, Eq. (4.33) has stationary points at $(kx, kz) = (pi/2, 1)$, which is a saddle point, and $(kx, kz) = (3\pi/2, 1)$, which is a point of absolute maximum. These stationary points do not disappear at certain corrugation values as did $U_{\pi/2}^{\max}$, $U_{\pi/2}^{\text{saddle}}$ and $U_{3\pi/2}^{\min}$. Notice that τ, for all values of x, increases from the bed upwards, attaining its largest value at $kz = 1$. To get an idea of how large the variation of τ with respect to x is, consider the ratio:

$$R := \frac{\tau(kx = \pi/2, kz = 1)}{\tau(kx = 3\pi/2, kz = 1)} \quad (4.34)$$

which is the ratio of the maximum and minimum values of τ as a function of x. Putting (4.33) into (4.34), and ignoring z/h with respect to other terms, gives

$$R = \sqrt{\frac{1 - 2/e^2 - 1/e^4 + 4(1 - 1/e^2)/(\varepsilon e)}{4(1 - 1/e^2)/(\varepsilon e)1 + 2/e^2 - 1/e^4}} \quad (4.35)$$

or

$$R \approx \sqrt{\frac{0.711\,\varepsilon + 1.272}{0.748\,\varepsilon - 1.272}}. \quad (4.36)$$

For $\varepsilon = 0$ there is of course no variation of τ with x, *i.e.* $R = 1$. A corrugation value of $\varepsilon = 0.1$ gives $R \approx 1.12$ or 12%, and $\varepsilon = 0.3$ gives a variation of about about 42% in τ as a function of x, for $kz = 1$. This shows, without any doubt, that Kamb's main assumption in his development of a non-linear theory of sliding, ϵ_{II} being independent of x, is only approximately valid.

Kamb never claimed that ϵ_{II} was entirely independent of x but merely that the flow is dominated by the z dependence of η. For small enough ε values this will be true. The asymptotic ε dependence of u_b for $\varepsilon \to 0$ is given correctly by Kamb's theory, although the numerical values are not exact, as has been shown on page 32.

All of the above equations for the velocity, the stress field, *etc.* are only valid as long as no bed separation takes place, that is as long as the pressure at the bed remains positive. The pressure field is given by

$$p(x, z) = p_a + \rho_I g h \cos\alpha \left\{ 1 - z/h + \frac{\tan\alpha}{ka}(2e^{-kz} \cos kx + kae^{-2kz} \sin 2kx) \right\} + O(\varepsilon^3) \quad (4.37)$$

where α is the mean bed slope and p_a the atmospheric pressure.

The position of the points of maximum and minimum pressure along the bed are found by solving $\partial p(x,z)/\partial z = 0$ with $z = 0$, which gives

$$\varepsilon = \frac{\sin kx}{\cos 2kx}. \tag{4.38}$$

Using a Taylor expansion, one finds that the pressure obtains its minimum value at $kx = \pi - \varepsilon + O(\varepsilon^3)$ and its maximum value at $kx = \varepsilon + O(\varepsilon^3)$. This shows that as ε gets larger these points move from the inflexion points of the sine curve towards $kx = \pi/2$.

Requiring $p \geq 0$ gives

$$\tan\alpha \leq \frac{\varepsilon}{2}\left\{1 + \frac{p_a}{\rho_I g \cos\alpha}\right\} + O(\varepsilon^3), \tag{4.39}$$

or to a good approximation: $\tan\alpha \leq \varepsilon/2$, if the atmospheric pressure can be ignored with respect to the mean ice overburden pressure. By inverting (4.39) one gets

$$\varepsilon \underset{p_a \ll \rho_I g \cos\alpha}{\geq} \frac{1}{4\tan\alpha}\left\{1 + \frac{p_a}{\rho_I g\cos\alpha} - \sqrt{\left(1 + \frac{p_a}{\rho_I g\cos\alpha}\right)^2 - (4\tan\alpha)^2}\right\} \\ 2\tan\alpha + O((4\tan\alpha)^3), \tag{4.40}$$

which gives a lower limit for ε, for a given mean bed slope and ice thickness.[8] There are therefore two restrictions on ε. First of all, it has to be small if the results of the perturbation analysis are to be applicable, and secondly, it may not be so small that a bed separation occurs. The predictions of this theory can only be trusted for values of ε up to $\varepsilon = 0.5$, which means that α has to be less than 14°. Applications to ice falls are therefore questionable.

4.7 Summary

At this point I would like to summarise the most important results obtained so far.

The sliding law has been given in a non-dimensional form and it has been argued that only ε, δ and n will enter it in a nontrivial way. The fact that u_b increases linearly with λ and a, for a given ε independent of n and δ, as shown in Eq. (3.6), follows directly from dimensional arguments.

For asymptotically small ε and δ values, the sliding law is given by (3.23). A simple argument was given, which does not prove this result, but makes it physically reasonable. There are other theoretical arguments that give the same result (Kamb, 1970; Fowler, 1979).

[8] The solution with a plus sign before the square root in (4.40) can be rejected by noticing that it does not give the correct value in the limit of $\alpha \to 0$.

Using the results of Morland (1976a), the expressions (4.1), (4.2), (4.32), (4.31) and (4.33) that give the stress and velocity fields as functions of x and z have been derived. It turns out that of two of the particularly interesting features of Nye's and Kamb's solution — occurrence of extrusion flow and the second invariant of the strain rates being independent of x — the first is carried on to these more precise solutions but the second is not. It must be stressed that this extrusion flow is of local character, and should possibly be called *local* extrusion flow in order to distinguish it from extrusion flow encountered earlier in the glaciological literature, which was of global nature — extending, at some distance below the surface, through an entire glacier — and causing an increase of ice flux. The local extrusion flow does not add to the ice flux.

Criteria for extrusion flow have been given. Close to the bed the horizontal velocity field can have at most three different stationary points. If $0 < \varepsilon < 1/2$ there is a minimum point ($U^{\min}_{3\pi/2}$) situated at $X = 3\pi/2$ and $Z < 1$, which moves downwards as ε gets larger, reaching the bed for $\varepsilon = 1/2$. For $X = \pi/2$ there is a point of maximum velocity ($U^{\max}_{\pi/2}$) at $1 < Z < Z_{\text{critical}}(\pi/2, \delta)$ and a saddle point ($U^{\text{saddle}}_{\pi/2}$) at $Z > Z_{\text{critical}}(\pi/2, \delta)$ as long as $\varepsilon < \varepsilon_{\text{critical}}(\pi/2, \delta)$. With ε increasing the maximum point, $U^{\max}_{\pi/2}$, moves upwards and the saddle point, $U^{\text{saddle}}_{\pi/2}$, downwards until they meet at $Z = Z_{\text{critical}}(\pi/2, \delta)$ for $\varepsilon = \varepsilon_{\text{critical}}(\pi/2, \delta)$ and vanish.

A simple argument was given, which shows that the velocity will in general not be a simple harmonic at $z = z_0$, except for truly small values of ε; a feature that may at first be somewhat surprising but is evident in expressions (4.1) and (4.2). At large corrugation values this frequency doubling may be expected to become more pronounced.

CHAPTER 5

Testing of the Correctness of Numerical Results Obtained with the FE Program MARC

The general purpose FE Program MARC (MARC, 1992) was used for all numerical calculations of flow velocities and stresses presented in this work, including calculation of flow over a sinusoidal bed. In this chapter various tests done to estimate the errors involved with the numerical calculations are described, and error estimates given.

The results obtained by the FE code were tested by comparing them with analytical solutions for some analytically solvable problems. For the numerical calculation of flow over a sinusoidal bed an additional type of testing was done by comparing results of runs with different values of λ, a, h and α but same ε and δ values together. This latter type of testing gives an estimate of the relative errors that are caused by differences in grid density. Comparison with analytical results, on the other hand, gives an estimate of the absolute errors involved. It is important that both types of testing are done, since the problems that can be solved analytically often possess some kinds of symmetries that are not representative of real glaciers; comparing numerical results with them does therefore not necessarily test the programs in a general way. The discretization error was also estimated by solving the same problem using several meshes with different numbers of elements.

5.1 Comparison with analytical solutions

When comparing calculated results with analytical ones, one should not use a property of the analytical solutions as a boundary condition (BC) for the model. For example, calculating the flow of a gravity-driven plane-flow using the analytical solution for the velocity profile or the stress variation along the edge as a boundary condition for the model will give estimates of the numerical errors which are too low. A better approach would be to use periodic boundary conditions. Results obtained with MARC were compared with analytical solutions for five different problems.

5.1.1 Gravity driven plane flow down an inclined plane

The effect of using velocity or pressure as a boundary condition, and the use of periodic boundary conditions on the accuracy and computer time required, were in-

vestigated. With 8 linear elements in the vertical direction the maximal discrepancy between numerically and analytically calculated velocity for $n = 3$ was 0.04% if the velocity was given as a BC, 0.06% if the pressure was given as BC, and 0.1% for periodic boundary conditions. For non-linear rheological behavior the effective viscosity distribution was repetitively calculated until the maximum change in velocity was less than 0.01%. The iteration procedure converges much faster if the velocity is given as a BC, thus confining the velocity variation, than if the pressure or periodic boundary conditions are used.

5.1.2 Closure rate of a circular hole and the flow between two rotating coaxial cylinders (Couette Flow)

The results concerning the numerical accuracy of the calculation of the closure rate of a circular hole, are similar to those obtained by studying gravity-driven plane flow down an inclined plane. It turned out that for a given mesh the numerical results for flow between two rotating coaxial cylinders were more exact (about an order of magnitude) than those for the closure rate of a circular hole with some pressure p_1 within the hole and some pressure p_2 at the outer boundary. This shows that the accuracy of the numerical results obtained with the same mesh can vary greatly for two seemingly similar problems.

5.1.3 Gravity driven flow down a channel of circular cross-section

The velocity profile for a semi-circular channel of radius R of uniform cross-section and uniform slope α is

$$u(r) = \frac{2A}{n+1}\left(\frac{\tau_b}{2}\right)^n R\left(1-\left(\frac{r}{R}\right)^{n+1}\right), \tag{5.1}$$

where $\tau_b = \rho_I g R \sin\alpha$, and $r = \sqrt{y^2+z^2}$ (Nye, 1965; Hutter, 1983). The discharge q is

$$\begin{aligned} q &= \int_{\pi/2}^{\pi/2} d\theta \int_0^R dr\, v(r,\theta) \\ &= \frac{\pi A}{(n+3)}\left(\frac{\tau_b}{2}\right)^n R^3. \end{aligned} \tag{5.2}$$

If the velocity is scaled with $2AR\tau_b^n$ and the discharge with $2A\tau_b^n R^3$ the dimensionless velocity U_0 and discharge Q are given by

$$U_0 = \frac{1}{2^n(n+1)} \qquad \text{and} \qquad Q = \frac{\pi}{2^{n+1}(n+3)} \tag{5.3}$$

These scalings are the same as those used by Nye (1965).[1]

[1]The A that Nye uses is twice the A used here, *i.e.* $A_{\text{Nye 1965}} = 2A$.

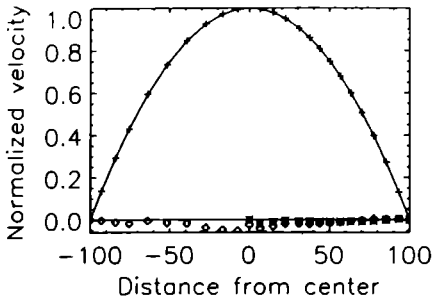

Fig. 5.1-a: Normalized velocity profiles along the z-axis and the y-axis for $n = 1$. Detailed information is given in the text.

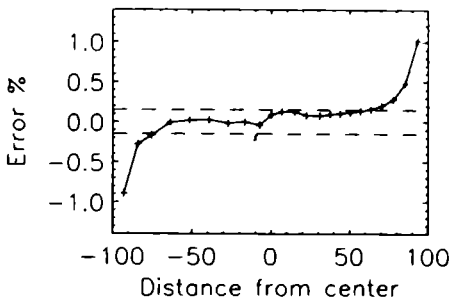

Fig. 5.1-b: Percentage difference between analytical and calculated v_x values for $n = 1$. The long dashes represent the $\pm 0.15\%$ range within which most of the values lie within.

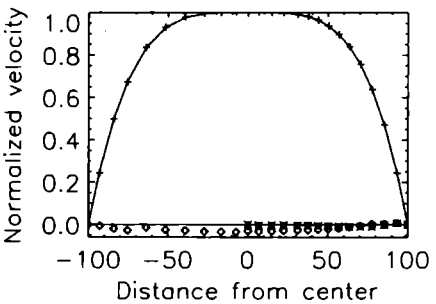

Fig. 5.1-c: Normalized velocity profiles along the z-axis and the y-axis for $n = 3$.

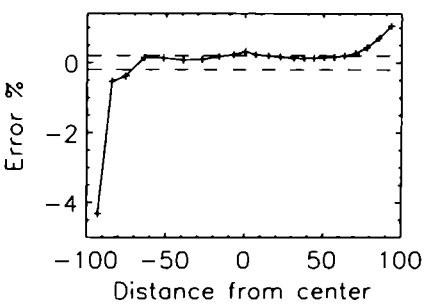

Fig. 5.1-d: Percentage difference between analytical and calculated v_x values for $n = 3$. The long dashes represent the $\pm 0.20\%$ range.

Figs. a and c show the velocity variation of all the three spatial velocity components along a profile that runs from a point at the bottom of the center of the channel ($y = 0$ and $z = -R$) upwards along the z-axis towards the centerline ($y = 0$ and $z = 0$), and then sidewards across the surface along the y-axis toward the margin ($y = R$ and $z = 0$). Calculated values are represented by symbols. v_x is shown as a plus sign, v_y as an asterisk, and v_z as a diamond. The solid line that goes through the plus signs in Figs. a and c is the analytical result for v_x. The perceptual difference between analytically and numerically calculated v_x values is given in Figs. b and d. All the figures refer to the 10×10 discretization. Since the transversal velocity component v_y was fixed ($= 0$) along the longitudinal central plane of the channel, v_y is not shown in the left parts of Figs. a and c.

For the calculations two FE discretizations where used, one with 10×10 elements in the cross-section[2], and another finer discretization with 20×20 elements in the cross-section. The meshes were generated by an automatic 2D mesh generator. An example of the meshes created in this way can be seen in Fig. 5.2. The domain of investigation was three-dimensional, but was reduced to two dimensions by imposing

[2] 10 elements subdivision in each spatial dimension, giving a total of 100 elements.

	U_0	Q
theoretical value	0.03125	0.032725
10×10 mesh	0.03138 (0.42%)	0.03321 (1.5%)
20×20 mesh	0.03126 (0.03%)	0.032703 (0.06%)

Table 5.1: Semi-circular channel. Comparison of analytical and numerical values for U_0 and Q for a semi-circular channel with $n = 3$. Values in the brackets stand for the percentage error in U_0 and Q.

periodic boundary conditions for the velocities. No assumptions about the stresses or the velocities at the "cut off" boundaries were made. Only one half of the semi-circular channel was modelled.

The difference between analytical and numerical values can be seen in Table 5.1. The error is considerably smaller for the 20×20 discretization, but even for the 10×10 discretization quite acceptable. It can be concluded that a mesh with about 10 elements over the depth of a glacier gives sufficient precision for most practical purposes. Since a discretization with more than 10 elements over the depth can be computationally expensive the errors of the 10×10 discretization are analysed more closely in Figs 5.1-a to 5.1-d.

Sometimes the flow transverse to the main flow direction is of interest. The FE formulation used allows the elements to be exactly incompressible in principle, but due to numerical errors this is not exactly so in practice. This causes some transverse flow even for infinite channels where no transverse flow should occur. It is important to estimate the magnitude of this "flow", which is linearly proportional to the main flow, and which expresses nothing but numerical errors. In Fig. 5.2 the horizontal component of the transverse flow (v_y), and in Fig. 5.3 the vertical component (v_z), are shown for a semi-circular channel with radius 100 m. The maximum horizontal velocity v_x was equal to one. This "numerical" transverse flow is surprisingly large, up to 3.5 % of the maximum horizontal velocity for v_z and up to 2 % for v_y. In general the errors are, however, much smaller, but this shows how careful one must be in interpretating calculated transverse flow results.

In Table 5.2 computed results for a semi-circular channel for $n = 1$ to $n = 5$, where n is the power law exponent in Glen's flow law, and the corresponding errors are listed. The errors of the velocity on the centerline do not seem to increase with n and are of the order of 0.2 %. The mesh was 3D and the results given are for one particular cross-section. Inspection of the results showed the centerline velocity to oscillate slightly along the x-direction. Taking this small oscillation into account the correct error estimate is 0.22 %. Errors smaller than this are accidental. The discharge errors increase somewhat with increasing n. It is not clear whether this is a result of the flow field errors or the errors involved with integrating the flow field to get the discharge. Since only the resulting error is of interest this question is of no concern.

In conclusion it can be said that the program MARC can be used for 3D non-linear calculations of glacier flow where thermal effects are not important. For about 10

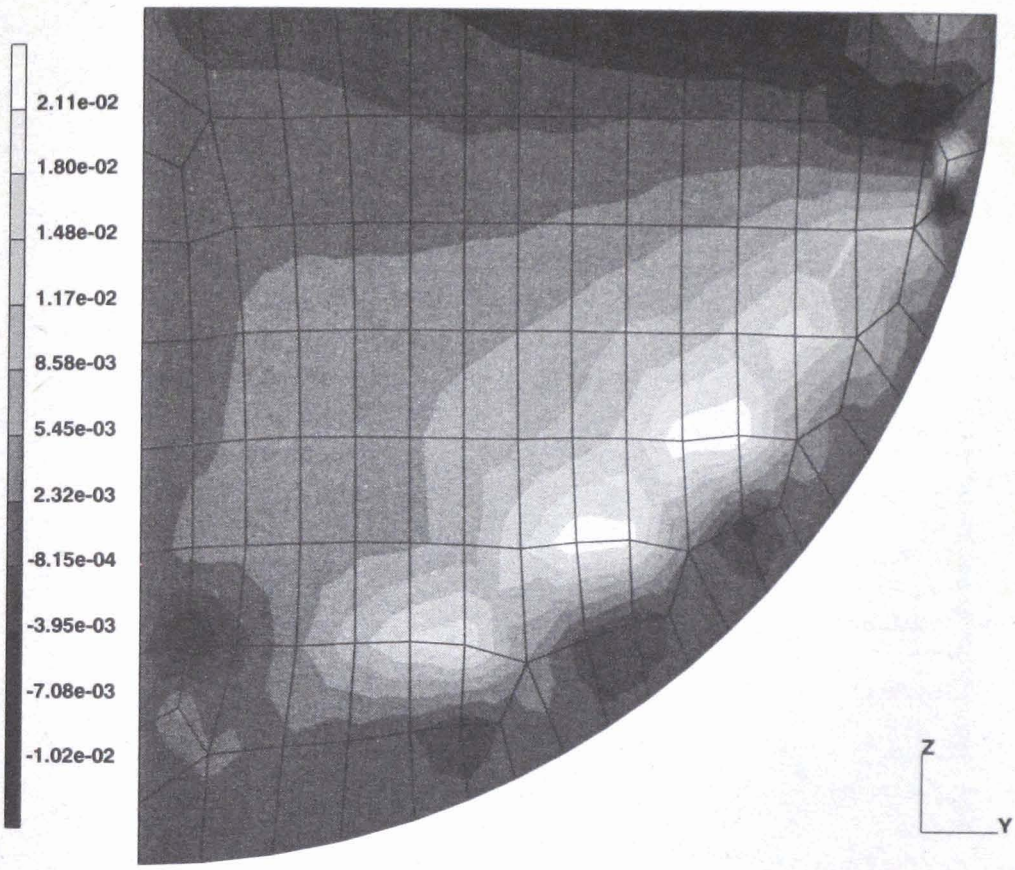

Fig. 5.2: Normalized transverse horizontal flow ($v_y/v_x(R=0)$) in a semi-circular channel. The figure depicts nothing but numerical errors. If the calculation were exact, there would be no transverse flow. The value of A was chosen such that v_x along the centerline was equal to one.

	U_0		Q	
n	Numerical	Error (%)	Numerical	Error (%)
1	0.250439	0.17	0.19636	0.0067
2	0.083507	0.21	0.078538	0.0023
3	0.031261	0.037	0.032703	0.066
4	0.012491	0.066	0.014004	0.14
5	0.0051980	0.20	0.0061178	0.29

Table 5.2: Comparison of numerical and analytical values for the velocity at the centerline and the discharge of a semi-circular channel. The numerical values were obtained with the 20×20 mesh.

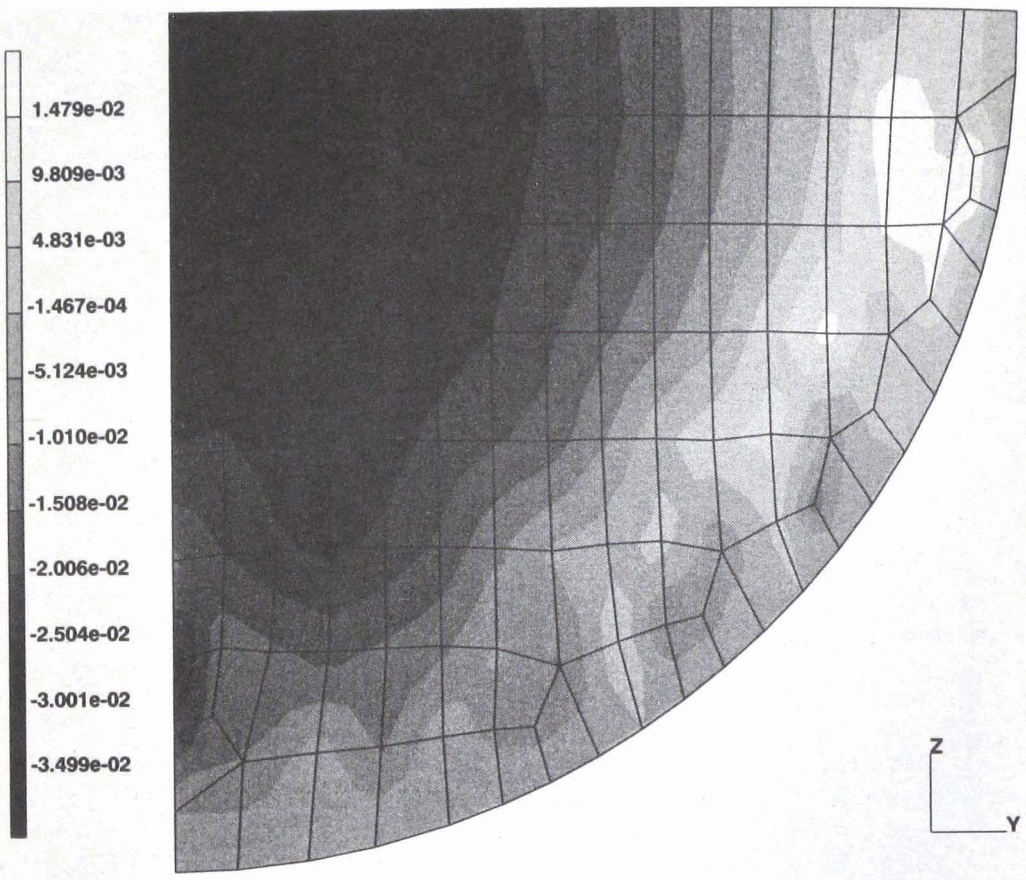

Fig. 5.3: Normalized vertical flow ($v_z/v_x(R=0)$) in a semi-circular channel.

elements over the depth the error is generally less then 0.5% but somewhat larger at the edges, or up to about 4%. There seems to be no reason to use more that 8 to 10 elements over the depth for most types of calculations.

5.1.4 Gravity driven flow down a channel of parabolic cross-section

Numerical solutions exist for glacier flow in channels of various cross-sections (Nye, 1965). Flows through a few parabolic channels having different aspect ratios were calculated. The aspect ratio (W) is defined as the ratio of the channel half width (b_p) to its depth (a_p), *i.e.* $W := b_p/a_p$. The suffix p refers to parabolic.

A program was written that transforms a semi-circular channel into a parabolic one. The idea behind the transformation formula used is explained in Fig. 5.4. The node p of the semi-circular FE mesh with coordinates (x, y, z), is transformed into node

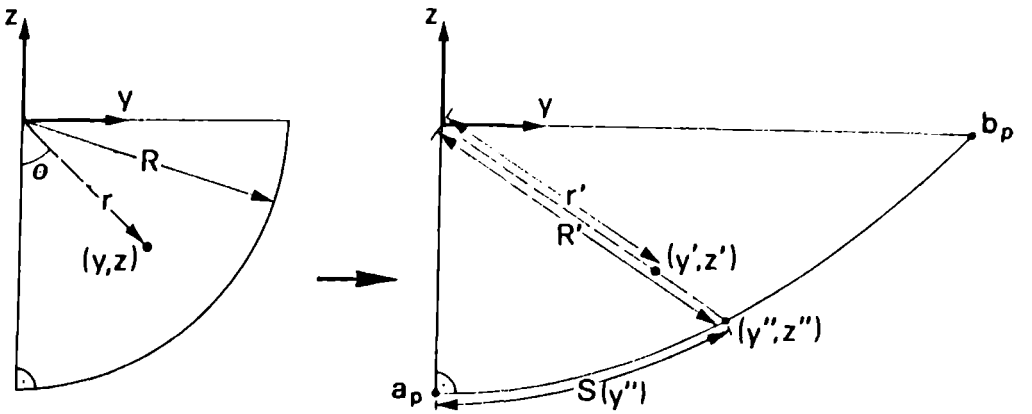

Fig. 5.4: Transformation of a semi-circular channel into a parabolic one. The point r with the coordinates (y, z) is transformed onto the point r' with the coordinates (y', z'). $S(y'')$ is the distance from the lower left corner of the parabolic channel (a_p) along the lower boundary to the point with the coordinates (y'', z''). (y'', z'') is defined as the point of intersection of a line going through the channels center point (the origin of the coordinate system) and the point r' with the lower boundary of the channel. The idea behind the transformation is that r/R should be equal to r'/R', and that $\theta/(\pi/2)$ should be equal to $S(y'')/S(b_p)$, where $S(b_p)$ is the distance from a_p along the bottom to b_p.

p' having the coordinates (x, y', z') of the parabolic mesh by requiring that

$$\frac{\theta}{\pi/2} = \frac{s(y'')}{s(b_p)} \tag{5.4}$$

and

$$\frac{r}{R} = \frac{r'}{R'(y'')}, \tag{5.5}$$

where $s(y'')$ is a function giving the length of the parabolic curve from $(y, z) = (0, R)$ to $(y, z) = (y'', z'')$. x points in the down-flow direction (making a vertical angle α to the horizontal), y is horizontal and perpendicular to the flow, and z points upwards. Let z_0 denote the z coordinate of the lower boundary of the parabolic channel:

$$z_0 = a_p((y/b_p)^2 - 1). \tag{5.6}$$

The function $s(y)$ is given by

$$\begin{aligned} s(y) &= \int_0^y \sqrt{1 + (\frac{dz_0}{dy})^2}\, d\hat{y} \\ &= \frac{\sqrt{2a_p}}{b_p} \int_0^y \sqrt{b_p^2/2a_p + y^2}\, d\hat{y} \\ &= \frac{\sqrt{a}}{\sqrt{2}b} \left\{ y\sqrt{b_p^2/2a_p + y^2} + \frac{b_p^2}{2a_p} \arcsin b_p y/\sqrt{2a_p} \right\}. \end{aligned} \tag{5.7}$$

Eq. (5.4) has no closed solution for y''. It was therefore solved numerically by finding the zero of the function $f(y) = 2\theta/\pi - s(y)/s(b_p)$. This procedure gave meshes that were only slightly distorted. An example of a mesh generated in this way is given in Fig. 5.5.

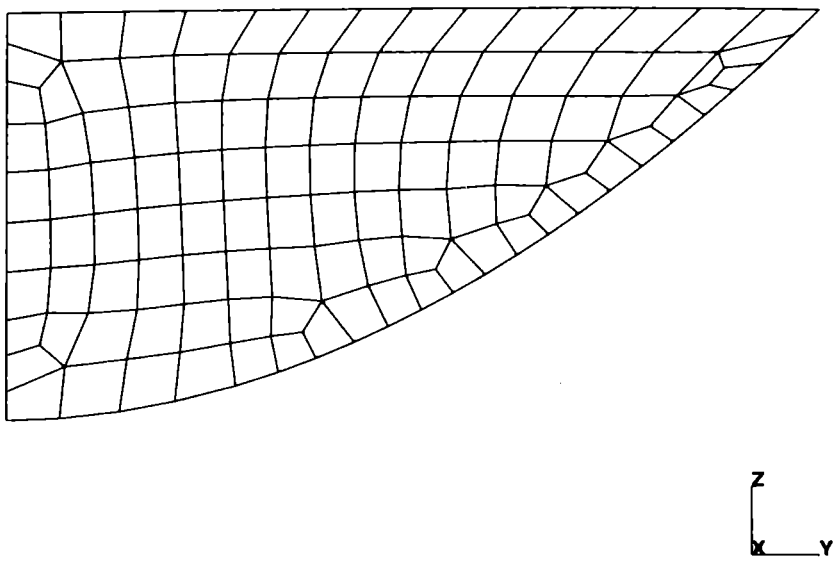

Fig. 5.5: Parabolic mesh with aspect ratio 2.

Results of the FE calculations are given in Table 5.3. They are compared with earlier results from Nye (1965) wherever possible. The form factor f is defined so that fz is the best linear approximation to the shear stress σ_{xz} giving the true surface velocity, if fz is integrated. A simple calculation shows f to be given by $f = ((n+1)U_0)^{1/n}$.[3] Nye (1965) gave estimates of the error in U_0 and the values in Table 5.3 agree within the range of errors.

Calculating the flow of the parabolic channels involved exactly the same steps as needed for the semi-circular channels, except for the additional use of the program transforming a semi-circular channel into a parabolic one. For error estimates the corresponding values in Table 5.2 can be used, as the errors are expected to depend mainly on n and to lesser extent on W.

f and Q as functions of W are plotted in Figs. 5.6 and 5.7 respectively.

For $W \to 0$ one finds that $U = W^{n+1}/(n+1)$, and that $f = W^{(n+1)/n}$, and since $n\,df/dW = (n+1)W^{1/n}$ the slope of $f(W)$ at $W = 0$, for any fixed value of n, is zero. On the other hand, if $n \to \infty$ and $W \to 0$ then the form factor is proportional to W, and the slope equal to one. This can be seen in Fig. 5.6 and explains the somewhat different slope of the curve for $n = 1$ with respect to the other curves

[3] In general the form factor will depend on the variation of basal sliding across the width of the channel. The form factors in Table 5.3 are valid for the special case of no, or uniform sliding. Highly non-uniform sliding across a glacier cross-section has been observed by Raymond (1971) at the Athabasca Glacier, where basal sliding velocities up to about 40 m/a and at the same time negligible marginal sliding was found. Reynaud (1973) showed that this kind of lateral sliding variation can for example result from a friction at the bed being proportional to effective normal pressure. Further numerical work, that resulted in better agreement with data from Athabasca Glacier, has been done by Harbor (1992), who used a sliding law dependent on basal shear stress and effective pressure, with the additional assumption of increased friction towards the margin of the glacier.

n	W	U_0	Q	f
1	0.25	0.025777	0.0039027	0.05155
	0.5	0.083069	0.026672	0.16614
	1	0.208831	0.13779	0.41766
	1.5	0.30003	0.29484	0.60007
	2	0.358132	0.46352	0.71626
	3	0.420510	0.79978	0.84102
	4	0.450332	1.12699	0.90067
2	0.25	0.0032176	0.000545513	0.09825
	0.5	0.016891	0.0063679	0.22511
	1	0.063681	0.05037	0.43708
	1.5	0.11079	0.13001	0.57653
	2	0.148571	0.22722	0.66762
	3	0.200355	0.43936	0.77528
	4	0.232740	0.65668	0.83559
3	0.25	0.00042698	0.000078841	0.11953
	0.5	0.0037698	0.001572	0.24705
	1	0.021771 (0.0221)	0.01914 (0.0199)	0.44325 (0.445)
	1.5	0.045694	0.059555	0.56751
	2	0.068117 (0.0675)	0.11539 (0.1172)	0.64829 (0.646)
	3	0.103610 (0.104)	0.24979 (0.255)	0.74557 (0.746)
	4.0	0.12898 (0.131)	0.39682 (0.404)	0.80204 (0.806)
4	0.25	0.000059572	0.000011671	0.13137
	0.5	0.00089236	0.00039802	0.25845
	1	0.013045	0.0074772	0.44634
	1.5	0.020074	0.028012	0.56286
	2	0.033204	0.060158	0.63832
	3	0.056627	0.145521	0.72945
	4	0.075239	0.245742	0.78317
5	0.25	0.0000086024	0.0000017582	0.13885
	0.5	0.00021933	0.00010256	0.26537
	1	0.0030124	0.00297799	0.44814
	1.5	0.0091756	0.013433	0.55996
	2	0.016814	0.031941	0.63207
	3	0.032085	0.086290	0.71927
	4	0.045424	0.15489	0.77106

Table 5.3: U_0 is the velocity at the centerline normalized by $2a_pA\tau_b^n$, and Q is the discharge normalized by $2Aa_p^3\tau_b^n$. The form factor was calculated according to $f = ((n+1)U_0)^{1/n}$. The numbers in the brackets are from Nye (1965). Calculated values are estimated to deviate less than 0.22% from exact ones.

that at first sight might seem to indicate an error. Notice that the curves in that figure result from simple interpolation and that the slope at $W = 0$ is incorrect. As n gets larger, increasingly smaller W values will be needed to make the correct slope become evident.

An interesting feature of Fig. 5.6 is the cross over of the $f(W)$ curves for $W \approx 1.2$. For larger W values increasing n and keeping W fixed has the effect of decreasing f.

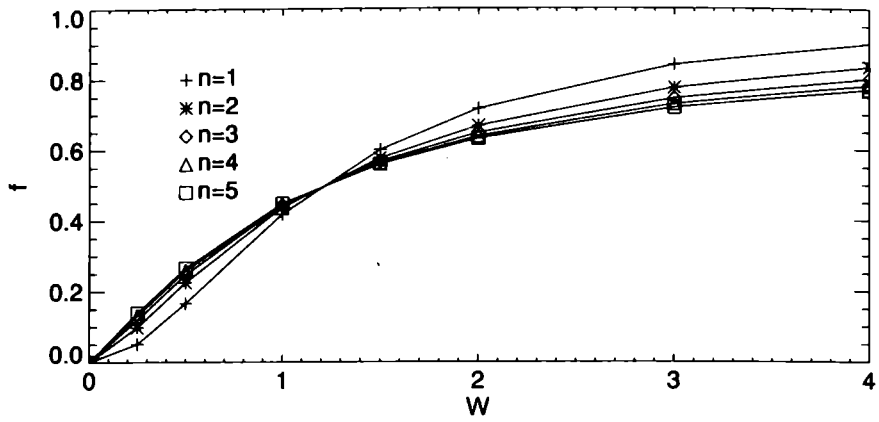

Fig. 5.6: Form factor f for parabolic channels as a function of W. Letting $W \to 0$ for a fixed value of n gives a slope of zero at $W = 0$. If, on the other hand, $n \to \infty$ and then $W \to 0$, the slope at W is equal to unity. Note the cross over of the curves. This happens at a value of W for which the drag from the bottom starts to be more important than the drag from the sides. Since the limiting value of $f = 1$ for $W \to \infty$ is approached more slowly for larger values of n, increasing n for a wide channels has the effect of making the glacier more aware of its finite width. For a narrow channel the situation is the same in the sense that increasing n makes the glacier more aware of its finite depth. As explained in the text, this can be understood to be a consequence of the stress redistribution caused by increasing the value of n. The effective stresses then become more uniformly distributed over the bed, and all sections of the bed tend to contribute more equally to the overall drag. Increasing n has thus the effect of making a valley glacier more aware of the shape of its cross-section.

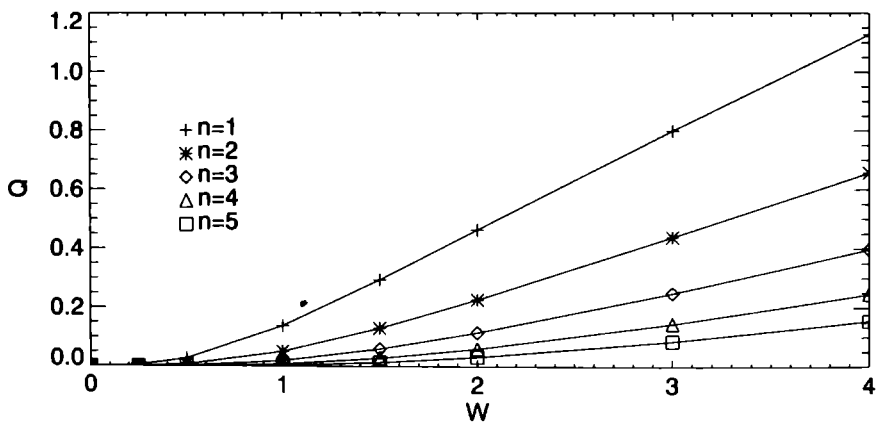

Fig. 5.7: Non-dimensional discharge, Q for parabolic channels as a function of W. Q is related to the dimensional discharge q through $q = 2A\tau_b^n a_p^3 Q$.

For smaller W values it is the other way round; f increases with increasing n. This shows that for a wide glacier (wide in the sense of $W \gg 1$) the effects of the sides are felt more closely with increasing n, since the asymptotic value of 1, as W approaches infinity, is reached more slowly. Conversely, for a narrow glacier ($W < 1$) the drag from the bottom has a larger effect on the centerline velocity as n increases. One

can therefore say that increasing n has the effect of making a valley glacier more aware of the shape of the cross-section.

The cross over is where the drag from the side starts to dominate the drag from the bottom. For an elliptical channel the cross over would hence be expected to be at $W = 1$ but for a parabolic channel this is not necessary true, and as Fig. 5.6 shows the cross over is at $W > 1$. This is of course caused by the curvature of the channel. Since the point of the bed closest to the centerline is always the point of largest shear stress (Nye, 1965), the location of this point along the transverse section as a function of W is important for the relative contribution of the sides to the overall drag. For a parabolic channel one can easily show that the point of the bed lying closest to the centerline is on the "side" of the parabolic profile, in the sense that a straight line from the center to this point then makes an angle that is greater than $\pi/4$ to the vertical, if $W > \sqrt{2}$.[4] Thus, because of the curvature of the parabolic curve, the cross-over point would be expected to lie between 1 and $\sqrt{2}$, as it does.

With increasing n the effective stresses across the bed are redistributed and the stress distribution becomes more uniform. For a wide glacier this means that the relative contribution of the sides to the drag becomes larger. Hence the sides are "felt" more strongly and the value of form factor decreases. For a narrow glacier the situation reverses. This explains the cross over in Fig. 5.6.

For $W \to \infty$ the parabolic channel becomes an infinitely wide channel of uniform depth and $f \to 1$ and $U \to 1/(n+1)$.

Nye gives, for the asymptotic slope of the $Q(W)$ curve,

$$\lim_{W\to\infty} \frac{Q}{W} = \frac{2}{n+2} I(2n+5) \tag{5.8}$$

where $I(r) = \int_0^{\pi/2} \cos^r d\theta$, or

$$\lim_{W\to\infty} \frac{Q}{W} = \frac{1}{n+2} \frac{\Gamma(1/2)\Gamma(n+3)}{\Gamma(n+7/2)} \tag{5.9}$$

where Γ is the gamma function. This expression is valid for all values of n (and not just for integers as is the case for the expression given by Nye (1965)). Hence, for $n = [1, 2, 3, 4, 5]$ the asymptotic slope of the $Q(W)$ curve is [0.3048, 0.2032, 0.1478, 0.1137, 0.09093] respectively. This is in good agreement with Fig. 5.7. The slope between $W = 3$ and $W = 4$ is for example equal to 0.2173 for $n = 2$, and 0.1470 for $n = 3$.

In the limit $W \to 0$, it can be shown (Nye, 1965) that $(n+2)(n+4)Q \to 4W^{n+2}$, which explains the flattening of the curves in the figure.

5.1.5 Flow over a sinusoidal bed

The flow over a frictionless sinusoidal bed was calculated and the results compared with the analytical solution given in Sec. 4.1.

[4] To see this minimize $R^2 := y_0^2 + z_0^2$ with respect to y_0, giving $y = b_p\sqrt{1 - W^2/2}$ and $z = a_p((1 - W^2/2) - 1)^2$, and then solve $y_0/z_0 = 1$.

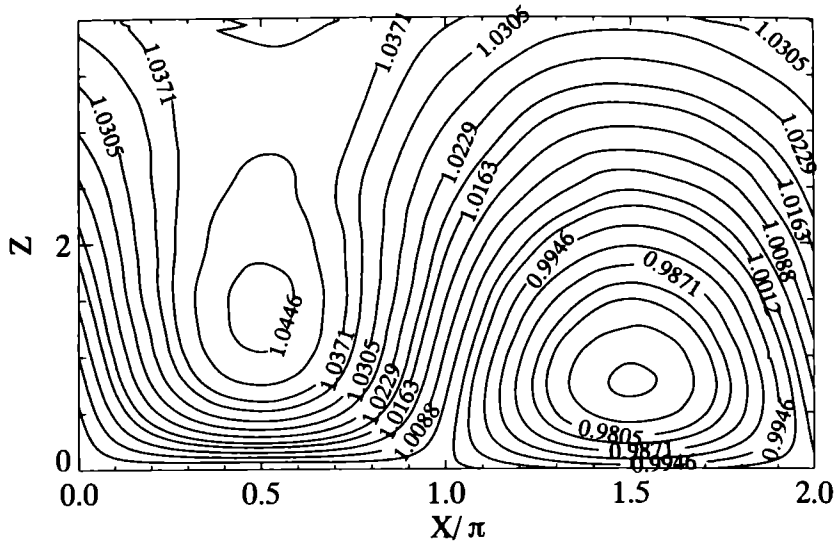

Fig. 5.8: Calculated horizontal velocity of flow over sinusoidal bed for $n = 1$. The vertical position of the bed z_0 is given by: $z_0 = a \sin kx$. The velocities were normalized by the sliding velocity u_b. X and Z are non-dimensional coordinates defined as $X = kx$ and $Z = kz$. The peak of the sinusoidal bed is at $X/\pi = 1/2$ and the trough at $X/\pi = 3\pi/2$. The values of the slope parameter $\varepsilon = ak$, and the thinness parameter $\delta = 1/(hk)$, were $\varepsilon = 0.3\pi$ and $\delta = 0.05/\pi$.

In Fig. 5.8 the calculated horizontal velocity field for $a/\lambda = 0.015$, $\lambda/h = 0.1$, $\sin\alpha = 0.01$ and $\rho_I g = 8.99577 \times 10^3\,\mathrm{kgm^{-2}m^{-3}}$ is shown. The domain had dimensions of 200 times 200 meters, and the FE mesh had 5395 nodes and 5038 elements. For the region in the figure the nodal values were used for creating an evenly-spaced grid with 200 times 200 points, which was then used for the contouring. The points $U^{\min}_{3\pi/2}$ and $U^{\max}_{\pi/2}$ can be seen.

The velocity field was normalized by the calculated sliding velocity $u_b = 21.24472$ m/a, which gives $s(3\pi/10, 1/(20\pi), 1) = 0.9866$, a value close to the theoretical one of $s(0,0,1) = 1$. $s(\varepsilon, \delta, n)$ is the sliding function, defined as

$$s(\varepsilon, \delta, n) := \frac{\varepsilon^{n+1} k u_b}{2A\tau_b^n} \tag{5.10}$$

The mean of the vertical velocity ($< v_z >$) along the bed should be equal to zero, but due to numerical errors will never be exactly so. The calculated value was $< v_z >= -1.417 \times 10^{-4}$, or five orders of magnitude less than the sliding velocity.

In Fig. 5.9 the horizontal velocity field as given by Eq. (4.1) is depicted. Here again the velocity field was normalized by the sliding velocity, but the value for u_b used was not the numerical one, but that according to (4.3). It can be seen that there is almost no difference between these two figures by looking at Fig. 5.10, where the difference is shown in percentage terms. The difference is small, always within the range of -0.06 to $0.12\,\%$. It is therefore concluded that the errors involved with the numerical solution are less than 0.1%. This error estimate can only be used for the calculations of linear viscous media. For non-linear rheology the corresponding

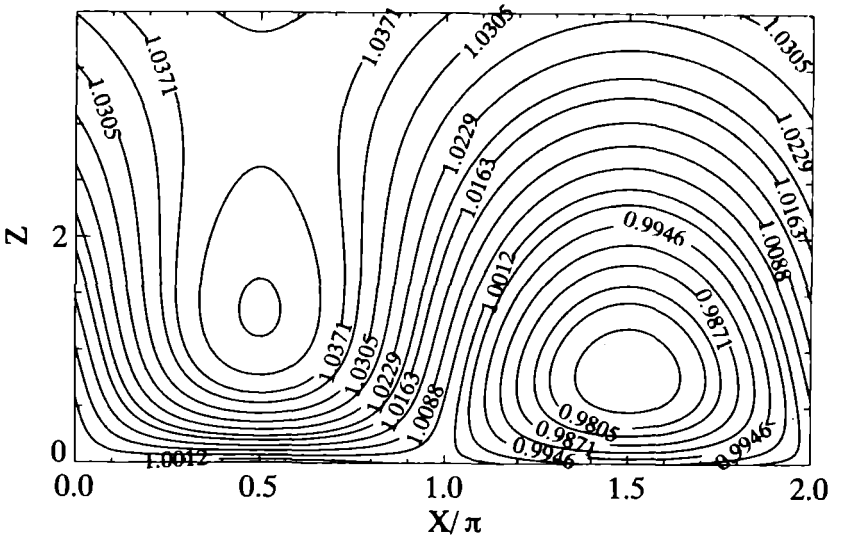

Fig. 5.9: Analytical horizontal velocity for $n = 1$, $\varepsilon = 0.3\pi$ and $\delta = 0.05/\pi$. Horizontal velocity $v_x(x,z)/u_b$ as given by Eq. (4.1). A comparison with Fig. 5.8 shows how similar the results obtained by FE calculations are.

non-linear equation system has to be solved iteratively until a prescribed accuracy is obtained. In principle a much better accuracy can be obtained but that may require an unreasonably large amount of computer time.

The iterations were continued until the maximum change in velocity over the whole model divided by the maximum velocity was less than some prescribed value, which was chosen to be equal to 0.0001 or 0.01 % for all of the calculations. Although this is a truly small value the accuracy of the non-linear results will be somewhat less than the linear ones. How much larger the errors are is difficult to estimate exactly since no analytical solutions are available, but assuming that the only additional source of error is the iteration procedure the errors should be less than 0.2 %. There is, however, another source of error; the effective viscosity distribution can only be as accurately represented as the FE discretization allows, with every integration point assigned one effective viscosity value. This discretization error does not play a role if a linear viscous medium is modelled, since then the viscosity is constant over the whole domain. In the non-linear case it must be estimated by solving the same problem with different FE meshes. Several calculations using a mesh of 4302 elements and 4636 nodes were therefore done. The results, compared with the finer discretization, differed by less than 0.3 %.

5.2 Discretization errors

Discretization errors were estimated by: a) generating several meshes with different numbers of nodes and elements, and b) by comparing the nondimensionalized results obtained by different meshes characterized by the same nondimensional numbers ε, δ and n, but different dimensional numbers such as a, λ, τ_b and h.

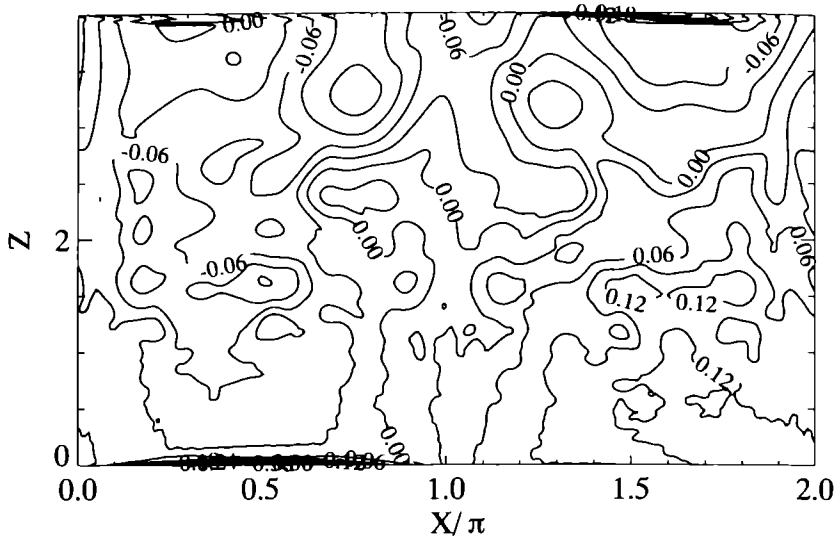

Fig. 5.10: Percentage differences between a numerical and the analytical solutions of highly viscous flow over a sinusoidal bed.
Differences between analytical and numerical results for the horizontal velocity in percents, i.e. $100\,(v_x^a(x,z) - v_x^{\mathrm{FE}}(x,z))/v_x^a(x,z)$, where a stands for analytical and FE for numerical results obtained by an FE calculation, for $\varepsilon = 0.3\pi$ and $\delta = 0.05/\pi$. One sees therefore the percentage difference between Fig. 5.8 and Fig. 5.9. The error is never larger than $0.12\,\%$, and usually much less. There is a small systematic tendency of the error to be positive for $X > \pi$ and negative for $X < \pi$. By generating similar figures for different values of the thinness parameter δ, it was discovered that this discrepancy is due to the assumption in the derivation of the analytical solution that δ is approximately zero. The numerical solution is therefore even more precise than the figure indicates. The analytical solution is defined for $z > 0$ whereas the numerical one is defined for $z > z_0$. No attempt was made to account for this difference, which is the reason for the "black" area close to $(X, Z) = (1/2, 0)$.

The lines in Table 5.4 show the percentage difference in $s(n, \varepsilon, \delta)$ obtained from two calculations done with different values of the dimensional parameters λ, a, and h, which give the same dimensionless ratios ε and δ ($r = \varepsilon/2\pi$ and $\varsigma = 2\pi\delta$), and should therefore give exactly the same results. The error is almost always less than $0.2\,\%$. For $n \neq 1$ there is a tendency of the error to get larger as r increases. This is most probably due to the fact that as r becomes larger there is an increased stress concentration at the peaks of the bed protubances, leading to large variations in the effective viscosity over a limited area, which can only be approximately represented by the FE mesh.

n	Corrugation (r)	Asperity (ς)	Difference (%)
1	1.2566370	0.10	0.026
	3.1415930	0.10	0.008
	0.1005310	0.05	0.001
	0.1130973	0.05	0.001
	0.1256637	0.10	0.001
	0.2513274	0.10	0.001
	0.3141593	0.10	0.003
	0.376991	0.10	0.005
	0.5654867	0.10	0.945
	0.6283185	0.10	0.011
	0.0565487	0.05	0.055
	0.0628319	0.10	0.092
	0.0062832	0.10	0.009
	0.0691150	0.05	0.067
	0.0753982	0.05	0.001
	0.0816814	0.05	0.153
2	1.2566370	0.05	0.650
	1.3823010	0.05	0.209
	0.6283185	0.05	0.058
	0.9424778	0.10	0.043
3	1.2566370	1.00	0.220
	1.2566370	0.1666667	0.435
	1.3823010	0.05	0.235
	0.1256637	1.00	0.215
	0.1256637	0.10	0.044
	0.1256637	0.50	0.145
	0.3769911	0.10	0.176
	0.6283185	1.00	0.182
	0.9424778	0.10	0.407
4	1.2566370	0.20	0.059
	1.3823010	0.05	0.877
	0.9424778	0.10	0.208
5	1.3823010	0.05	0.991
	6.2831850	0.05	0.216

Table 5.4: Comparison of results obtained for different FE grids but for the same dimensionless numbers n, r and ς. Every line of the table shows the values of n, r, and ς for two calculations with different values of λ, a, and h (not tabulated). The last column shows the difference in percent of the calculated values for the function $s(n, \varepsilon, \delta)$ between these two calculations, which should theoretically be zero.

CHAPTER 6

Numerical Calculations of Flow Over a Sinusoidal Bed

Up to this point the emphasis has been on theoretical work done on perfect sliding over a sinusoidal bed although some numerical work has also been mentioned. In this chapter the flow of a viscous material over a sinusoidal bed for free-slip boundary conditions will be analysed. The analytical results that are only valid for slight roughness will be extended to extreme roughness and the effect of a non-linear flow law on the sliding velocity and on the flow characteristics will be examined.

6.1 Objectives

The flow of linear viscous material over a sinusoidal bed for $\varepsilon \ll 1$ and $\delta \approx 0$ is rather well understood. Eqs. (4.1), (4.2), (4.32), (4.31) and (4.33) gave some new insight. In general however, even for the linear case, the dependence of the sliding velocity on ε and δ is not known. For a power-law fluid the relationship is still less clear since the asymptotic behavior of u_b for $\varepsilon \to 0$ is, as said before, a subject of debate.

Neither is the effect of δ on the sliding velocity clear. Claims have been made that u_b depends linearly on δ (Fowler, 1979) independent of n, but this has also been questioned since physically one might expect u_b, in the limit of small δ values, only to be dependent on h through its dependence on τ.

The aim of the numerical modeling was to get answers to the following questions:

1. How does U_b depend on ε in the limit $\varepsilon \to 0$ for $\delta \ll 1$? Is Eq. (3.23) correct?
2. How does u_b vary as a function of n.
3. How does u_b depend on δ?
4. How exact are the predictions made for the appearance/disappearance of extrusion flow at certain ε values?
5. Is extrusion flow for $n > 1$ possible, and how does n effect its magnitude and its dependency on ε?

6.2 Solution method

The differential equations that are to be solved are the conservation Eqs. (2.4), (2.5) together with Glen's flow law (Eq. (2.1)) given in Sec. 2.1.1.

The solution procedure applied was the method of finite elements. Commercially available FE software, the general purpose program MARC, was used for the calculations. This program proved to be well suited, especially because the user can add user-defined subprograms to the main code and recompile it. In this manner the program can be extended and modified in order to fit the needs of the particular person using it. MARC is actually not designed for fluid analysis and Glen's flow law is not implemented. The implementation of Glen's flow law, after having contacted the program developers, nevertheless turned out to be rather easy. One of the strong points of MARC is that it allows the calculation of a truly incompressible medium and offers iteration algorithms for the handling of systems of non-linear equations.

A comprehensive testing of the correctness of the numerical results obtained with MARC was done. A description of the testing procedure and the results obtained is given in Chapter 5. In addition to giving information on the numerical errors involved the testing procedure also gave results that are possibly of general interest. An example of this is a calculation of form factors for parabolic channels for a considerably larger range of parameters than was originally done by Nye (1965).

The FE element chosen was a four-noded isoparametric element with bilinear interpolation. Linear elements tend to give better results for non-linear calculation although a somewhat larger number of subdivisions may be needed. To enforce incompressibility two methods were used: a) selective integration, where the four Gaussian points are used for the deviatoric contribution, and the centroid for the dilatation contribution, a method also known as the constant dilatation method, and b) the Herman variational principle using $(\mathbf{v}, p)$-formulation (mixed formulation) where a fifth node for the pressure degree of freedom is added to the center of the element. The pressure is constant within the element (it can be shown that the pressure interpolation function must be of one degree lower than the velocity functions if the resulting equation system is to be non-singular).

To improve the bending characteristics of the element the assumed strain formulation was used, where the interpolation functions are expressed with respect to the distorted element.

Due to the non-linearity of the flow law the solution must be sought in an iterative way. The method of direct substitution was used, *i.e.* the old effective viscosity distribution was repeatedly substituted by a new one based on the calculated strain rates using the old distribution. The iteration was continued until the ratio of the maximum change of the velocity at some node in the FE mesh during the last iteration, divided by the maximum node-velocity, was less than a specific value, set to 0.0001. Experience with other FE programs such as RHEO-STAUB has shown that it is sometimes necessary to damp the iteration in order to ensure convergence, and to use as a new effective viscosity some weighted average of the old viscosity and the one based on the resulting strain rates. With MARC this turned out not to be necessary except for $n < 1$.

To reduce computation time the effective viscosity of every integration point of every element was written to a file and during subsequent calculations the resulting effective viscosity of the most similar calculation was used as a starting value, which led to substantial reduction of CPU-time.

6.3 Mesh generation

Since a large number of models with various different ε and δ values was to be calculated, it was impractical to generate a new FE mesh for each and every calculation. Instead a small number of rectangular meshes were generated, which were then — through the use of transformation formulae — transformed into the desired shape.

The transformation formulae were

$$x' = ae^{-z/h-ak/2}(\xi_1 + \xi_2 - \xi_1 e^{-kz} - \xi_2 e^{kz}) \sin kx + x, \tag{6.1}$$

$$z' = a(\xi_1 e^{-kz} - \xi_2 e^{kz}) \cos kx + z(1 + ak(\xi_1 + \xi_2)(e^{-z/a} - e^{-h/a}), \tag{6.2}$$

where

$$\xi_1 := \frac{e^{kh}}{2 \sinh kh} \qquad \text{and} \qquad \xi_2 := -1 + \xi_1, \tag{6.3}$$

(x', z') denote the transformed values and (x, z) the original ones. Note that the bed was defined by

$$z_0 = a \cos kx \tag{6.4}$$

and not $z_0 = a \sin kx$. In some cases the mesh was scaled linearly in both directions prior to the use of (6.1) and (6.2), keeping the wavelength fixed, to obtain different wavelength-to-thickness ratios. In this way it was also possible to apply different scalings to get different meshes with the same ε and δ values, making it relatively easy to estimate the numerical error associated with a change in mesh geometry.

The transformation formula was found by starting with the formulation:

$$z' = f(z)a \cos kx + g(z) \tag{6.5}$$

where $f(z)$ and $g(z)$ are some unknown functions satisfying: $f(0) = 1$, $f(h) = 0$, $g(0) = 0$ and $g(h) = 1$. It is desirable that the transformation formula gives approximately a conformal mapping, but it should not be an exact conformal mapping because there will inevitably be a "crowding" of the transformed z'-lines, giving bad aspect ratios for the generated elements (Menikoff and Zemach, 1980). The Cauchy-Riemann equations are

$$x'_x = z'_z \qquad \text{and} \qquad x'_z = -z'_x \tag{6.6}$$

Putting (6.5) into the left-hand side of (6.6) and integrating gives

$$x' = akF(z) \sin kx + K(x), \tag{6.7}$$

where F is the integration of f and K is an unknown function. Using the right-hand side of (6.6) gives a differential equation for $f(z)$, which can easily be solved

$$f(z) = a_1 e^{-kz} - a_2 e^{kz}, \tag{6.8}$$

where a_1 and a_2 are constants, and $g_z = K_x$, which gives $g(z) = a_3 z$ and $K(x) = a_3 x$. It is required that for $z = 0$, z is transformed to z_0, and to $z' = h$ for $z = h$. In order to avoid the negative aspects of crowding the factor $e^{-z/h-ak/2}$ was introduced, which makes the transformation non-conformal. It then turned out to be necessary to ensure that the transformation is one-to-one[1], which was guaranteed by requiring $z'_z > 0$ and $x'_x > 0$. Eq. (6.1) and Eq. (6.2) can be seen as a compromise between the positive aspect of a conformal mapping giving small skewness values for the generated elements, and the negative aspect of the crowding, which gives large aspect ratios. This transformation gave an excellent FE mesh and could be used for all values of ϵ and δ of interest.

6.4 Boundary conditions

The top of the model is a free surface; there σ_{zz} and σ_{xz} are equal to zero. The atmospheric pressure was ignored.

The perfect sliding condition was applied to the bottom nodes. It was implemented by suppressing all movements in the direction normal to the bed and allowing free movements in the tangential direction.

At the sides a periodic velocity boundary conditions was specified, *i.e.* the left side was forced to have the same velocity profile as the right side. The model is infinite and periodic. No prior knowledge of the velocity or of the stress tensor along the edges was needed.

6.5 Post-processing

There were basically two types of post-processings performed. One was the direct visual inspection of the results of an individual calculation with the post processing program Mentat. This was time consuming and could only be done for a limited number of runs. The other one consisted of an automatic calculation of all quantities of interest. Various subroutines from the IMSL collection of numerical algorithms were applied in doing so(IMSL, 1989).

A one dimensional periodic B-spline interpolation through the velocity values at the bed was made to obtain equally-spaced velocity values along the x axis, which were then Fourier transformed and used for calculating the mean of v_x, *i.e.* the sliding velocity.

The velocity field was interpolated by the use of a bilinear interpolation function that was consistent with the FE mesh and the FE interpolation functions used. The searching procedure for $U^{\max}_{\pi/2}$ and $U^{\min}_{3\pi/2}$ involved a non-linear constrained minimization/maximization problem because the z extension of the region of interest is dependent on the value of x. As starting values for the positions of $U^{\max}_{\pi/2}$ and

[1] A function $T : V \to W$ satisfying $T(x) = T(y)$ and implying $x = y$, is said to be one-to-one on V.

$U^{min}_{3\pi/2}$ the analytical results discussed in Sec. 4.3.2 were used. The positions of $U^{max}_{\pi/2}$ and $U^{min}_{3\pi/2}$ within the FE mesh were also found using the nodal velocity values and compared with those found by interpolation. The difference was never large, which is the expected results, or comparable to the size of the elements. By interpolation of the nodal values somewhat more precise results were obtained than otherwise, as $U^{max}_{\pi/2}$ and $U^{min}_{3\pi/2}$ could then be found somewhere within the elements. This allowed a better comparison between theoretical and numerical results.

6.6 Numerical results

6.6.1 Sliding velocity

In Sec. 3.2 it was shown that in the limit as $\varepsilon \to 0$ and for $\delta \ll 1$ the sliding function s, defined by Eq. (3.24) will be a constant c_0 that is independent of ε but depends on n, *i.e.*

$$\lim_{\varepsilon \to 0} s(\varepsilon, \delta, n) \overset{\delta \ll 1}{=} c_0(\delta, n), \tag{6.9}$$

and it was argued that $c_0 = \hat{c}^{1-n}$ with $\hat{c} \approx 2$. Otherwise no estimates of the sliding function s could be made, and it was realized that numerical work could give some more information about s.

The sliding function was calculated for $n = 1$ to $n = 5$, for $r = 0.001$ to $r = 1.0$ and for ς in the range from 0.025 to 1.0. Some of the results can be seen in Fig. 6.1 and in Fig. 6.2, which show $\ln s$ as functions of $\ln \varepsilon$ for $n = [1, 2, 3, 4, 5]$ and for $\delta = 0.05/(2\pi) \ll 1$ and $\delta = 0.1/(2\pi)$ respectively. The figures display a number of interesting features:

- For small ε values all curves have zero slope. Eq. (6.9) is therefore correct, and the sliding velocity is, for ε small enough, proportional to $\varepsilon^{-(1+n)}$ as Eq. (3.23) indicates. This can be seen more clearly in Fig. 6.5-a that shows the function U_b, or the nondimensional sliding velocity (defined through Eq. (3.6)), for $\varepsilon < 0.125$.[2] The slope of the $f(\varepsilon)$ curves is given in Table 6.2, and depicted as a function of n in Fig. 6.5-b. The calculated slope is $-1.017 - 0.986\,n$, or within 2 % from the theoretical slope of $-(1 + n)$.

- The range of the validity of Eq. (3.23) depends on n. As n increases this range of ε values gets smaller, contrary to statements made by Fowler (1981, p. 675) who argued that ε^{n+1} had to be small. For $n = 5$, ε must for example be smaller than about $e^{-2} \approx 0.135$ ($r < 0.0215$) for Eq. (3.23) to be a approximation valid within 20%. Although a value less than 0.02 for r is not unreasonably small, this fact considerably reduces the usefulness of Eq. (3.23). For $n = 1$ the variation of s is slow; not until $\varepsilon = 1.0$ is s 20% different from $s(0, 0.05/2\pi, 1)$.

- For ε and δ fixed $\ln s$ changes by a constant amount for every unit change in n, *i.e.* $\ln(s(\varepsilon, \delta, n + 1)) - \ln(s(\varepsilon, \delta, n)) = \Delta(\varepsilon, \delta)$. It is an important fact that

[2] U_b and s are connected through $s = \pi \varepsilon^{n+1} U_b$.

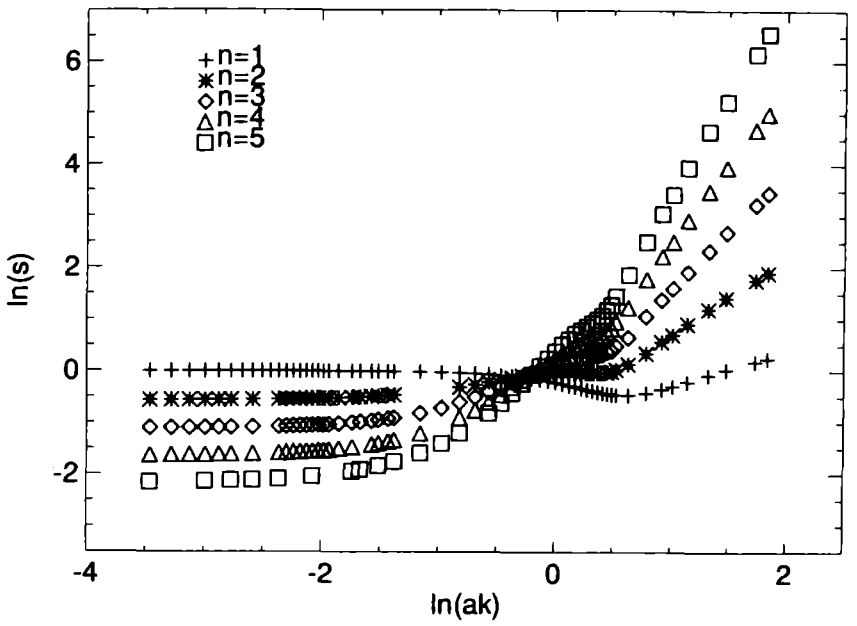

Fig. 6.1: The logarithm of the sliding function s as a function of $\ln\varepsilon$ and n for $\varsigma = 0.05$. Every symbol represents the result of one calculation. The constant slope of the curves for $\varepsilon \to 0$ shows that $u_b \propto \varepsilon^{-(n+1)}$ in that limit. The range of ε values for which this asymptotic expression is correct depends on n, and becomes smaller with increasing n. Note that for every particular value of ε there is a constant shift in the value of $\ln s$ with each unit increase in n. This means that $\ln s$ is a linear function of n. It is therefore not necessary to calculate s for every possible value of n; all that is needed is a simple interpolation or extrapolation of the calculated values.

Δ does not depend on n. Hence, one does not have to calculate s for every possible value of n. A simple interpolation or extrapolation based on several different n values will suffice. In Fig. 6.3 the logarithm of the sliding function s is shown as function of n for a few roughness values r and a fixed corrugation value of $\varsigma = 0.005$. It is seen that a straight line always results, but with a slope dependent on ε. For $\varepsilon = 0.005$ (the smallest value of ε in the figure)

$$\ln s(0.005, 0.05/2\pi, n) = 0.5138 - 0.5370\, n \tag{6.10}$$

with a standard deviation of 0.010. Eq. (3.29) predicted this power-law behavior but with a slope of $-\ln 2 \approx -0.69$. Notice that relation (6.10) gives $\ln s = -0.0232 \neq 0$ for $n = 1$, although s was defined in such a way that $\ln s(0, 0, 1) = 0$. This discrepancy is not entirely a result of numerical errors since it was obtained with finite values of ς and ε.

For $\delta = 0.05/2\pi$, s was approximated as

$$s(\varepsilon, \delta, n) = \sum_{i=0}^{6} c_{2i}(\delta, n)\, \varepsilon^{2i} \tag{6.11}$$

for $\varepsilon < \pi/2$. The resulting curves are seen in Fig. 6.4, which shows s as a function of ε^2, and the values of the Taylor coefficient are given in Table 6.1.

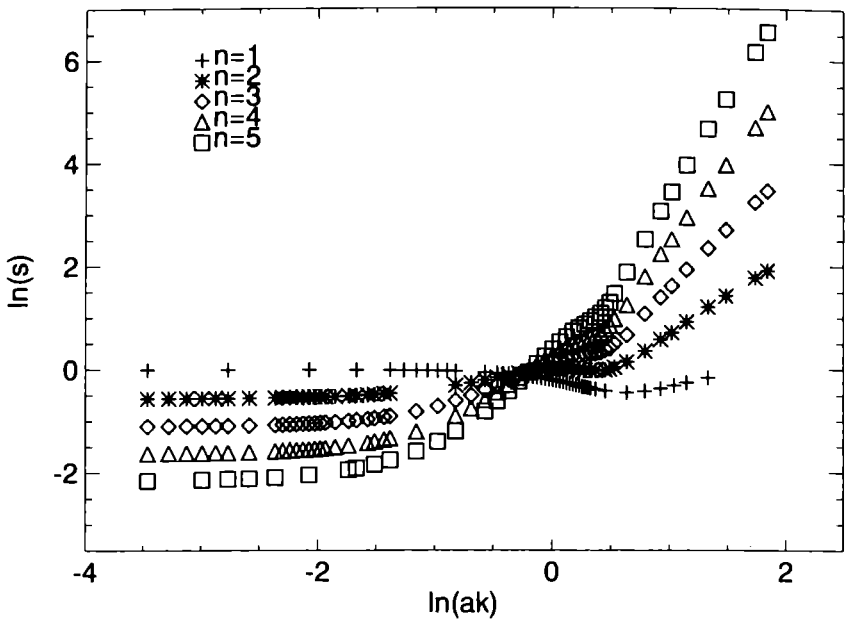

Fig. 6.2: $\ln s$ as a function of $\ln \varepsilon$ and n for $\varsigma = 0.1$. The only difference between this figure and the previous one is the value used for δ. No difference can be seen, showing that the results do not depend on the exact value of δ.

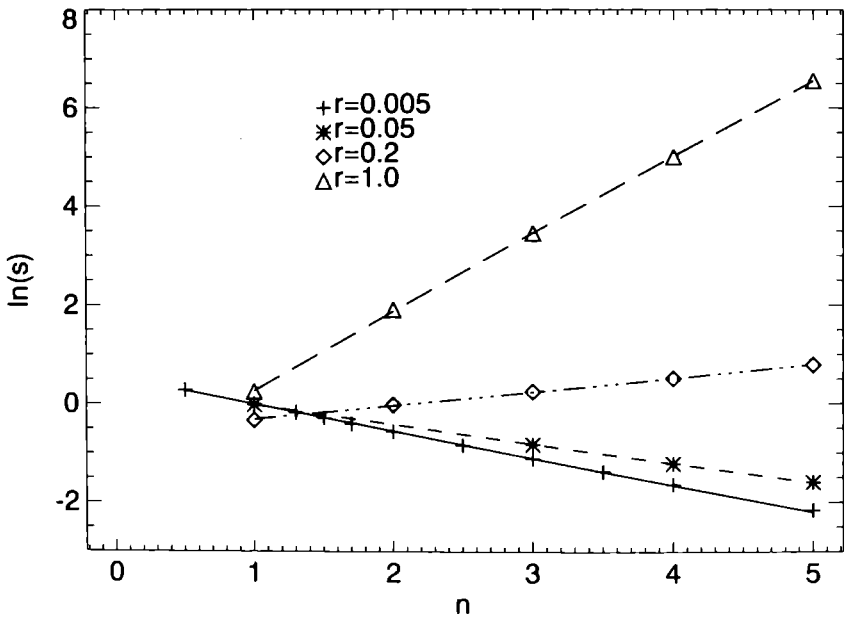

Fig. 6.3: $\ln s$ as a function of n for several roughness values r and $\varsigma = 0.05$. For every roughness value r a linear relationship between $\ln s$ and n is found, with a slope that depends on r. s is defined in such a way that the limiting value of $\ln s$ for $r \to 0$ and $n = 1$ is equal to unity.

If s is needed for some other n, s should be calculated according to Eq. (6.11) and interpolated or extrapolated using the fact that $\ln s(,,n) = \hat{c}_1 + \hat{c}_2 n$ where $\hat{c}_1$ and $\hat{c}_2$ are obtained through a least squares approximation.

Attempts to extrapolate to $\varsigma = 0$ did not convincingly result in improvements, partly because practically the same slopes were obtained for different δ values as long as $\delta \ll 1$ but more importantly because s was calculated for a rather limited number (≈ 10) of wavelength-to-thickness ratios. Comparison of Fig. 6.1 and Fig. 6.2 shows that a factor of two change in δ does not change s significantly, *i.e.* ε is much more important for s than δ (How s depends on δ will be discussed in Sec. 6.6.2.). By calculating the slope of the $s(\varepsilon)$ curve for different values of δ, it could be shown that the small but finite value of δ is responsible for the 0.64 % deviation of $c_0(0.05/2\pi, 1)$ from 1 seen in Table 6.1. Although this deviation is small, a standard statistical test showed it to be significant.

The values of c_0 for $n = 3$ from Table 6.1 is in agreement with the estimate (3.26) from Meyssonnier based on theoretical arguments. The value of $c_2(0,3) = 1.163 \pm 2\%$ from Table 6.1 is, however, most probably not in accordance with his estimate for $c_2(0,3) = 2.4$. This deviation could be caused by the limited number of calculations, numerical errors, or both. Despite this difference there seems to be no reason to doubt the general correctness of Meyssonnier's findings.

The numerical results are also in agreement with Lliboutry's (1993) theoretical upper estimate for $s(0,3)$

$$s(0,3) \leq 0.33839 + 3.688\,\varepsilon^2 + 0.17\,\varepsilon^3 \tag{6.12}$$

and his tabulated values for s (Lliboutry, 1993, p. 62). His upper estimate is, however, up to several times greater than the calculated values.[3]

- All curves in Fig. 6.2 intersect at $\ln\varepsilon \approx -0.3$. This fact does not need any special attention. If one wants to compare s for different n as a function of ε, s would have to be made comparable by, for example, normalising it with c_0. Then all one could say is that $s(\varepsilon, \delta, n+1) > s(\varepsilon, \delta, n)$.

- For $\ln\varepsilon > 1$, $U_b \propto \varepsilon^p$, where p depends on n. This can be seen in Fig. 6.5-c, and in Fig. 6.5-d where $\partial \ln U_b / \partial \ln\varepsilon$ for $\ln\varepsilon > 1$ as a function of n is depicted. The best straight line approximation is given by $-1.11 - 0.228\,n$ with a standard deviation of 0.010, *i.e.* $U_b \propto \varepsilon^{-1.11-0.228\,n}$. Hence, for extreme roughness the sliding velocity is not dependent in the same way on ε as it is for slight roughness.

$s(\varepsilon, \delta, n)$ as a function of ε and ς for $n = 3$ is shown in Fig. 6.6. Diamond symbols represent the (ε, ς)-pairs for which s was calculated. The lines were calculated by interpolating this randomly scattered data. It can be seen that s depends more strongly on ε than ς, and that $\partial s / \partial \varsigma$ is negative and increases in magnitude as ε increases.

[3]Lliboutry (1993) uses the symbol V for the sliding function.

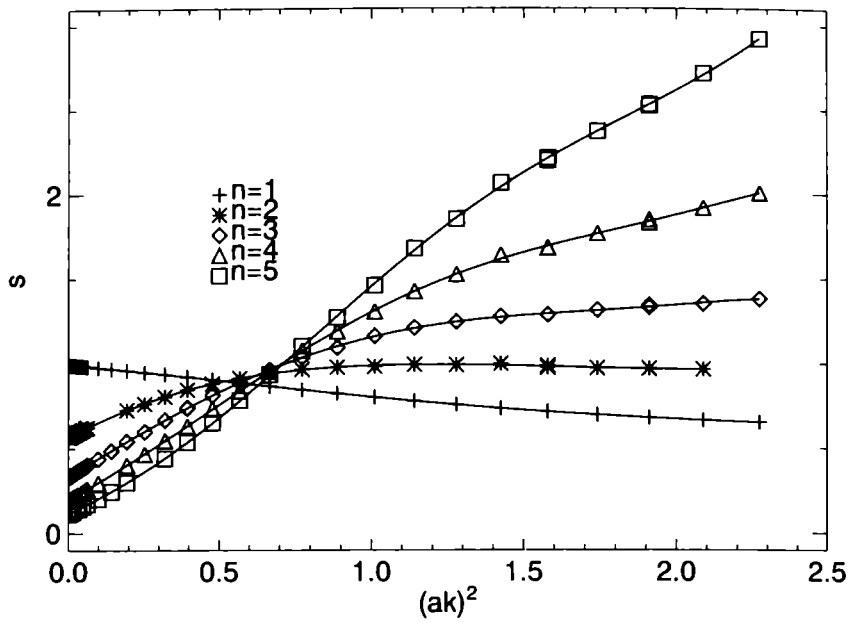

Fig. 6.4: s as a function of ε^2 for $\delta = 0.05/2\pi$ and $\varepsilon < \pi/2$ ($\dot{r} < 0.25$). The symbols represent calculated values and the lines are least squares approximations using $s(\varepsilon, \delta, n) = \sum_{i=0}^{6} c_{2i}(\delta, n)\, \varepsilon^{2i}$. Table 6.1 gives the values for c_{2i}.

n	1	2	3	4	5
c_0	0.9936	0.5661	0.3294	0.1943	0.1153
c_2	-0.1486	0.9328	1.163	1.055	0.8701
c_4	-0.1137	-0.4997	-0.3795	0.06465	0.2984
c_6	0.08996	-0.3361	0.3066	0.4760	0.8857
c_8	-0.01813	0.5192	-0.4693	-0.7965	-1.034
c_{10}	-0.001253	-0.2334	0.2459	0.3642	0.3583
c_{12}	0.0006450	0.03723	-0.04077	-0.05325	-0.0380
st. dev.	3.5×10^{-5}	0.0028	0.0027	0.0067	0.0074

Table 6.1: Taylor coefficients of the sliding function $s(\varepsilon, \delta, n) = \sum_{i=0}^{\infty} c_{2i}(\delta, n)\, \varepsilon^{2i}$ for $\delta = 0.05/2\pi$. These values can be used for $\delta = 0$ with less than 2% error.

n	a_n	b_n	standard deviation
1	-1.159	-2.002	0.00071
2	-1.671	-2.987	0.0017
3	-2.174	-3.976	0.0032
4	-2.653	-4.962	0.0047
5	-3.110	-5.943	0.0060

Table 6.2: Linear regression coefficients for $\ln U_b(\varepsilon, 0.05/2\pi, n) = a_n + b_n n$ for $\varepsilon < 0.125$. Theory predicts $b_n = -(n+1)$ for $\varepsilon \to 0$.

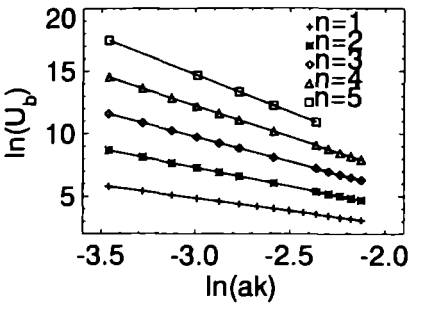

Fig. 6.5-a: $\ln U_b$ as a function of ε and n for $\varsigma = 0.05$ and $\varepsilon < 0.125$.
The straight lines show the best linear approximations through calculated values given by the symbols.

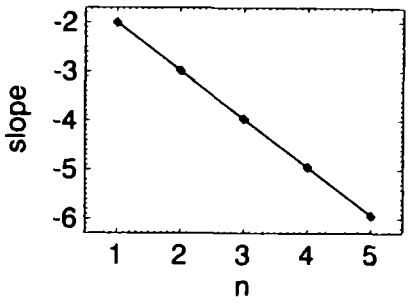

Fig. 6.5-b: U_b as a function of n for $\varsigma = 0.05$ and $\varepsilon < 0.125$.
Each point represents the slope of a curve in Fig. 6.5-a for the corresponding n. The best straight-line approximation is given by $-1.017 - 0.986n$ with a standard deviation of 0.0025, in an agreement with the theoretical prediction of $-(1+n)$ for the slopes

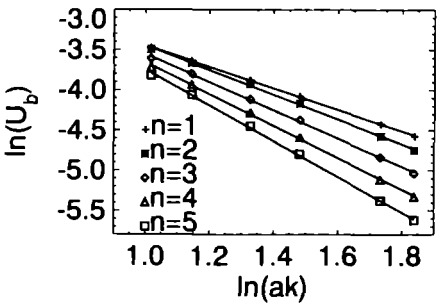

Fig. 6.5-c: $\ln U_b$ as a function of ε and n for $\varsigma = 0.05$ and $\varepsilon > 2.7$.
The straight lines show the best linear approximations though calculated values given by the symbols.

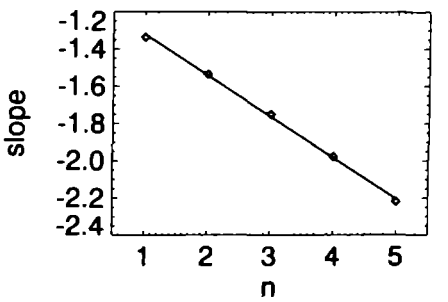

Fig. 6.5-d: U_b as a function of n for $\varepsilon > 2.7$
Each point represents the slope of a curve in Fig. 6.5-c for the corresponding n. The best straight line approximation is given by $-1.11 - 0.228n$ with a standard deviation of 0.010. No theoretical prediction known.

The sensitivity of the sliding velocity to changes in glacier thickness is therefore larger for high corrugation values than for small ones.

6.6.2 The dependency of u_b on δ

The contour lines in Fig. 6.6 are more or less straight lines (deviation from straight lines could be a result of the interpolation procedure) and this fact indicates that s is possibly a linear function of δ. By plotting s as a function of ς for different values of n and ε, as done in Fig. 6.7, it is found that s is indeed a linear function of ς and that the slope increases with increasing ε and, more importantly, with increasing n.

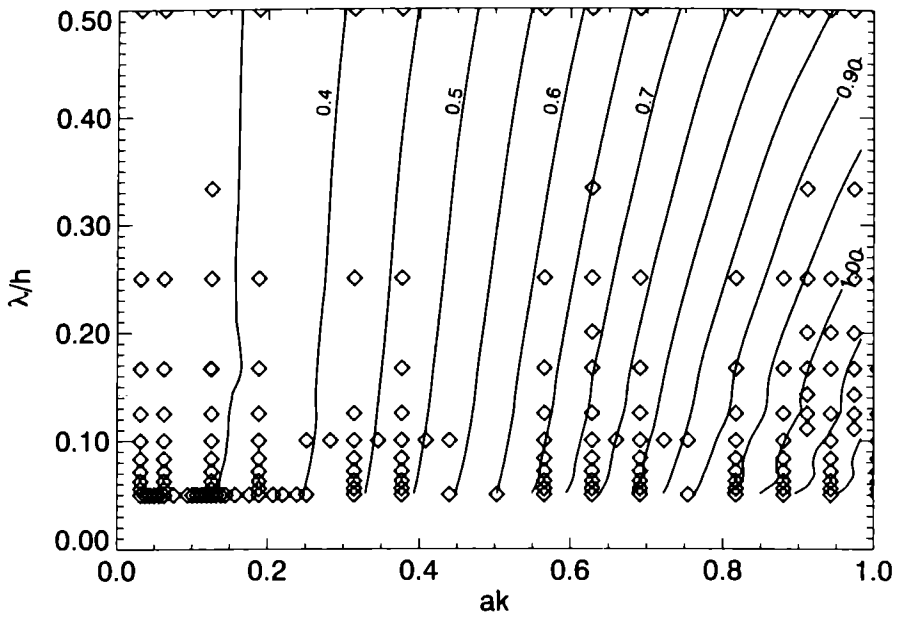

Fig. 6.6: Dependency of s on ε and ς for $n = 3$. Contour interval is 0.05. Diamond symbols represent the (ε, ς) pairs for which s was calculated. It can clearly be seen that s depends more strongly on ε than ς, and that $\partial s/\partial \varsigma$ is negative and increases in magnitude as ε increases. As explained in the text, a closer inspection of the numerical results showed that the sliding function s depends linearly on δ. The contour lines should therefore be straight lines, and the deviation from that form results from errors associated with the interpolation.

Hence, the sensitivity of the sliding velocity to changes in glacier thickness increases with increasing n. Except for $n = 1$, s is a decreasing function of δ and u_b therefore decreases somewhat faster than τ_b^n.

For $r = 0.02$, s changes less than 6% for $0 \leq \varsigma \leq 1$ even for $n = 5$. For $\varsigma \not\ll 1$ the variation of the sliding velocity is expected to set up some surface variation that in turn will change the stress pattern at the bottom resulting in a different sliding velocity. $\varsigma \ll 1$ can therefore be seen as a part of the definition of the problem and not a simplifying assumption. If $\varsigma \ll 1$ is not fulfilled the notation of sliding velocity is not clear. For reasonable ς values ($\varsigma \leq 1/4$) ς does not influence the sliding velocity significantly unless $n \geq 3$ and $r \geq 0.1$. As an example, for $n = 5$ and $r = 0.2$, s changes $\approx 20\%$ as ς goes from zero to 0.25. This is unexpectedly large, and it is important to get some rough idea of what is causing this ς-dependency.

The following simple explanation turns out to be helpful. For $\varepsilon \ll 1$ the contributions of the crest ($0 \leq X < \pi$) and the trough ($\pi \leq X < 2\pi$) of the sine wave to the average shear stress are equal. As ε increases this is no longer true as higher harmonics that disturb this symmetry start to be important. The stresses become more and more concentrated about the crest meaning that the force balancing gravity is increasingly supported by it. The glacier thickness, as well as the driving force, are therefore effectively reduced. Let us assume that the driving stress is given by

$$\hat{\tau}_b = \rho g(h - p(x)a)\sin\alpha \tag{6.13}$$

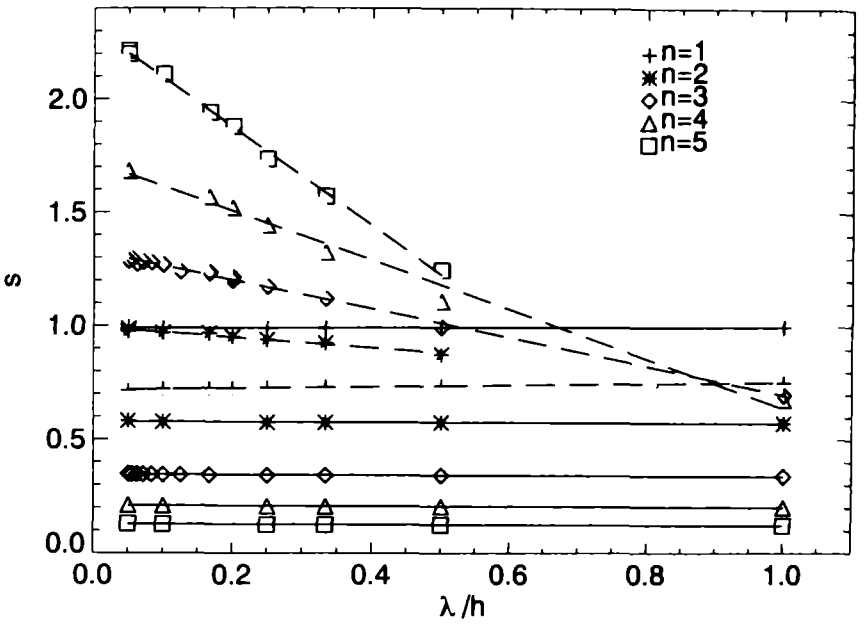

Fig. 6.7: s as a function of ς for $r = 0.02$ (solid lines) and $r = 0.2$ (long dashes). The numerical results indicate that the sliding function s depends linearly on the λ/h ratio (asperity). The slope of the $s(\varsigma)$ curve depends on n and ε, and it can be shown that this dependency is approximately linear, and that $s(\varepsilon, \delta, n) \approx (1 - \varepsilon\delta n)s(\varepsilon, 0, n)$, for $\varepsilon\delta \ll 1$.

with $0 \leq p(n) \leq 1$, where $p(x)$ is otherwise an unknown function, which depends on n because the shift in stress pattern and the degree of stress concentration is expected to depend on n. If the only influence of a change in a is given by this reduction in driving stress then it follows that

$$\begin{aligned} s(\varepsilon, \varsigma, n)/s(\varepsilon, 0, n) &= (\hat{\tau}_b/\tau_b)^n \\ &= (1 - \varepsilon\delta p(n))^n \\ &\overset{\varepsilon\delta \ll 1}{=} (1 - \varepsilon\delta n p(n)) \end{aligned} \tag{6.14}$$

The slope of the $s(\delta)$ graph should therefore be proportional to ε and $nr(n)$. The ratio $s/(1 - \varepsilon\delta)^n$ as a function of ς is seen in Fig. 6.8. Comparison with Fig. 6.7 shows that the slopes are greatly reduced, meaning that the most part of the δ dependence can be explained in this way with $p(n) = 1$. The systematic change of $s/(1 - \varepsilon\delta)^n$ as a function of the asperity ς is (for a reasonable range of ς) so small that it is of no practical importance. The curves, however, seem to be somewhat over-corrected for small n values, and under-corrected for large ones. This would mean that $p(n)$ increases with n or that the stress concentration becomes larger for increasing n. An inspection of the numerical results showed this to be true.

Of interest is the sliding velocity as a fraction of the total surface velocity. If one writes the surface velocity u_s as a sum of the deformation velocity u_d and the sliding

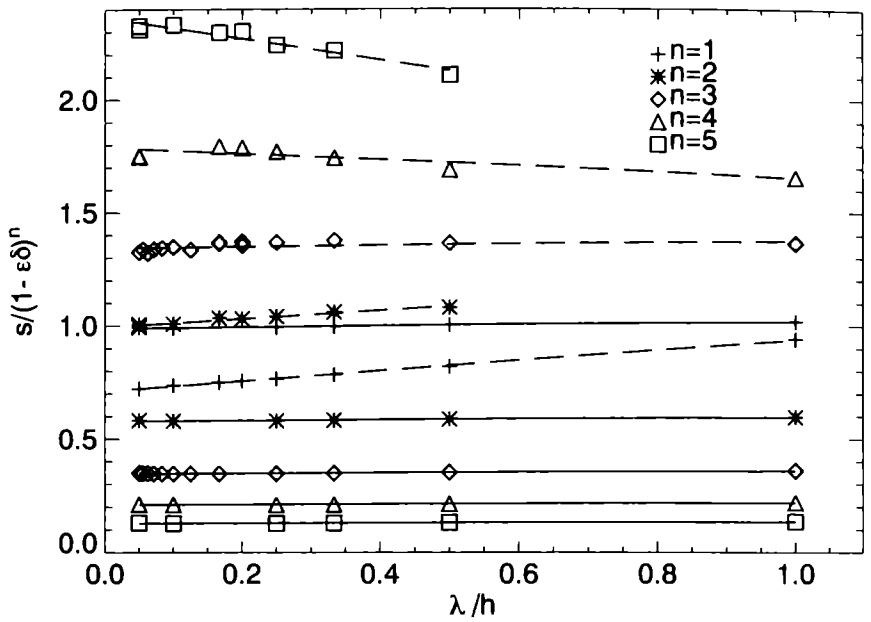

Fig. 6.8: $s/(1-\varepsilon\delta)^n$ as a function of ς for $r = 0.02$ (solid lines) and $r = 0.2$ (long dashes). By comparing this figure with the previous one it can be seen how much of the dependency of s on δ can be accounted for by the assumption $s(\varepsilon, \delta, n) = (1-\varepsilon\delta)^n s(\varepsilon, 0, n)$.

velocity[4]

$$u_s = 2A\ \tau_b^n \left(\frac{h}{n+1} + \frac{s}{\varepsilon^{n+1} k} \right) \tag{6.15}$$

one finds

$$\Delta_b := \frac{u_b}{u_s} = \left(1 + \frac{\varepsilon^{n+1}}{(n+1)\delta s} \right)^{-1} . \tag{6.16}$$

The ratio that determines the *fractional sliding velocity* (Δ_b) is therefore:

$$\frac{\varepsilon^{n+1}}{(n+1)\delta s}, \tag{6.17}$$

and Δ_b can be quite large. For $r = 0.1$, $\varsigma = 0.05$ and $n = 3$ one finds for example, using the values from Table 6.1, that $\Delta_b = 0.58$. Using $r = 0.05$ gives $\Delta_b = 0.99$. Sliding over a hard bed without bed separation can be significant. It is important to realize that Eq. (6.16) gives the maximum fractional sliding possible. In nature ice will always experience some friction from the bed reducing the sliding velocity (possibly down to zero).

Eq. (6.16) shows that $\partial\Delta_b/\partial\delta$ depends on ε. Observation of changes in fractional sliding velocity as a glacier changes its thickness could therefore give information on the roughness of the glacier bed.

[4]This is only approximately correct. For $n \neq 1$ the ice close to the bedrock becomes somewhat softer and the internal deformation therefore somewhat larger than otherwise expected.

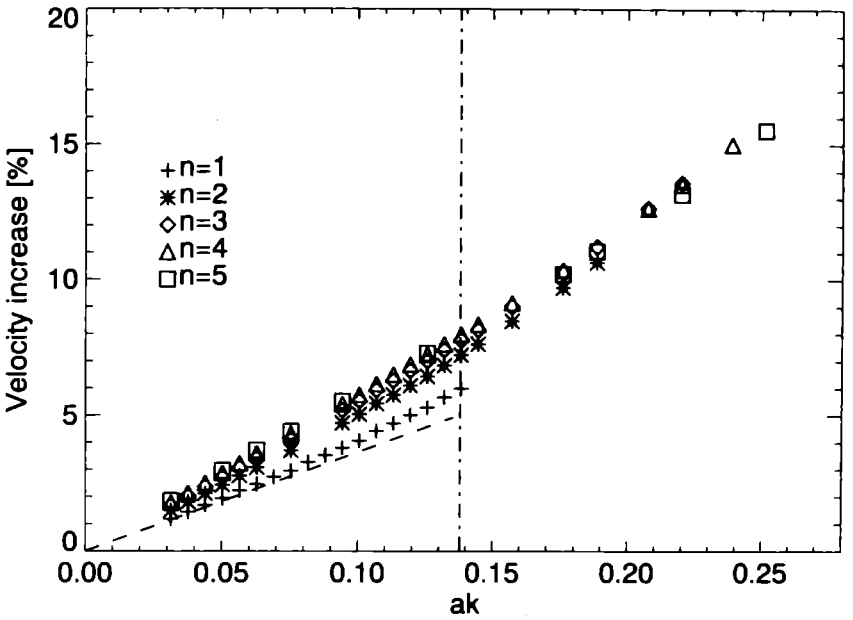

Fig. 6.9: The velocity increase of $U_{\pi/2}^{\max}$ with respect to the velocity at bed at $X = \pi/2$, for $\varsigma = 0.05$. With increasing ε, $U_{\pi/2}^{\max}$ moves towards $U_{\pi/2}^{\text{saddle}}$ and disappears at $\varepsilon = \varepsilon_{\text{critical}}$. For $n = 1$ and $\delta \ll 1$ this limiting value is approximately equal to 0.138. The vertical dashed-dotted line marks this ε value. For $n = 1$ there should therefore theoretically be no symbols to the right of the line. The numerical calculations confirm this. The value of ε above which no local velocity maximum was found depends on n. This is reflected in the figure by the fact that symbols are found at progressively larger ε values with increasing n, showing that the magnitude of the velocity maximum is both enhanced by the non-linearity of the flow law and that it exists up to larger roughnesses.

6.6.3 Extrusion flow and non-linear material behavior

As explained in Sec. 4.3 extrusion flow is expected to occur above the point where $U_{\pi/2}^{\max}$ for $n = 1$ arises, as long as $\varepsilon < 0.1378839$, and below the point where $U_{3\pi/2}^{\min}$ arises as long as $\varepsilon < 1/2$. Extrusion flow is caused by the bedrock undulations and can therefore be seen as a geometrical effect. The flow law can, however, be expected to have an influence on the magnitude and the onset of extrusion flow.

In Fig. 6.9 the percentage of increase of the velocity $U_{\pi/2}^{\max}$ over the velocity at $Z_0(\pi/2)$ as a function of ε is shown for $n = 1$ to $n = 5$. The vertical dashes-dotted line is at $\varepsilon = 0.1378839$. To the right of that line no plus symbols are shown, indicating that in agreement with the theoretical prediction for $n = 1$ no $U_{\pi/2}^{\max}$-points were found for larger ε values. The long dashes show the theoretical asymptotic slope for $\varepsilon \to 0$. Again a good agreement between numerical and analytical results is found.

For $n > 1$ extrusion flow exists. As n increases the range of ε values for which extrusion flow is found becomes progressively larger. The velocities also become progressively larger. Extrusion flow is therefore enhanced by the non-linearity of Glen's flow law. For $n = 3$ it is for example found for ε up to ≈ 0.2 or $r \approx 0.03$, and the velocity is $\approx 10\%$ larger than at the bed. The position of $U_{\pi/2}^{\max}$ for $n = 1$ follows

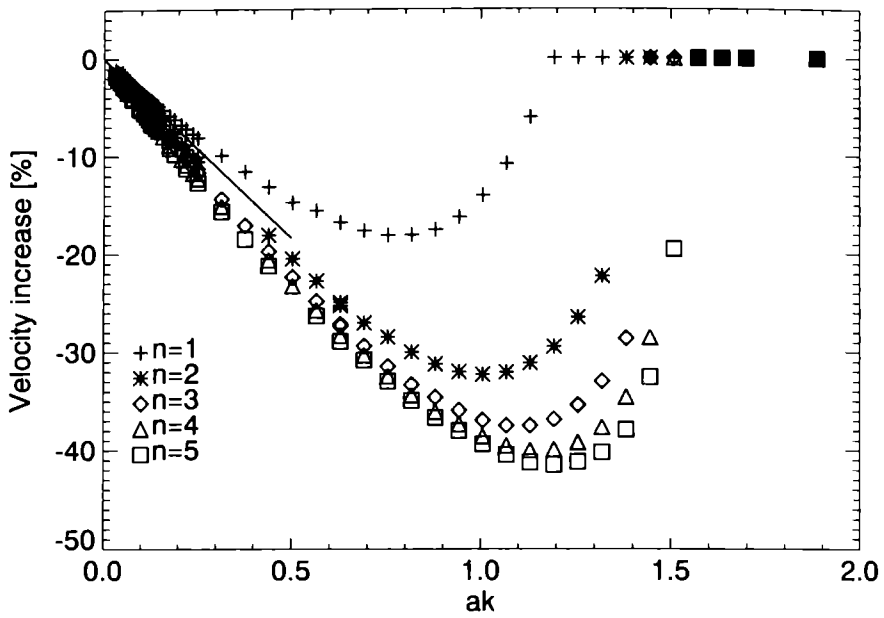

Fig. 6.10: Relative decrease of $U^{\min}_{3\pi/2}$ with respect to the velocity at the bed at $X = 3\pi/2$ for $\varsigma = 0.05$. For $\varepsilon \to 0$ there is no velocity variation and the velocity of the local velocity minimum is the same as the velocity at bed. Thus for $\varepsilon \to 0$ all the curves approach the value 0. For $\varepsilon > 0$ the minimum velocity is always less than the velocity at the bed (extrusion flow) so that the percentage increase is always negative. With increasing ε, $U^{\min}_{3\pi/2}$ becomes, as a percentage of the bed velocity, larger negative, and at some particular value of ε a minimum is reached. The position of this minimum moves to larger ε values with increasing n. The velocity minimum is also stronger for larger n values (larger negative numbers). The non-linearity of the flow law therefore has the effect of enhancing the vertical velocity variation in relative terms, and with it the extrusion flow behavior. On the basis of Morland's solution it was expected that for a linear medium no velocity minimum would be found for $\varepsilon > 1/2$. The results of the numerical calculations do not, as can be seen in the figure, support this conclusion. $U^{\min}_{3\pi/2}$ for $n = 1$ is found up to $\varepsilon \approx 1.18$. The reason for this discrepancy lies presumably in the fact that $1/2 \not\ll 1$, and that therefore the results of the second order perturbation theory, were $\varepsilon \ll 1$ is assumed, cannot be trusted.

closely the theoretical prediction. For $n > 1$ the $U^{\max}_{\pi/2}$ moves progressively closer to bed. This is in agreement with other numerical calculations (Raymond, 1978).

Fig. 6.10 shows the minimum of the absolute horizontal velocity at $X = 3\pi/2$ as a percentage of the velocity at the bed *i.e.*

$$100\left(\frac{\min_z(|v_x(3\pi/2, z)|)}{v_x(3\pi/2, -a)} - 1\right) \tag{6.18}$$

for $\varsigma = 0.05$ as a function of ε. The theoretical prediction for $n = 1$ was that $U^{\min}_{3\pi/2}$ should exist for $\varepsilon < 1/2$. Symbols below the horizontal zero line indicate that a minimum was found. For $n = 1$ a minimum was found for ε up to 1.17 and not only up to $\varepsilon = 1/2$. The theoretical value is based on a perturbation analysis which is only valid for $\varepsilon \ll 1$. Since $U^{\min}_{3\pi/2}$ exists for $\varepsilon > 1$ it is clear that the perturbation approach could never have given the correct answer. The asymptotic change of the

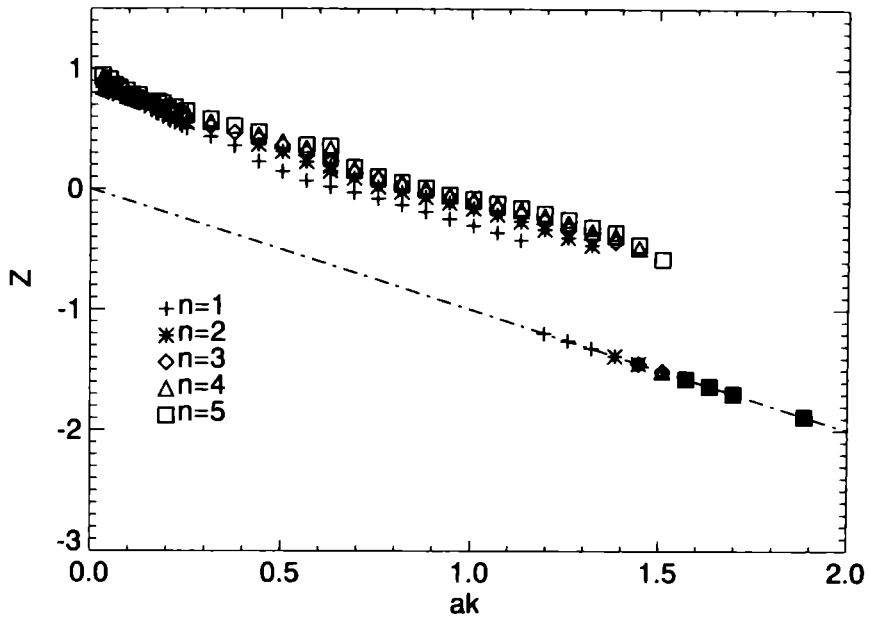

Fig. 6.11: Vertical position of $U^{\min}_{3\pi/2}$ ($\varsigma = 0.05$). The numbers on the y-axis correspond to a vertical distance of $1/k$. For $\varepsilon \to 0$, $U^{\min}_{3\pi/2}$ is situated at $Z = 1$, or $z = 1/k$. If the minimum velocity at $kx = 3\pi/2$ is found at $z = -a$, $U^{\min}_{3\pi/2}$ is at the bed. This corresponds to $kz = -ka$ or $Z = -\varepsilon$. The line made of points and long dashes gives the position of the bed as a function of ε. If the symbols lie on the line there is no local velocity minimum above the trough of the sine curve. Note that with increasing n, $U^{\min}_{3\pi/2}$ moves away from the bed-line.

velocity decrease as $\varepsilon \to 0$, shown as a solid line, is however reproduced. There is therefore a good agreement between theory and numerics at ε values where an agreement can be expected. Notice that the two figures are practically identical indicating that the exact value of ς is unimportant as long as it is small. This is also correct for others figures shown below.

For all calculated values of n the velocity decrease (shown in the figures as a negative velocity increase) becomes larger as ε increases from zero, reaches a maximum and decreases again. There is always some ε value above which no extrusion flow is found. As n increases the extrusion flow is strongly enhanced. It again becomes progressively larger in magnitude and exists for larger ε values as n increases. Comparison of Figs. 6.10 with Fig. 6.9 shows that extrusion flow behavior is more dominant above a trough than above a riegel. Above a trough a 30 to 40 % decrease in horizontal velocity with height over a distance of $\approx 1/k$ is possible and could for example cause a considerable inversion of a bore-hole inclination.

$U^{\min}_{3\pi/2}$ arises for $\varepsilon = 0$ at $Z = 1$ and moves towards the bed with increasing ε. How this happens for $n = 1$ to $n = 5$ and $\varsigma = 0.05$ can be seen in Fig. 6.11. The dashed-dotted line gives $Z = -\varepsilon$, which is the position of the bed. As long as the symbols remain above the dashed-dotted line $U^{\min}_{3\pi/2}$ exists. It is interesting that $U^{\min}_{3\pi/2}$ is situated slightly larger above the bed for larger n values which is opposite to the behavior of $U^{\max}_{\pi/2}$. It is therefore not a general rule that characteristics of the ice deformation tend to approach the bed with increasing n. Another interesting feature

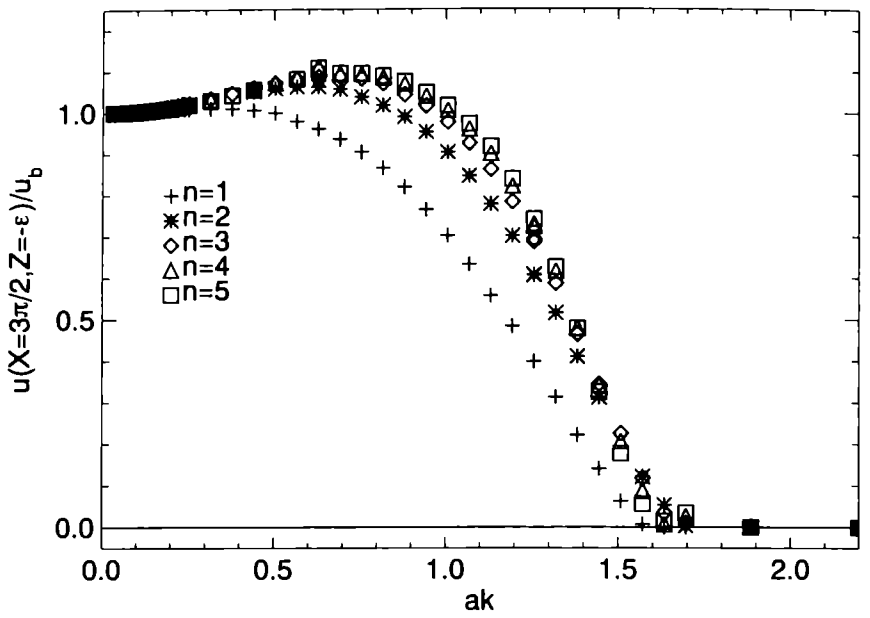

Fig. 6.12: Velocity at $(X, Z) = (3\pi/2, -\varepsilon)$ as a fraction of the sliding velocity ($\varsigma = 0.05$). Note that the velocity at the base of the trough at first increases with ε, and that the non-linearity of the flow law makes this increase larger and displaces it to larger ε values .

of the figure is that $U^{\min}_{3\pi/2}$ remains more or less at a constant height of approximately 1 (or at $\lambda/2\pi$ in dimensional units) above the bed for all values of ε.

The velocity within an overdeepening as a fraction of the sliding velocity is often of interest. It is for example sometimes important to know at what roughness values the ice within the overdeepening effectively remains there without taking part in the overall glacier motion. What exactly is meant by saying that the ice does not move depends of course on what part of the overdeepening — at the bed or only "close" to the bed — one is referring to, but it turns out that this is, at least for the case of a perfectly lubricated bed, relatively unimportant, as will be shown below.

The velocity at $(X, Z) = (3\pi/2, -\varepsilon)$ as a fraction of the sliding velocity (*cf.* Fig. 6.12) becomes, as ε increases from zero, at the beginning somewhat larger. This unexpected result is a manifestation of the extrusion flow and is more important for non-linear than for linear flow behavior. As ε increases further the ratio $v(X = 3\pi/2, Z = -\varepsilon)/u_b$ decreases fast; it is less than 0.1 at $\varepsilon = 1.6$ and negligibly small for $\varepsilon > 2$.

Another measure of the magnitude of ice movements within a trough would be the velocity at the base of the trough ($(X, Z) = (3\pi/2, -\varepsilon)$), or the minimum velocity at $X = 3\pi/2$ for some Z, normalized by the velocity at the top of the riegel ($(X, Z) = (\pi/2, \varepsilon)$), which is depicted in Fig. 6.13 and Fig. 6.14 respectively. In all cases the result is effectively the same. For $\varepsilon \geq 2$ there is practically no ice movement within the trough.

A value of $\varepsilon = 2$ corresponds to $r = 1/\pi \approx 0.32$ which can hardly be considered to be a very high roughness value. For an overdeepening or a trough having this value

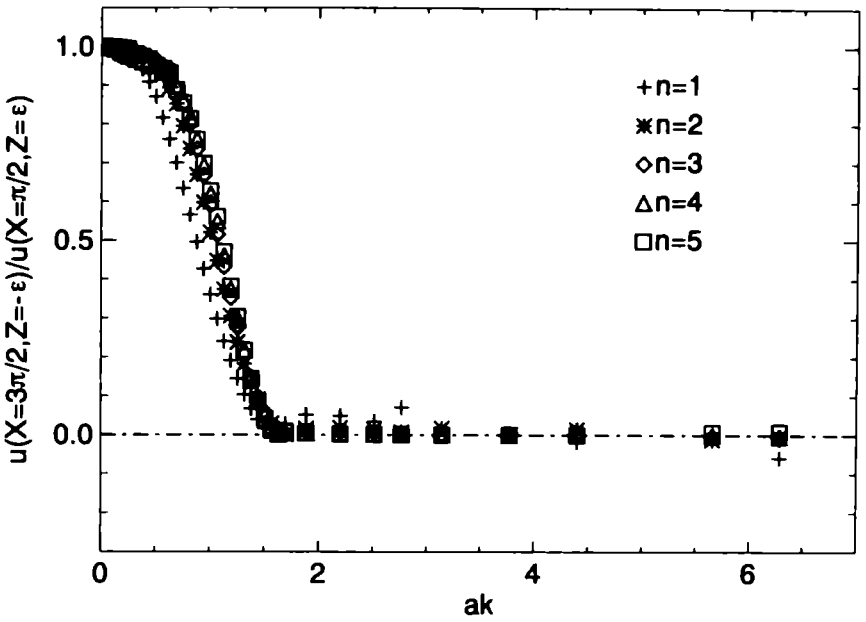

Fig. 6.13: $u(X = 3\pi/2, Z = -\varepsilon)$ normalized by $u(X = \pi/2, Z = \varepsilon)$ for $\varsigma = 0.05$. The curve gives the velocity at the base of the trough as a fraction of the velocity at the peak of the sine curve.

of roughness or larger the ice within it practically does not move. Perfect sliding is an idealization, which will cause the maximum local basal velocity possible. Any degree of friction will presumably pose a further hindrance to ice movements.

The minimum velocity at $X = 3\pi/2$ normalized by u_b is shown in Fig. 6.15. For ε large enough to exclude extrusion flow the minimum is found at the bed ($Z = -\varepsilon$), and Fig. 6.15 shows a similar behavior Figs. 6.12 and 6.14. But there is also something quite unexpected to be seen; for $\varepsilon > 1.8$ $u(X = 3\pi/2, Z = -\varepsilon)/u_b$ is negative, *i.e.* the medium in the lowest part of the trough flows in the opposite direction to the main flow. This is a clear indication of a flow separation.

An example of a flow separation is given in Fig. 6.17. It is an enlarged part of Fig. 6.16, which shows the flow above and within an overdeepening for $\lambda = 50\,\mathrm{m}$, $a = 20\,\mathrm{m}$, $h = 200\,\mathrm{m}$, $n = 1$ and $\rho g \sin\alpha = 8.99577 \times 10^{-3}\,\mathrm{bar/m}$. Fig. 6.16 again only shows a part of the hole configuration, which had the dimensions $200 \times 200\,\mathrm{m}$. The velocities have the dimension m/a. Although the velocities within the overdeepening are small compared to the velocity at the riegel, they are a significant fraction of the sliding velocity, which for this particular case is 0.50 m/a. It can clearly be seen how the main flow induces a secondary flow circulation in the clockwise direction. a separation line is formed (shown as long dashes), separating the main flow from the induced flow. The ice below the separation line will theoretically circulate there for ever, never leaving the trough.

Flow separation is not, as sometimes thought, limited to high Reynolds numbers as Figs. 6.17 and 6.16 clearly show. There is also a number of analytical and experimental studies of creeping flow that show that flow separation is not limited to the

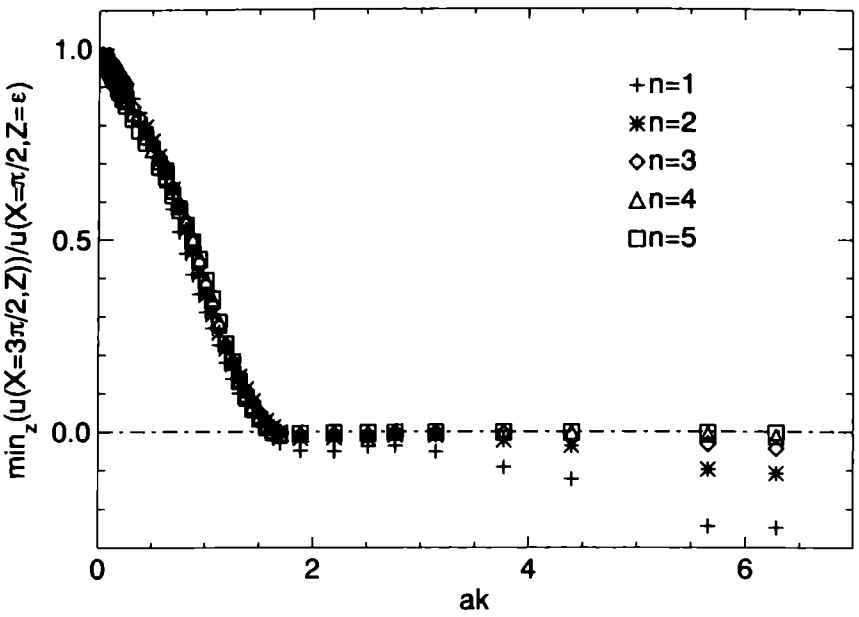

Fig. 6.14: The minimum of the horizontal velocity v_x at $X = 3\pi/2$ for some z normalized by the velocity at the peak of the sine curve, i.e. $\min_Z(u(X = 3\pi/2, Z))/u(X = \pi/2, Z = \varepsilon)$. The minimum is not necessarily found at the base of the trough. The negative numbers indicate that the minimum velocities are negative, i.e. the flow direction is opposite to the flow direction at $(X, Z) = (\pi/2, \varepsilon)$. This is an example of the recirculation of the ice within the trough which takes place at high ε values.

particular case of a perfectly lubricated sinusoidal bed (Hasimoto and Sano, 1980; Sherman, 1990, p. 258 - 265). Corner flow, as an example, driven by circumferential motion with no-slip boundary conditions, is known to form so called Moffatt corner eddies[5] if the corner is sharp enough (Moffatt, 1964). The corner angle must be less than 73°. A review of the literature has, however, not revealed any other examples of flow separation for perfectly-sliding-type boundary conditions. Separation is also known to occur in creeping flow past sharp-cornered obstacles such as a vertical fence of in a plane flow past a step (Taneda, 1956).

Tsangaris and Potamitis (1985) did numerical calculations on laminar small Reynolds-number flow over a sinusoidal wall using no-slip boundary conditions. They found flow separation at $\varepsilon \approx 0.6$ for $\mathrm{Re} = 1$, where the Reynolds number Re was defined by $\mathrm{Re} = U\lambda/(2\eta)$, where U was the horizontal velocity at large distance above the wall.

The magnitude of the reversed flow can be several times as large as the sliding velocity (*cf.* Fig. 6.15), but enlarging n decreases it. To test the influence of the FE grid size on the onset of flow separation a local mesh refinement was done that made the mesh unsymmetrical with respect to $X = 3\pi/2$. It was found that this did locally increase the reverse flow. The possibility that extrusion flow occurs somewhat earlier than Fig. 6.15 indicates and that its magnitude is somewhat greater cannot

[5]Named after H. K. Moffatt, who theoretically proved their existence

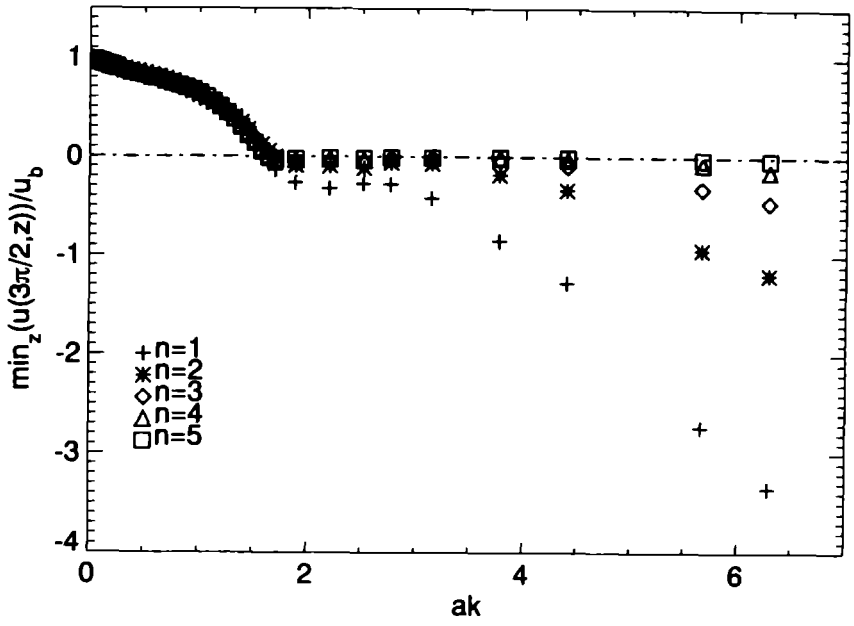

Fig. 6.15: The minimum of the horizontal velocity above the trough of the sine wave as a function of ε ($\varepsilon := ak$), i.e. $\min_Z(u(3\pi/2, Z))$. The velocities were normalized by the average sliding velocity u_b. For $\varepsilon \to 0$ there will be no velocity variations and the minimum of v_x is equal to u_b. Therefore all the velocity curves start at 1.0 for $\varepsilon = 0$. With increasing roughness the minimum of the horizontal velocity as a fraction of the sliding velocity becomes smaller. For $\varepsilon = 1.75$ the minimum of flow velocities within the trough have become a negligible fraction of the sliding velocity. As ε increases further negative values are found. This shows that the minimum velocities have become negative. Since the roughness is then quite large the sliding velocities are small and the ratio of the minimum velocities (maximum negative velocities) to u_b can thus be large.

be excluded. This is especially true for $n > 1$.

6.6.4 Frequency doubling

That larger frequencies become increasingly important can clearly be seen in Fig. 6.18 and 6.19 that show the first four harmonics of the basal velocity for $n = 1$ and $n = 3$. The figures are double logarithmic and the Fourier coefficients have been normalized by u_b. The solid line gives the increase of the second harmonics according to Eq. (4.8).

For $n = 1$ (Fig. 6.18) and ε small, the first two harmonics are about equally important. But as ε increases and the stresses concentrate about the peaks of the sine curve the amplitude of the other two harmonics shown become comparable with the first two ones. Within the framework of perturbation analysis each harmonic is associated with one term of the power series. The rise of the i-th harmonic with ε is therefore proportional to the i-th power of ε. This can be seen in Fig. 6.18 where the slope of the curves is equal to the number of the harmonic.

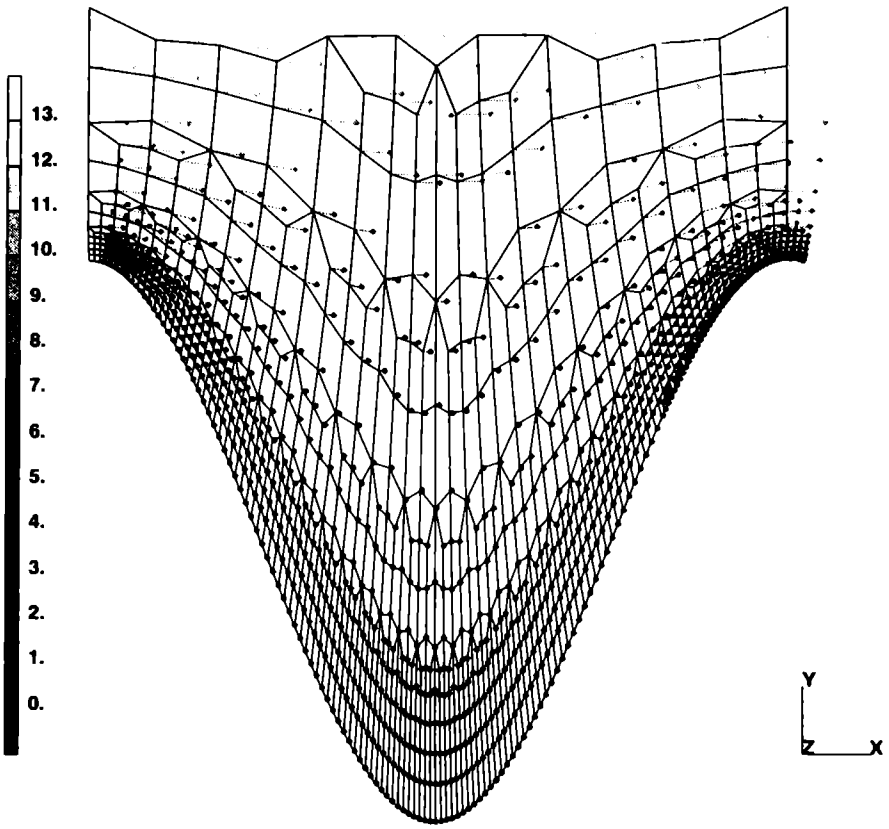

Fig. 6.16: Flow above and within an over-deepening. Parameters used: $\lambda = 50\,\mathrm{m}$, $a = 20\,\mathrm{m}$, $h = 200\,\mathrm{m}$, $n = 1$ and $\rho g \sin\alpha = 8.99577 \times 10^{-3}\,\mathrm{bar/m}$. The velocities have the dimension m/a. Only a part of the FE model is shown.

For $n = 3$ the higher harmonics turn out to be relatively more important with respect to the first harmonic than for $n = 1$. Frequency doubling seems to play a more important role for non-linear flow. This can be understood as a result of the flow becoming more concentrated about the peaks for $n > 1$.

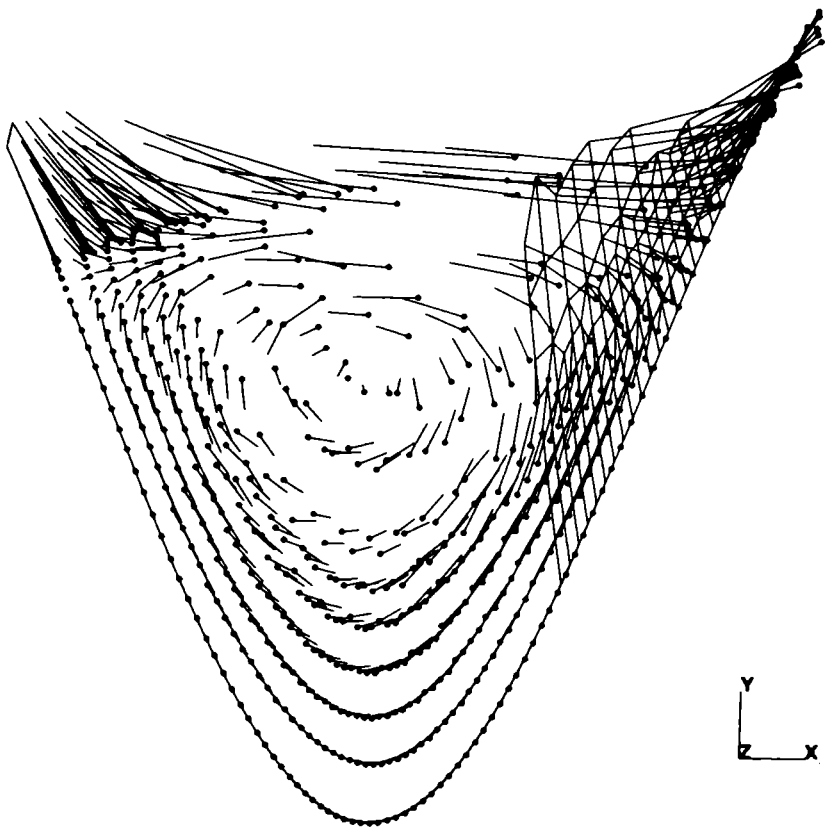

Fig. 6.17: Flow separation. Same parameters used as in the previous figure. Only part of the FE mesh is shown. The direction of the main flow is from left to right. The vectors indicate the direction of the flow at each FE node. The ice within the trough rotates slowly in the clockwise direction. The ice which takes part in this circular motion will theoretically never leave the trough, and is thus separated from the main flow. This calculation was done for a perfectly lubricated bed. No systematic study was made of the effect of the boundary condition along the bed-line on the flow behavior. This particular calculation was, however, repeated for no-slip boundary conditions, and again a flow separation of this type was found.

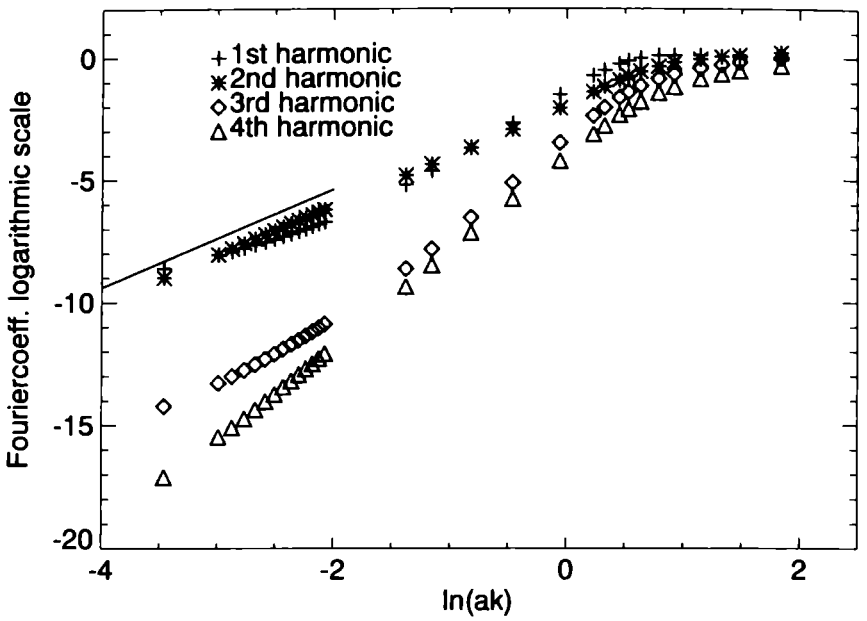

Fig. 6.18: Harmonics of the basal velocity for $n = 1$ ($\varsigma = 0.05$). The Fourier coefficients were normalized by the sliding velocity u_b. The solid line gives the theoretically-derived curve for the second harmonics. The curve is double logarithmic. Note how important the second harmonics are. With increasing ε all harmonics become equally important.

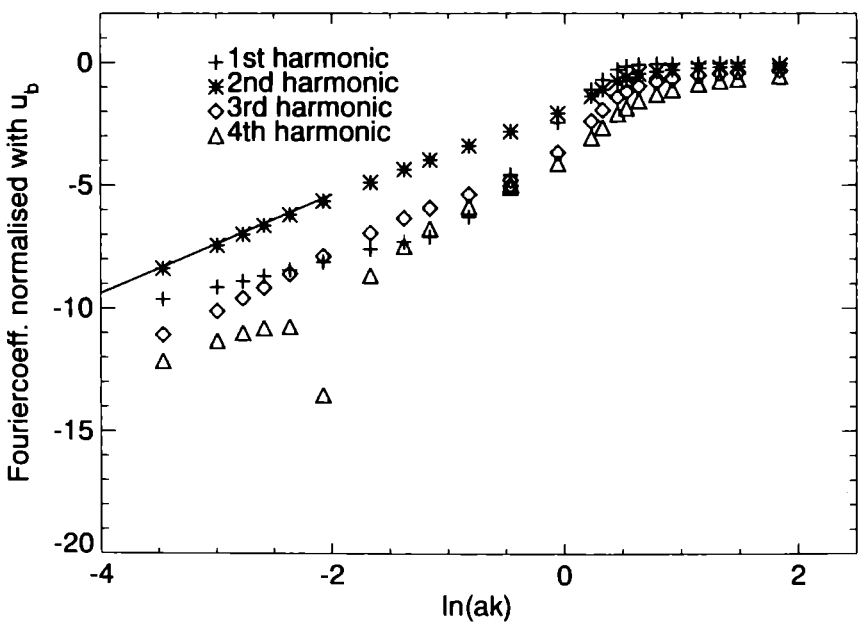

Fig. 6.19: Harmonics for $n = 3$ ($\varsigma = 0.05$) normalized by u_b. The solid line gives the theoretically-derived curve for the second harmonics for $n = 1$. The curve is double logarithmic.

CHAPTER 7

Conclusions

With the use of both analytical and numerical methods the flow characteristics as well as the sliding velocity of a highly viscous medium flowing under the influence of gravity over a perfectly lubricated sinusoidal bed have been analysed. In this chapter a summary of results, and recommendations for further research will be given. Examples of field observations of extrusion flow that can be understood in the light of these new findings and predictions about flow patterns of glacier in the Alps that could not have been done before this investigation was made, will be given.

7.1 Flow characteristics

The horizontal velocity field of a highly viscous medium flowing over a frictionless sinusoidal bed can have a point of local velocity maximum $U_{\pi/2}^{\max}$ above the peak of the sine curve, and a point of local velocity minimum above the trough of the sine curve. Whether these stationary points will exist or not depends mainly on the roughness of the bed ($r := a/\lambda$ or $\varepsilon := ak$), and the non-linearity of the medium, but also to some extent on the wavelength to thickness ratio.

7.1.1 The local velocity maximum, $U_{\pi/2}^{\max}$

The velocity maximum is found for $\varepsilon \leq \varepsilon_{\text{critical}}(\pi/2, \delta)$. $\varepsilon_{\text{critical}}$ is a function of n and is listed in Table 7.1 for $n = 1$ to $n = 5$ for $\delta \ll 1$. The value of $\varepsilon_{\text{critical}}$ increases with increasing n showing that the non-linearity of the flow law makes the range of ε values for which $U_{\pi/2}^{\max}$ exists larger.

$U_{\pi/2}^{\max}$ is situated directly above the peak of the sine curve. For $\varepsilon = 0$ its vertical position is given by $Z = 1$. With increasing ε, $U_{\pi/2}^{\max}$ moves upwards with respect to the mean bed-line. For $n = 1$ and $\varepsilon = \varepsilon_{\text{critical}}$, $U_{\pi/2}^{\max}$ is at $Z \approx 1.98$. Increasing the value of n moves $U_{\pi/2}^{\max}$ towards the bed.

There is a point of the horizontal velocity field situated directly above $U_{\pi/2}^{\max}$ were v_x has a local maximum in the horizontal direction but a local minimum in the vertical direction. This saddle point $U_{\pi/2}^{\text{saddle}}$ moves downwards from $Z = \infty$ towards the maximum point $U_{\pi/2}^{\max}$ with increasing ε. For $\varepsilon = \varepsilon_{\text{critical}}$ the vertical position of the saddle point and that of the maximum point become coincident. For $\varepsilon \geq \varepsilon_{\text{critical}}$, $U_{\pi/2}^{\max}$ and $U_{\pi/2}^{\text{saddle}}$ do not exist.

n	$\varepsilon_{\text{critical}}(\pi/2, 0)$
1	0.13788
2	0.19
3	0.22
4	0.24
5	0.25

Table 7.1: $\varepsilon_{\text{critical}}(\pi/2, 0)$ as a function of n for $\delta \ll 1$. The value of $\varepsilon_{\text{critical}}$ for $n = 1$ is based on the Morland solution. The values for $n > 1$ are based on numerical calculations. The velocity maximum above the peak of the sine curve ($kx = \pi/2$) exists for $\varepsilon < \varepsilon_{\text{critical}}$. The errors in the determination of $\varepsilon_{\text{critical}}$ are estimated to be less than 7%.

Between $U_{\pi/2}^{\text{saddle}}$ and $U_{\pi/2}^{\text{max}}$ the horizontal velocity increases with depth. This is an example of extrusion flow. Extrusion flow would cause an inversion of the inclination of bore holes. It is interesting that this type of inclination inversion has been observed in nature. Inclinometry measurements in a bore hole slightly down-glacier from the crest of a riegel on Storglaciären, Sweden, showed an increase in horizontal velocity with depth (Hooke *et al.*, 1987). This was only observed during summer when water pressures were high. There are indications that the ice became at least partly decoupled from the bed during this period. The assumption of frictionless flow over the bedrock may thus be valid. A map of the bed topography obtained by radio-echo measurements (Björnsson, 1981) shows that there are two regions of overdeepening up-glacier and down-glacier from the riegel. The bed can thus be approximated by a sine curve. The wavelength is about 1000 m and the amplitude approximately 20 m which gives $\varepsilon \approx 0.12$. This ε value is less than $\varepsilon_{\text{critical}}(\pi/2, 0)$ from Table 7.1 for all values of n. The assumption of $\delta \ll 1$ is however not valid and one can therefore not expect a perfect numerical agreement. The measured vertical position of the region of increase in horizontal velocity with depth is, for example, closer to the bed than would be expected on the basis of the numerical calculations done for $\delta \ll 1$. Still, it can be concluded that the vertical extension and compression of the ice caused by the sinusoidal form of the bed is a likely explanation of the observed flow pattern.

7.1.2 The local velocity minimum, $U_{3\pi/2}^{\text{min}}$

The minimum point $U_{3\pi/2}^{\text{min}}$ is situated above the trough of the sine curve ($kx = 3\pi/2$), and is found for $\varepsilon < \varepsilon_{\text{critical}}(3\pi/2, \delta)$. The calculated values of $\varepsilon_{\text{critical}}$ for $\delta \ll 1$ are given in Table 7.2.

The non-linearity of the flow law increases the range of ε values for which $U_{3\pi/2}^{\text{min}}$ is found, as Table 7.2 shows. The velocity decrease with respect to the velocity at the bed also gets more pronounced with increasing n (*cf.* Fig. 6.10).

For $\varepsilon = 0$, $U_{3\pi/2}^{\text{min}}$ is situated at $Z = 1$. With increasing ε $U_{3\pi/2}^{\text{min}}$ moves downwards, reaches the bed and disappears for $\varepsilon = \varepsilon_{\text{critical}}(3\pi/2, \delta)$. Increasing n has the effect of moving $U_{3\pi/2}^{\text{min}}$ slightly further away from the bed.

n	$\varepsilon_{\text{critical}}(3\pi/2, 0)$
1	1.20
2	1.37
3	1.45
4	1.50
5	1.55

Table 7.2: $\varepsilon_{\text{critical}}(3\pi/2, 0)$ as a function of n for $\delta \ll 1$. All values based on numerical calculations. The velocity minimum above the trough of the sine curve ($kx = 3\pi/2$) exists for $\varepsilon < \varepsilon_{\text{critical}}$. The errors in the determination of $\varepsilon_{\text{critical}}$ are estimated to be less than 7%.

Below $U^{\min}_{3\pi/2}$ the horizontal velocities increase with depth. If the explanation for the occurrence of extrusion flow at Storglaciären is correct, one must expect two further such regions above and below the riegel. This would be an interesting test of the appropriateness of this explanation.

7.1.3 Flow separation

Flow separation occurs for $\varepsilon > 1.8$ for all values of n. It can happen for a perfectly lubricated bed as well as for no-slip boundary conditions. Based on the large number of analytical, experimental and computational demonstrations of its existence, flow separation for no-slip boundary conditions is known to be an universal feature of laminar flow in corners (Sherman, 1990, p. 265) as well as around sharp corners. It is now clear that flow separation must also be expected at roughness values larger than ≈ 0.28 for smooth perfectly lubricated beds.

A value of 1.8 for the slope parameter ε corresponds to a roughness r of 0.28. This is a high roughness value but there is an example of an overdeepening in the Alps that has an even larger roughness value. This is the spectacular overdeepening found at Konkordiaplatz, Aletschglacier, Switzerland, which is about 1000 m long and 400 m deep. Although the flow situation there is strongly three-dimensional it must be expected that the ice within this overdeepening hardly takes part in the overall flow of the glacier, if at all. The overlying ice most probably moves directly over the trough. Again this is a prediction that could be put to the test.

7.1.4 Stresses

The maximum of the effective stresses along the bed-line is found for $\varepsilon \to 0$ at the inflection points of the sinusoidal curve. With increasing ε these maximum points move towards the peaks of the sine curve, and become stronger and more localized. A first order perturbation theory gives a distribution of the effective stresses that is independent of z. For a second order theory this is no longer true.

7.2 Sliding velocity

The sliding velocity as a function of n, ε, and δ has been calculated. Eq. (3.23) is correct. For finite values of ε the sliding velocity can be determined by the use of the Taylor coefficients listed in Table 6.1.

A very interesting result is the fact that $\ln u_b$ depends linearly on n for all values of ε and δ.[1]

Furthermore the numerical calculations indicate that s depends linearly on δ. As n and ε get larger the linear slope of the $s(\delta)$ curve increases approximately according to Eq. (6.14). The sliding velocity is thus dependent on the glacier thickness and measurements of changes in sliding velocities with time for glaciers lying on hard beds could thus be caused by thickness changes.

It is, however, difficult to see how these theoretical results could be tested or even used directly to estimate sliding velocities of glaciers. The model is in this respect definitely too idealized. On the other hand it is difficult to see how progress towards a theoretically-derived sliding law can be made without knowing the sliding velocity for this idealized model. Further work along similar lines is needed.

[1] To calculate s as a function of n for a different value of n than that listed, one should use Table 6.1 to calculated the sliding function for several n values and then interpolate or extrapolate the results assuming $\ln s = \hat{a} + \hat{b}n$ for some $\hat{a}$ and $\hat{b}$.

APPENDIX A

Second-order Solutions for Perfect Sliding With Regelation

The following equations give the velocity components, the strain rates, and the pressure distribution of a highly viscous medium sliding over a sinusoidal bed in the presence of regelation. They were derived directly from Morland (1976a). Morland was mainly interested in the velocity and pressure distribution along the bed, and therefore only gave the corresponding expressions for $z = 0$.

The x axis is parallel to the mean slope of the bed making an angle α with respect to the horizontal. The coordinates of the bed as a function of x are denoted by $z_0(x)$. The bed is defined by $z_0 = a \sin kx$.

Regelation is only important at wavelengths comparable to or smaller than the *transition wavelength* λ_*, where

$$\lambda_* = \sqrt{\frac{8\pi^2 \eta C_0 (K_I + K_B)}{L}}. \tag{A.1}$$

Using the numerical values for the physical parameters from Table A.2 one finds that the transition wavelength is of the order of 0.5 m. For a non-linear medium with $n > 1$ the transition wavelength becomes smaller (Kamb, 1970; Fowler, 1979; Fowler, 1981). Table A.1 compares the notation that is used here with the notation of several other authors.

There are two parameters that describe the relative importance of regelation to viscous flow. One of them is denoted by $\bar{w}$ and is the ratio of the bed wavelength

this thesis	Nye (1969,1970)	Kamb (1970)	Lliboutry (1987b)	Morland (1976a)
k_*	k_*	l_0	w_*	$1/\bar{\lambda}_*$
λ_*	$2\pi/k_*$	λ_0	$2\pi/w_*$	$2\pi\bar{\lambda}_*$
L	L	H	ρL	L
k	k	h	w	k
r	$\sqrt{2}\,r$	ζ		$\varepsilon/2\pi$

Table A.1: Notation used in this thesis and that used by several different authors. k_* is the controlling wavenumber, and λ_* the transition wavelength, $\lambda_* = 2\pi/k_*$, with $k_* = \sqrt{\frac{L}{2\eta C_0 (K_I + K_B)}}$. $r = a/\lambda$ is the single wavelength roughness, and $\varepsilon = ak = 2\pi r$ is the (local bed) slope number. L is the latent heat of fusion per unit volume of ice.

C_0	$0.8 \times 10^{-7}\,^{\circ}\mathrm{C\,m^2\,N^{-1}}$
Q	$4 \times 10^{-2}\,\mathrm{J\,m^{-2}\,s^{-1}}$
L	$2.8 \times 10^{8}\,\mathrm{J\,m^{-3}}$
η_I	$3 \times 10^{12}\,\mathrm{N\,m^{-2}\,s}$
K_I	$2.0\,\mathrm{J\,m^{-1}\,s^{-1}\,^{\circ}C^{-1}}$
K_B	$\approx K_I$

Table A.2: Numerical values of physical parameters, based on Paterson (1981) and Hutter (1983). C_0 is the Clausius-Clapeyron constant, Q the geothermal heat flux, L the latent heat of fusion per unit volume of ice, η_I is the (linear) viscosity of ice, and K_I and K_B are the thermal conductivities of the ice and bed respectively.

to the transition wavelength, *i.e.*

$$\bar{w}^2 := (\lambda/\lambda_*)^2 = (k_*/k)^2 \tag{A.2}$$

$$= \frac{L}{2\,k^2\,\eta\,C_0\,(K_I + K_B)}. \tag{A.3}$$

k_* is the *controlling wavenumber*, given by

$$k_*^2 = \frac{L}{2\eta C_0\,(K_I + K_B)}. \tag{A.4}$$

Since the ratio $\bar{w}^2/(\bar{w}^2+1)$ will turn up in most of the following equations it will be abbreviated by β_1, or

$$\beta_1 := \frac{\bar{w}^2}{\bar{w}^2+1}. \tag{A.5}$$

This also agrees with Nye's notation. In the no-regelation limit $\beta_1 = 1$, and in the pure-regelation limit $\beta_0 = 0$. $\ln \bar{w}$ is a convenient measure of the importance of regelation.

The second parameter is Morland's A parameter, which will here be denoted by A_m.

$$A_m = \frac{(K_I + K_B)\cos(\alpha)\rho\,g\,C_0 + 2\,Q}{L u_b} \tag{A.6}$$

$$= \frac{a^2 k^3 \eta}{L}\left(\frac{C_0\,(K_I + K_B)\cot(\alpha)}{h} + \frac{2Q}{\tau_b}\right). \tag{A.7}$$

The effect of freezing and melting on the flow field is negligible if $A_m \ll 1$, which is almost always the case (Morland, 1976a).

The basal sliding velocity u_b is

$$u_b = \frac{\tau_b}{\eta\varepsilon^2 k}\frac{(\bar{w}^2+1)}{\bar{w}^2} \tag{A.8}$$

$$= \frac{\tau_b}{\eta\varepsilon^2}\left(\frac{1}{k} + \frac{1}{k_*}\frac{k}{k_*}\right). \tag{A.9}$$

In the no-regelation limit $k/k_* \ll 1$ and

$$u_b = \frac{\tau_b}{\eta k \varepsilon^2}. \tag{A.10}$$

In the pure-regelation limit $k/k_* \gg 1$ and

$$u_b = \frac{\tau_b k}{\eta \varepsilon^2 k_*^2} \tag{A.11}$$

u_b has a minimum at $k = k_*$ and the largest part of the drag is contributed by the Fourier components of the bed with wavelengths (having the same amplitude to wavelength ratio) around λ_* (Nye, 1969).

Note that

$$u_b \beta_1 = \frac{\tau_b}{\eta \varepsilon^2 k}, \tag{A.12}$$

which is a useful relation that can be used to eliminate the sliding velocity from the following equations.

The horizontal velocity field is given by

$$\begin{aligned} v_x(x,z) &= u_b + \frac{\tau_b h}{2\eta}\left(1-(1-z/h)^2\right) \\ &+ u_b \beta_1 kze^{-kz}\left(\sin(kx) - A_m\cos(kx)\right)\varepsilon \\ &+ u_b \beta_1 e^{-2kz}\left(\cos(2kx) + A_m \sin(2kx)\right)(1/4 - kz/2)\,\varepsilon^2 \\ &+ O(\varepsilon^3). \end{aligned} \tag{A.13}$$

Note also that for $z = 0$ the first order term vanishes.

The vertical velocity field is given by

$$\begin{aligned} v_z(x,z) &= u_b \beta_1 e^{-kz}\left(\cos(kx) + A_m \sin(kx)\right)(1+kz)\,\varepsilon \\ &+ \frac{1}{2} u_b \beta_1 kze^{-2kz}\left(\sin(2kx) - A_m\cos(2kx)\right)\varepsilon^2 \\ &+ O(\varepsilon^3). \end{aligned} \tag{A.14}$$

The corresponding strain rates are given by

$$\begin{aligned} \dot{\epsilon}_{xx} &= u_b \beta_1 zk^2 e^{-kz}\left(\cos(kx) + A_m \sin(kx)\right)\varepsilon \\ &+ u_b \beta_1 ke^{-2kz}\left(\sin(2kx) - A_m\cos(2kx)\right)(kz - 1/2)\,\varepsilon^2 \\ &+ O(\varepsilon^3). \end{aligned} \tag{A.15}$$

$$\begin{aligned} \dot{\epsilon}_{xz} &= \frac{1}{2}(1-z/h)\,a^2k^3u_b \\ &+ u_b \beta_1 zk^2 e^{-kz}\left(A_m\cos(kx) - \sin(kx)\right)\varepsilon \\ &+ u_b \beta_1 ke^{-2kz}\left(kz - 1/2\right)\left(\cos(2kx) + A_m \sin(2kx)\right)\varepsilon^2 \\ &+ O(\varepsilon^3). \end{aligned} \tag{A.16}$$

The second invariant of the strain-rate tensor is given by

$$\begin{aligned}
\dot{\epsilon}_{II}^2 &= \frac{1}{4}(1-z/h)^2\, a^4 k^6 u_b^2 \\
&+ u_b^2\, \beta_1\, (1-z/h)\, (A_m\, \cos(kx) - \sin(kx))\, z k^5 a^2 e^{-kz}\, \varepsilon \\
&+ u_b^2\, \beta_1^2 \left(A_m^2 + 1\right) z^2 k^4 e^{-2\,kz}\, \varepsilon^2 \\
&+ u_b^2\, \beta_1\, (1-z/h)\, (kz - 1/2)\, (A_m\, \sin(2\,kx) + \cos(2\,kx))\, a^2 k^4 e^{-2\,kz}\, \varepsilon^2 \\
&+ u_b^2\, \beta_1^2 \left(A_m^2 + 1\right) (2\,kz - 1) \sin(kx)\, z k^3 e^{-3\,kz}\, \varepsilon^3 \\
&+ u_b^2\, \beta_1^2\, (kz - 1/2)^2 \left(A_m^2 + 1\right) k^2 e^{-4\,kz}\, \varepsilon^4 \\
&+ O(\varepsilon^6).
\end{aligned} \tag{A.17}$$

The pressure is given by

$$\begin{aligned}
p(x,z) &= p_a + \rho g\, \cos(\alpha)\, (1 - z/h) \\
&+ 2 u_b\, \beta_1\, \eta k e^{-kz}\, (\cos(kx) + A_m\, \sin(kx))\, \varepsilon \\
&+ u_b\, \beta_1\, \eta k e^{-2\,kz}\, (\sin(2\,kx) - A_m\, \cos(2\,kx))\, \varepsilon^2 \\
&+ O(\varepsilon^3).
\end{aligned} \tag{A.18}$$

These expressions can be used to calculate the flow and the sliding velocity for a general bed geometry. Different Fourier components can simply be added linearly together. Calculating the regelation velocity and the viscous flow velocity separately for a general bed geometry and afterwards adding the two components together would on the other hand give an incorrect result. The reason for this is, as Nye (1969) explains, that the pressure distribution that results from the process of regelation is in general different from the one that is caused by viscous flow over a bump, so that the two flows will interfere.

Bibliography

Björnsson, H. (1981). Radio-echo sounding maps of Storglaciären, Isfallsglaciären, and Rabots glaciär, northern Sweden. *Geografiska Annaler*, 63A(3-4):225–231.

Blake, E., Clarke, G. K. C., and Gérin, M. C. (1992). Tools for examining subglacial bed deformation. *Journal of Glaciology*, 38(130):388–396.

Budd, W. F. and Jacka, T. H. (1989). A review of ice rheology for ice sheet modeling. *Cold Regions Science and Technology*, 16:107–144.

Carol, H. (1947). The formation of roches moutonnées. *Journal of Glaciology*, 1(2):57–60.

Chadbourne, B. D., Coole, R. M., Tootill, S., and Walford, M. E. R. (1975). The movement of melting ice over rough surfaces. *Journal of Glaciology*, 14(71):287–292.

Demorest, M. (1941). Glacier flow and its bearing on the classification of glaciers. *Bulletin of the Geological Society of America*, 52(12):2024–25. Pt. 2.

Demorest, M. (1942). Glacier regimes and ice movements within glaciers. *American Journal of Science*, 240(1):31–66.

Drake, L. D. and Shreve, R. L. (1973). Pressure melting and regelation of ice by round wires. *Proceedings of the Royal Society of London, Ser A*, 332(1588):51–83.

Fowler, A. C. (1979). A mathematical approach to the theory of glacier sliding. *Journal of Glaciology*, 23(89):131–141.

Fowler, A. C. (1981). A theoretical treatment of the sliding of glaciers in the absence of cavitation. *Philosophical Transactions of the Royal Society of London, Ser. A*, 298(1445):637–685.

Fowler, A. C. (1986). A sliding law for glaciers of constant vicosity in the presence of subglacial cavitation. *Proceedings of the Royal Society of London, Ser A*, 407:147–170.

Fowler, A. C. (1987). Sliding with cavity formation. *Journal of Glaciology*, 33(115):225–257.

Glen, J. W. (1952). Experiments on the deformation of ice. *Journal of Glaciology*, 2(12):111–114.

Glen, J. W. (1955). The creep of polycrystalline ice. *Proceedings of the Royal Society of London, Ser A*, 228(1175):519–538.

Harbor, J. M. (1992). Application of a general sliding law to simulating flow in a glacier cross-section. *Journal of Glaciology*, 38(128):182–190.

Hasimoto, H. and Sano, O. (1980). Stokeslets and eddies in creeping flow. *Ann. Rev. Fluid Mech.*, 12:335–363.

Hooke, R. L., Holmlund, P., and Iverson, N. R. (1987). Extrusion flow demonstrated by bore-hole deformation measurements over a riegel, Storglaciären, Sweden. *Journal of Glaciology*, 33(113):72–78.

Humphrey, N. (1987). Coupling between water pressure and basal sliding in a linked-cavity hydraulic system. In D., E. and Walder, J. S., editors, *The Physical Basis of Ice Sheet Modelling*, number 170 in Int. Assoc. Hydrol. Sci. Publ., pages 201–224.

Hutter, K. (1983). *Theoretical glaciology; material science of ice and the mechanics of glaciers and ice sheets.* D. Reidel Publishing Company/Tokyo, Terra Scientific Publishing Company.

Hutter, K. (1991). *Einführung in die Fluid- und Thermodynamik.* im Selbstverlag, Darmstadt.

Hutter, K. (1993). Thermo-mechanically coupled ice-sheet response — cold, polythermal, temperate. *Journal of Glaciology*, 39(131):65–86.

Hutter, K., Blatter, H., and Funk, M. (1988). A model computation of moisture content in polythermal glaciers. *Journal of Geophysical Research*, 93(B10):12,205–12,214.

Iken, A. (1981). The effect of the subglacial water pressure on the sliding velocity of a glacier in an idealized numerical model. *Journal of Glaciology*, 27(97):407–421.

Iken, A. and Bindschadler, A. (1986). Combined measurements of subglacial water pressure and surface velocity of Findelengletscher, Switzerland: Conclusions about drainage system and sliding mechanism. *Journal of Glaciology*, 32(110):101–119.

IMSL (1989). *IMSL MATH/LIBRARY User's Manual.* Problem-Solving Software Systems, 2500 ParkWest Tower One, 2500 CityWest Boulevard, Houston, Texas 77042-3020, USA, 1.1 edition.

Johnson, Jr., M. W. (1960). Some variational theorems for non-Newtonian flow. *The Physics of Fluids*, 3(6):871–878.

Kamb, B. (1970). Sliding motion of glaciers: Theory and observation. *Reviews of Geophysics and Space Physics*, 8(4):673–728.

Kamb, B. (1987). Glacier surge mechanism based on linked cavity configuration of the basal water conduit system. *Journal of Geophysical Research*, 92(B9):9083–9100.

Kamb, B. (1993). Glacier flow modeling. In Stone, D. B. and Runcorn, S. K., editors, *Flow and Creep in the Solar System: Observations, Modeling and Theory*, volume 391 of *NATO ASI Series C: Mathematical and Physical Sciences*, pages 417–506. Kluwer Academic Publishers.

Lile, R. C. (1978). The effect of anisotropy on the creep of polycrystalline ice. *Journal of Glaciology*, 21(85):475–483.

Lliboutry, L. (1993). Internal melting and ice accretion at the bottom of temperate glaciers. *Journal of Glaciology*, 39(131):50–64.

Lliboutry, L. A. (1959). Une théorie du frottement du glacier sur son lit. *Ann. Géophys.*, 15(2):250–65.

Lliboutry, L. A. (1968). General theory of subglacial cavitation and sliding of temperate glaciers. *Journal of Glaciology*, 7(49):21–58.

Lliboutry, L. A. (1976). Physical processes in temperate glaciers. *Journal of Glaciology*, 16(74):209–218.

Lliboutry, L. A. (1979). Local frictions laws for glaciers: a critical review and new openings. *Journal of Glaciology*, 23(89):67–95.

Lliboutry, L. A. (1987a). Realistic, yet simple bottom boundary conditions for glaciers and ice sheets. *Journal of Geophysical Research*, 92(B9):9101–9109.

Lliboutry, L. A. (1987b). *Very Slow Flows of Solids; basics of modeling in geodynamics and glaciology.* Martinus Nijhoff Publishers.

MARC (1992). *MARC/MENTAT User's Manual.* MARC Analysis Research Corporation, 260 Sherida Avenue, Palo Alto, CA 94306, K5 edition.

Menikoff, R. and Zemach, C. (1980). Methods for numerical conformal mapping. *Journal of Computational Physics*, 36:366–410.

Meyssonnier, J. (1983). *Ecoulement de la glace sur un lit de forme simple: Expérience, modélisation, paramétrisation du frottement.* PhD thesis, Univ. of Grenoble. 359 pp.

Meyssonnier, J. (1989). Ice flow over a bump: experiment and numerical simulations. *Journal of Glaciology*, 35(119).

Moffatt, H. K. (1964). Viscous and resistive eddies near a sharp corner. *Jour. Fluid Mech*, 18:1–18.

Morland, L. W. (1976a). Glacier sliding down an inclined wavy bed. *Journal of Glaciology*, 17(77):447–462.

Morland, L. W. (1976b). Glacier sliding down an inclined wavy bed with friction. *Journal of Glaciology*, 17(77):463–477.

Morris, E. M. (1976). An experimental study of the motion of ice past obstacles by the process of regelation. *Journal of Glaciology*, 17(75):79–98.

Nye, J. F. (1952). Reply to Mr. Joel E. Fisher's comments. *Journal of Glaciology*, 2(11):52–53.

Nye, J. F. (1953). The flow law of ice from measurements in glacier tunnels, laboratory experiments and the Jungfraufirn borehole experiment. *Proceedings of the Royal Society of London, Ser A*, 219(1193):477–489.

Nye, J. F. (1957). The distribution of stress and velocity in glaciers and ice-sheets. *Proceedings of the Royal Society of London, Ser A*, 239(1216):113–133.

Nye, J. F. (1965). The flow of a glacier in a channel of rectangular, elliptic or parabolic cross-section. *Journal of Glaciology*, 5(41):661–690.

Nye, J. F. (1967). Theory of regelation. *Phil Mag.*, 16(144):1275–80.

Nye, J. F. (1969). A calculation on the sliding of ice over a wavy surface using a Newtonian viscous approximation. *Proceedings of the Royal Society of London, Ser A*, 311(1506):445–467.

Nye, J. F. (1970). Glacier sliding without cavitation in a linear viscous approximation. *Proceedings of the Royal Society of London, Ser A*, 315(1522):381–403.

Paterson, W. S. B. (1981). *The physics of glaciers.* Pergamon Press, Oxford, 2. edition.

Raymond, C. F. (1971). Flow in a transverse section of Athabasca Glacier, Alberta, Canada. *Journal of Glaciology*, 10(58):55–69.

Raymond, C. F. (1978). Numerical calculation of glacier flow by finite elements methods. Final technical report for National Science Foundation Grant No. DPP74-19075.

Reynaud, L. (1973). Flow of a valley glacier with a solid friction law. *Journal of Glaciology*, 12(65):251–258.

Schweizer, J. (1989). Friction at the base of a glacier. Mitteilung 101, Versuchsanstalt für Wasserbau, Hydrologie und Glaziologie der ETH Zürich, Gloriastrasse 37-39, ETH-Zentrum, CH-8092 Zürich.

Schweizer, J. and Iken, A. (1992). The role of bed separation and friction in sliding over an undeformable bed. *Journal of Glaciology*, 38(128):77–92.

Seligman, G. (1947). Extrusion flow in glaciers. *Journal of Glaciology*, 1(1):12–18.

Sherman, F. S. (1990). *Viscous Flow.* McGraw-Hill Series in Mechanical Engineering. McGraw-Hill, Inc.

Shreve, R. L. (1984). Glacier sliding at subfreezing temperatures. *Journal of Glaciology*, 30(106):341–347.

Steinemann, S. (1958a). Experimentelle Untersuchungen zur Plastizität von Eis. Geotechnische Serie Nr. 10, Beiträge zur Geologie der Schweiz.

Steinemann, S. (1958b). Résultats expérimentaux sur la dynamique da la glace et leurs correlations avec le mouvement et la pétrographie des glaciers. *International Association of Scientific Hydrology*, 47:184–198.

Streiff-Becker, R. (1938). Zur Dynamik des Firneises. *Zeitshrift für Gletscherkunde*, 25(1/2):1–21.

Taneda, S. (1956). Experimental investigation of the wakes behind cylinders and plates at low reynolds numbers. *J. Phys. Soc. Japan*, 11:302–307.

Tsangaris, S. and Potamitis, D. (1985). On laminar small Reynolds-number flow over wavy walls. *Acta Mechanica*, 61:109–115.

van der Veen, C. J. and Whillans, I. M. (1990). Flow laws for glacier ice: comparison of numerical predictions and field measurments. *Journal of Glaciology*, 36(124):324–339.

Weertman, J. (1957). On the sliding of glaciers. *Journal of Glaciology*, 3(21):33–38.

Weertman, J. (1964). The theory of glacier sliding. *Journal of Glaciology*, 5(39):287–303.

Weertman, J. (1971). In defence of a simple model of glacier sliding. *Journal of Geophysical Research*, 76(26):6485–87.

Weertman, J. (1979). The unsolved general glacier sliding problem. *Journal of Glaciology*, 23(89):97–111.

White, F. M. (1991). *Viscous Fluid Flow*. McGraw-Hill Series in Mechanical Engineering. McGraw-Hill, Inc., second edition.

Acknowledgements

The continuous guidance given by Dr. Almut Iken during the course of this study is gratefully acknowledged.

The study was made possible by Prof. Dr. Dr. h. c. D. Vischer, head of the Hydraulics, Hydrology and Glaciology Laboratory (VAW) of the ETH Zürich, who provided all facilities and equipment. His support, particularly during the evaluative stages of the work, is greatly appreciated.

I have gained profoundly from numerous discussions with Dr. Martin Funk.

Prof. K. Hutter critically reviewed the work and helped as a "advocatus diaboli" in determining its final form.

I thank Prof. B. Hallet for bringing the paper of H. Carol on the formation of *Roches Moutonnées* as well as the paper of S. Tsangaris and D. Potamitis on flow over wavy walls to my attention.

Dr. Peter Collins corrected the English.

Special thanks to Simone Strohm. Her continuous support was essential for the successful completion of this work.

This work was supported by the Swiss National Science Foundation (Schweizerischer Nationalfonds), Grant Nr. 20-29619.90.